

Dielectronic Recombination (via $N = 2 \rightarrow N' = 2$ Core Excitations) and Radiative Recombination of Fe XX: Laboratory Measurements and Theoretical Calculations

D. W. Savin, E. Behar, and S. M. Kahn

*Columbia Astrophysics Laboratory and Department of Physics, Columbia University,
New York, NY 10027, USA*

savin@astro.columbia.edu

G. Gwinner, A. A. Saghiri, M. Schmitt, M. Grieser, R. Repnow, D. Schwalm, and A. Wolf

*Max-Planck-Institut für Kernphysik, D-69117 Heidelberg, Germany
and Physikalisches Institut der Universität Heidelberg, D-69120 Heidelberg, Germany*

T. Bartsch, A. Müller, and S. Schippers

*Institut für Kernphysik, Strahlenzentrum der Justus-Liebig-Universität, D-35392 Giessen,
Germany*

N. R. Badnell

*Department of Physics and Applied Physics, University of Strathclyde, Glasgow, G4 0NG,
United Kingdom*

M. H. Chen

Lawrence Livermore National Laboratory, Livermore, CA 94550, USA

and

T. W. Gorczyca

Department of Physics, Western Michigan University, Kalamazoo, MI 49008, USA

ABSTRACT

We have measured the resonance strengths and energies for dielectronic recombination (DR) of Fe XX forming Fe XIX via $N = 2 \rightarrow N' = 2$ ($\Delta N = 0$) core excitations. We have also calculated the DR resonance strengths and energies using AUTOSTRUCTURE, HULLAC, MCDF, and R-matrix methods, four different state-of-the-art theoretical techniques. On average the theoretical resonance

strengths agree to within $\lesssim 10\%$ with experiment. The AUTOSTRUCTURE, MCDF and R-matrix results are in better agreement with experiment than are the HULLAC results. However, in all cases the 1σ standard deviation for the ratios of the theoretical-to-experimental resonance strengths is $\gtrsim 30\%$ which is significantly larger than the estimated relative experimental uncertainty of $\lesssim 10\%$. This suggests that similar errors exist in the calculated level populations and line emission spectrum of the recombined ion. We confirm that theoretical methods based on inverse-photoionization calculations (e.g., undamped R-matrix methods) will severely overestimate the strength of the DR process unless they include the effects of radiation damping. We also find that the coupling between the DR and radiative recombination (RR) channels is small.

Below 2 eV the theoretical resonance energies can be up to $\approx 30\%$ larger than experiment. This is larger than the estimated uncertainty in the experimental energy scale ($\lesssim 0.5\%$ below ≈ 25 eV and $\lesssim 0.2\%$ for higher energies) and is attributed to uncertainties in the calculations. These discrepancies makes DR of Fe XX an excellent case for testing atomic structure calculations of ions with partially filled shells. Above 2 eV, agreement between theory and experiment improves dramatically with the AUTOSTRUCTURE and MCDF results falling within 2% of experiment, the R-matrix results within 3%, and HULLAC within 5%. Agreement for all four calculations improves as the resonance energy increases.

We have used our experimental and theoretical results to produce Maxwellian-averaged rate coefficients for $\Delta N = 0$ DR of Fe XX. For $k_B T_e \gtrsim 1$ eV, which includes the predicted formation temperatures for Fe XX in an optically thin, low-density photoionized plasma with cosmic abundances, the experimental and theoretical results agree to better than $\approx 15\%$. This is within the total estimated experimental uncertainty limits of $\lesssim 20\%$. Agreement below ≈ 1 eV is difficult to quantify due to current theoretical and experimental limitations. Agreement with previously published *LS*-coupling rate coefficients is poor, particularly for $k_B T_e \lesssim 80$ eV. This is attributed to errors in the resonance energies of these calculations as well as the omission of DR via $2p_{1/2} \rightarrow 2p_{3/2}$ core excitations. We have also used our R-matrix results, topped off using AUTOSTRUCTURE for RR into $J \geq 25$ levels, to calculate the rate coefficient for RR of Fe XX. Our RR results are in good agreement with previously published calculations. We find that for temperatures as low as $k_B T_e \approx 10^{-3}$ eV, DR still dominates over RR for this system.

Subject headings: atomic data – atomic processes

1. Introduction

Low temperature dielectronic recombination (DR) is the dominant recombination mechanism for most ions in photoionized cosmic plasmas (Ferland et al. 1998). Reliably modeling and interpreting spectra from these plasmas requires accurate low temperature DR rate coefficients. Of particular importance are the DR rate coefficients for the iron L -shell ions (Fe XVII-Fe XXIV). These ions are predicted to play an important role in determining the thermal structure and line emission of X-ray photoionized plasmas (Hess, Kahn, & Paerels 1997; Savin et al. 1999, 2000) which are predicted to form in the media surrounding accretion powered sources such as X-ray binaries (XRBs), active galactic nuclei (AGN), and cataclysmic variables (Kallman & Bautista 2001).

The need for reliable DR data for iron L -shell ions has become particularly urgent with the recent launches of *Chandra* and *XMM-Newton*. These satellites are now providing high-resolution X-ray spectra from a wide range of X-ray photoionized sources. Examples of the high quality of the data that these satellites are collecting are given by the recent *Chandra* observations of the XRB Cyg X-3 (Paerels et al. 2000) and the AGN NGC 3783 (Kaspi et al. 2000) and the *XMM-Newton* observations of the AGN NGC 1068 (Kinkhabwala et al. 2001) and the low-mass XRB EXO 0748-67 (Cottam et al. 2001). Interpreting the spectra from these and other photoionized sources will require reliable DR rate coefficients.

DR is a two-step recombination process that begins when a free electron approaches an ion, collisionally excites a bound electron of the ion and is simultaneously captured. The electron excitation can be labeled $Nl_j \rightarrow N'l'_j$, where N is the principal quantum number of the core electron, l its orbital angular momentum, and j its total angular momentum. This intermediate state, formed by the simultaneous excitation and capture, may autoionize. The DR process is complete when the intermediate state emits a photon which reduces the total energy of the recombined ion to below its ionization limit. Conservation of energy requires that for DR to go forward $E_k = \Delta E - E_b$. Here E_k is the kinetic energy of the incident electron, ΔE the excitation energy of the initially bound electron, and E_b the binding energy released when the incident electron is captured onto the excited ion. Because ΔE and E_b are quantized, DR is a resonant process. DR via $N' = 2 \rightarrow N = 2$ core excitations (i.e., $\Delta N \equiv N' - N = 0$ DR) generally dominates the DR process for iron L -shell ions in photoionized plasmas (Savin et al. 1997, 2000).

To address the need for accurate low temperature DR rate coefficients for the iron L -shell ions, we have initiated a program of measurements for DR via $2 \rightarrow 2$ core excitations using the heavy-ion Test Storage Ring (TSR) located at the Max-Planck-Institute for Nuclear Physics in Heidelberg, Germany (Müller & Wolf 1997). To date measurements have been carried out for $\Delta N = 0$ DR of Fe XVIII (Savin et al. 1997, 1999), Fe XIX (Savin et al. 1999),

Fe XX, Fe XXI, and Fe XXII. Here we present our results for $\Delta N = 0$ DR of Fe XX forming Fe XIX. Preliminary results were presented in Savin et al. (2000). Results for Fe XXI and Fe XXII will be given in future publications.

$\Delta N = 0$ DR of nitrogenlike Fe XX can proceed via a number of intermediate resonance states. DR occurs when the autoionizing Fe XIX states, produced in the dielectronic capture process, radiatively stabilize to a bound configuration. Here $\Delta N = 0$ captures led to measurable DR resonances for electron-ion collision energies between 0 and ≈ 105 eV and involved the following resonances

$$\text{Fe}^{19+}(2s^2 2p^3 [^4S_{3/2}^o]) + e^- \rightarrow \left\{ \begin{array}{ll} \text{Fe}^{18+}(2s^2 2p^3 [^2D_{3/2}^o]nl) & (n = 17, \dots, \infty) \\ \text{Fe}^{18+}(2s^2 2p^3 [^2D_{5/2}^o]nl) & (n = 15, \dots, \infty) \\ \text{Fe}^{18+}(2s^2 2p^3 [^2P_{1/2}^o]nl) & (n = 13, \dots, \infty) \\ \text{Fe}^{18+}(2s^2 2p^3 [^2P_{3/2}^o]nl) & (n = 12, \dots, \infty) \\ \text{Fe}^{18+}(2s2p^4 [^4P_{5/2}]nl) & (n = 8, \dots, \infty) \\ \text{Fe}^{18+}(2s2p^4 [^4P_{3/2}]nl) & (n = 7, \dots, \infty) \\ \text{Fe}^{18+}(2s2p^4 [^4P_{1/2}]nl) & (n = 7, \dots, \infty) \\ \text{Fe}^{18+}(2s2p^4 [^2D_{3/2}]nl) & (n = 7, \dots, \infty) \\ \text{Fe}^{18+}(2s2p^4 [^2D_{5/2}]nl) & (n = 7, \dots, \infty) \\ \text{Fe}^{18+}(2s2p^4 [^2S_{1/2}]nl) & (n = 6, \dots, \infty) \\ \text{Fe}^{18+}(2s2p^4 [^2P_{3/2}]nl) & (n = 6, \dots, \infty) \\ \text{Fe}^{18+}(2s2p^4 [^2P_{1/2}]nl) & (n = 6, \dots, \infty). \end{array} \right. \quad (1)$$

The lowest lying $\Delta N = 1$ resonances are predicted to occur at $E_k \approx 245$ eV. The excitation energies ΔE for all Fe XX levels in the $n = 2$ shell are listed, relative to the ground state, in Table 1.

The experimental technique used here is presented in § 2. Our results are given in § 3. Existing and new theoretical calculations are discussed in § 4. A comparison between theory and our experimental results is given in § 5 and conclusions in § 6.

2. Experimental Technique

DR measurements are carried out by merging, in one of the straight sections of TSR, a circulating ion beam with an electron beam. After demerging, recombined ions are separated from the stored ions using a dipole magnet and directed onto a detector. The relative electron-ion collision energy can be precisely controlled and the recombination signal measured as a function of this energy. Details of the experimental setup have been given elsewhere (Kilgus et al. 1992; Lampert et al. 1996; Savin et al. 1997, 1999). Here we discuss only those

new details of the setup which were specific to our Fe XX results.

A beam of 280 MeV $^{56}\text{Fe}^{19+}$ ions was produced and injected into TSR by the usual techniques. Stored ion currents of between $\approx 7 - 22 \mu\text{A}$ were achieved. The storage lifetime was ≈ 7 s. After injection, the ions were cooled for ≈ 2 s before data collection began. This is long compared to the lifetimes of the various Fe XX metastable levels (Cheng, Kim, & Desclaux 1979) and all ions were assumed to be in their ground state for the measurements.

The electron beam was adiabatically expanded from a diameter of ≈ 0.95 cm at the electron gun cathode to ≈ 3.6 cm before it was merged with the ions. In the merged-beams region, the electrons were guided with a magnetic field of ≈ 40 mT and traveled co-linear with the stored ions for a distance of $L \approx 1.5$ m. The effective energy spread associated with the relative motion between the ions and the electrons corresponds to temperatures of $k_B T_{\perp} \approx 15$ meV perpendicular to the confining magnetic field and $k_B T_{\parallel} \approx 0.13$ meV parallel to the magnetic field. The electron density varied between $n_e \approx 1 - 3 \times 10^7 \text{ cm}^{-3}$.

Data were collected using three different schemes for chopping the electron beam between the energies for cooling (E_c), measurement (E_m), and reference (E_r). For center-of-mass collision energies $E_{cm} \lesssim 0.048$ eV, the chopping pattern (Mode A) began by jumping to E_c and allowing for a 1.5 ms settling time of the power supplies, followed by a simultaneous cooling of the ions and collecting of data for 30 ms. This was followed by a jump to E_m , allowing for a 1.5 ms settling time, and then collecting data for 5 ms. The pattern was completed by jumping to E_r , allowing for a 1.5 ms settling time, and then collecting data for 5 ms. For $E_{cm} \gtrsim 0.048$ eV, two different chopping patterns were used. Mode B was similar to Mode A except that when jumping to E_m , a settling time of 20 ms was used, and data were then collected for 20 ms. Mode C was similar to Mode B except an E_c - E_r - E_m chopping pattern was used. The chopping pattern was repeated ≈ 300 times between injections of new ion current. With each step in the chopping pattern, E_m was increased (or decreased) in the lab frame by ≈ 0.5 eV. The electron energy was stepped by this amount for all three modes.

The reference energy E_r was chosen so that radiative recombination (RR) and DR contributed insignificantly to the recombination counts collected at E_r . This count rate was due to essentially only charge transfer (CT) of the ion beam off the rest gas in TSR. Taking electron beam space charge effects into account, the reference energy was ≈ 1600 eV greater than the cooling energy of ≈ 2740 eV. This corresponds to an $E_{cm} \approx 183$ eV.

Center-of-mass collision energies were calculated using the velocities of the electrons and the ions in the overlap region. The electron velocity was calculated using the calibrated acceleration voltage and correcting for the effects of space charge in the electron beam

using the beam energy and diameter and the measured beam current. The ion velocity is determined by the electron velocity at cooling.

For Fe XX, the DR resonance energies measured using Mode C did not precisely match those measured using Mode B. In the lab frame, resonances measured using Mode C occurred at energies $\approx 1.0 - 1.5$ eV lower than those using Mode B. This shift is attributed to E_r preceding E_m for mode C versus E_c preceding E_m in mode B. Capacitances in the electron cooler prevented the acceleration voltage from reaching the desired value in the time allotted. For the data collected here, E_c was essentially always smaller than E_m and E_r was always larger than E_m . Hence in mode B, when the beam energy was chopped from E_c up to E_m , the cooler capacitances prevented the beam energy from increasing all the way to E_m and the true electron beam energy was slightly less than expected. Conversely, in mode C when the beam energy was chopped from E_r down to E_m , these capacitances prevented the beam energy from decreasing all the way to E_m and the true beam energy was slightly higher than expected. E_{cm} was calculated using the expected electron beam energy. Thus the calculated energies in mode B were slightly too high and in mode C slightly too low. To merge the Mode B and Mode C data sets we shifted the Mode C data up in energy, in the lab frame, by ≈ 1.0 eV at moderate energies and ≈ 1.5 eV at higher energies. Technical reasons for the occurrence of these voltage errors have been identified and corrected.

The systematic inaccuracies in the absolute E_{cm} scale derived from the voltage calibrations were $\lesssim 2\%$. To increase the accuracy of the E_{cm} scale, a final normalization of the E_{cm} scale was performed using calculated energies for the DR resonances,

$$E_{nl} = \Delta E - \left(\frac{z}{n - \mu_l} \right)^2 \mathcal{R}. \quad (2)$$

Here E_{nl} is the resonance energy for DR into a given nl level, z the charge of the ion before DR, μ_l the quantum defect for the recombined ion, and \mathcal{R} the Rydberg energy. Values for ΔE were taken from spectroscopic measurements (Sugar & Corliss 1985) as listed in Table 1. The quantum defects account for energy shifts of those l levels which have a significant overlap with the ion core and cannot be described using the uncorrected Rydberg formula. As l increases, the overlap with the ion core decreases and μ_l goes to zero.

For the normalization of the E_{cm} scale we used DR resonances with $n \geq 7$ which were essentially unblended with other resonances. We considered only the high- l contributions occurring at the highest energy of a given n manifold, for which μ_l is essentially zero. The resulting calculated resonance energies were ≈ 1.046 times the experimental energy scale for $E_{cm} \approx 0.17$ eV. This factor decreased nonlinearly with increasing energy to ≈ 1.016 at ≈ 10 eV and then slowly decreased to ≈ 1.003 with increasing energy. We multiplied the experimental energy scale by this energy-dependent normalization factor to produce the

final energy scale for the results presented here. After corrections, we estimate that above ≈ 25 eV, the uncertainty in the corrected energy scale is $\lesssim 0.2\%$. Below ≈ 25 eV, it is estimated to be $\lesssim 0.5\%$.

The electron and ion beams were merged and then, after passing through the interaction region, they were separated using toroidal magnets. The motional electric fields in the downstream toroidal magnet field-ionized electrons which had dielectronically recombined into Rydberg levels $n \gtrsim n_{cut1} = 146$. Further downstream, two correction dipole magnets field-ionized electrons in levels $n \gtrsim n_{cut2} = 120$. Finally, the recombined ions passed through a dipole which separated them from the primary ion beam and directed them onto a detector. Electrons in $n \gtrsim n_{cut3} = 64$ were field ionized by this magnet. The flight time of the ions from the center of the interaction region to the final dipole magnet was ≈ 166 ns. During this time some of the captured electrons radiatively decayed below the various values of n_{cut} . DR occurs primarily into $l \lesssim 8$ levels. Using the hydrogenic formula for radiative lifetimes of Marxer & Spruch (1991), we estimate that for DR into $n \lesssim n_{max} = 120$, the captured electrons radiatively decayed below the various values of n_{cut} before reaching the final dipole and were therefore detected by our experimental arrangement.

The measured recombination signal rate was calculated by taking the rate at the measurement energy $R(E_{cm})$ and subtracting from it the corresponding rate at the reference energy $R(E_{ref})$. This eliminates the effects of slow pressure variations during the scanning of the measurement energy but not the effects of any fast pressure variations associated with the chopping of the electron beam energy, leaving a small residual CT background. Following Schippers et al. (2001), the measured rate coefficient $\alpha(E_{cm})$ is given by

$$\alpha_L(E_{cm}) = \frac{[R(E_{cm}) - R(E_{ref})]\gamma^2}{n_e N_i (L/C)\eta} + \alpha(E_{ref}) \frac{n_e(E_{ref})}{n_e(E_{cm})}. \quad (3)$$

Here N_i is the number of ions stored in the ring, $C = 55.4$ m the circumference of the ring, η the detection efficiency of the recombined ions (which is essentially 1), $\gamma^2 = [1 - (v/c)^2]^{-1} \approx 1.01$, and c the speed of light. The measured rate coefficient represents the DR and RR cross sections multiplied by the relative electron-ion velocity and then convolved with the experimental energy spread. The data sit on top of the residual CT background. The experimental energy spread is best described by an anisotropic Maxwellian distribution in the comoving frame of the electron beam. The second term in Equation 3 is a small correction to re-add the RR signal at the reference which is subtracted out in the expression $[R(E_{cm}) - R(E_{ref})]$. Here we used the theoretical RR rate coefficient at $E_{cm} = 183$ eV where contributions due to DR are insignificant. The RR rate coefficient at this energy, calculated using a modified semi-classical formula for the RR cross section (Schippers et al. 1998), is $\approx 4.3 \times 10^{-12}$ cm³ s⁻¹. Using $\alpha_L(E_{cm})$, the effects of the merging and demerging of the

electron and ion beams are accounted for, following the procedure described in Lampert et al. (1996), to produce a final measured recombination rate coefficient $\alpha(E_{cm})$ from which the DR results are extracted.

The DR resonances produce peaks in $\alpha(E_{cm})$. Resonance strengths are extracted after subtracting out the smooth background due to RR and CT. Although RR dominates the smooth background at low energies, we have been unable to extract reliable RR rate coefficients due to the remaining CT contributions to the measured signal rate.

Experimental uncertainties have been discussed in detail elsewhere (Kilgus et al. 1992; Lampert et al. 1996). The total systematic uncertainty in our absolute DR measurements is estimated to be $\lesssim 20\%$. The major sources of uncertainties include the electron beam density determination, the ion current measurement, corrections for the merging and de-merging of the two beams, the efficiency of the recombined ion detector, resonance strength fitting uncertainties, and uncertainties in the shape of the interpolated smooth background (particularly in regions where the DR resonances were so numerous that the background was not directly observable). Another source of uncertainty is that we assume each DR feature can be fit using a single resonance peak when in fact each feature is often composed of many unresolved resonance peaks. Relative uncertainties for comparing our DR results at different energies are estimated to be $\lesssim 10\%$. Uncertainties are quoted at a confidence level believed to be equivalent to a 90% counting statistics confidence level.

3. Experimental Results

Our measured spectrum of Fe XX to Fe XIX $\Delta N = 0$ DR resonances is shown in Figure 1(a). The data represent the sum of the RR and DR cross sections times the relative electron-ion velocity convolved with the energy spread of the experiment, i.e., a rate coefficient. The data are presented as a function of E_{cm} . For energies below 7.5 eV, we use the predicted asymmetric line shape for the DR resonances (Kilgus et al. 1992) and fit the data to extract DR resonance strengths and energies. Above 7.5 eV, the asymmetry is insignificant and we fit the data using Gaussian line shapes. Extracted resonance strengths S_d and energies E_d for a given DR resonance or blend of resonances d are listed in Table 2. The energies have been corrected as described in § 2.

The lowest-energy resolved resonance is the $2s^22p^3(^2D_{3/2}^o)17l$ blend at $E_{cm} \approx 0.081$ eV. Our fit to this blend begins to deviate significantly from the measured data for $E_{cm} \lesssim 0.05$ eV (see Figure 2). We attribute this deviation to unresolved broad and narrow DR resonances lying below 0.05 eV.

Due to the energy spread of the electron beam, resonances below $E_{cm} \approx k_B T_e \approx 0.015$ eV cannot be resolved from the near 0 eV RR signal. However, we can infer the presence of such resonances. The measured recombination rate coefficient at $E_{cm} \lesssim 10^{-4}$ eV is a factor of ≈ 90 times larger than the RR rate coefficient predicted using semiclassical RR theory with quantum mechanical corrections (Schippers et al. 1998). This enhancement factor is much larger than that found for Fe XVIII for which the near 0 eV recombination rate coefficient was a factor of ≈ 2.9 times larger than the theoretical RR rate coefficient. Fe XVIII is predicted to have no DR resonances near 0 eV. A similar enhancement (factor of ≈ 2.2) was found for RR of bare Cl XVIII (Hoffknecht et al. 2001). For Fe XIX, the enhancement was a factor of ≈ 10 . Fe XIX and Fe XX are both predicted to have near 0 eV DR resonances and the inferred enhancement factors of greater than 2.9 are attributed to these unresolved near 0 eV resonances.

We note that a number of issues pertaining to recombination measurements in electron coolers at $E_{cm} \lesssim k_B T_e$ remain to be resolved (Hoffknecht et al. 1998; Schippers et al. 1998; Gwinner et al. 2000; Hoffknecht et al. 2001), but it is highly unlikely that their resolution will lead to a near 0 eV recombination rate coefficient that increases by a factor of ≈ 30 for a change in ionic charge from 17 to 19. Thus we infer that there are unresolved DR resonances lying at energies below 0.015 eV.

Our calculations suggest that these unresolved resonances are due to a combination of the $2s^2 2p^3 ({}^2D_{5/2}^o) 15l$ and $2s 2p^4 ({}^4P_{3/2}) 7d$ configurations. Calculations indicate these $15l$ resonances have natural line widths significantly smaller than the energy spread of the experiment. Here we treat them as delta functions for fitting purposes. To determine the energies of these $15l$ resonances, we use the calculated quantum defect for an nf electron in Fe XIX from Theodosiou et al. (1986). The f level is the highest angular momentum they considered. We extrapolate this quantum defect to higher angular momentum using the predicted l^{-1} behavior (Babb et al. 1992). The resulting resonance energies are listed in Table 2. We estimate that for this complex, the $15i$ level is the lowest lying DR resonance. The highest resonance energy (for the $15t$ level) is estimated to be at ≈ 0.005 eV.

The energy of the near 0 eV $2s 2p^4 ({}^4P_{3/2}) 7d$ resonance is difficult to predict reliably because of the large interaction of the captured electron with the core. Calculations indicate the resonance has a width of ≈ 10 meV which is comparable to the energy spread of the experiment. To fit for this feature we must take the natural line profile of the DR resonance and its E_{cm}^{-1} dependence into account. Mitnik et al. (1999) have addressed theoretically the issue of near 0 eV DR resonances. Starting from Equation 12 of their paper, we can write

the near 0 eV DR line profile as

$$\sigma_{DR}^d(E_{cm}) = \frac{S_d E_d}{E_{cm}} \left[\frac{\Gamma_d/2\pi}{(E_{cm} - E_d)^2 + (\Gamma_d/2)^2} \right] \quad (4)$$

where Γ_d is the natural line width of the resonance.

Recent measurements of recombination of bare Cl XVIII found an enhanced recombination rate coefficient for $E_{cm} \lesssim 0.008$ eV (Hoffknecht et al. 2001). We expect a similar situation for Fe XX. Because the unresolved $15l$ DR resonances all occur for $E_{cm} \lesssim 0.005$ eV, we attribute the DR signal between 0.008 and 0.05 eV to the unresolved $7d$ resonance. We have fit this portion of the recombination spectrum essentially by eye, varying the resonance width, strength, and energy. Our best fit was for an inferred resonance width of 10 meV. The inferred resonance energy and strength of this $7d$ resonances are listed in Table 2.

Based on our Fe XVIII results (Savin et al. 1997, 1999), we expect to see an enhancement of ≈ 2.9 as E_{cm} approaches 0 eV. Taking only the near 0 eV $7d$ resonance into account yields an enhancement factor of ≈ 6.7 . We infer the resonance strength of the near 0 eV $15l$ resonances by varying their amplitudes to produce a model recombination spectrum which yields an enhancement factor of ≈ 2.9 .

We have linked the resonance strengths of the near 0 eV $15l$ levels taking into account the behavior of the DR cross section. Following the logic in § II of Müller et al. (1987), when the radiative stabilization rate A_r is much greater than the autoionization rate A_a of the intermediate doubly-excited state in the DR process, then the DR resonance strength is proportional to A_a . For the $2s^2 2p^3 ({}^2D_{5/2}^o) 15l$, the excited core electron cannot decay via an electric dipole transition. Stabilization of the intermediate autoionizing state is due to a radiative decay by the Rydberg electron. Using the hydrogenic formula of Marxer & Spruch (1991) for the radiative lifetime of the $15l$ electron and our calculated MCDF autoionization rates, we find that the radiative rates are always significantly larger than the autoionization rates. We have therefore linked the relative resonance strengths for the near 0 eV $15l$ resonances using the MCDF calculated A_a values. Thus the amplitudes of these resonances are controlled by a single normalization factor. We have varied this factor until our model recombination spectrum yields an enhancement factor of ≈ 2.9 for $E_{cm} < 10^{-4}$ eV. The inferred resonance strengths for these $15l$ resonances are listed in Table 2.

The measured and model recombination spectrum below $E_{cm} = 0.1$ eV is shown in Figure 2. For the model spectrum we use our inferred and extracted resonance strengths and energies. We have looked at the difference between the measured and model spectrum between 0.008 and 0.05 eV. The resulting residuals are comparable to the difference between the measured spectrum and the fitted spectrum for those peaks below 1 eV which we were

able to fit using a χ^2 procedure. We note here that the 10 meV width of this resonances is significantly larger than our fitted resonance energy of 3 meV. Thus we infer that the DR cross section is non-zero in value for $E_{cm} = 0$ eV and that the resulting Maxwellian DR rate coefficient will increase as the plasma temperature decreases.

We have used the extracted DR resonance strengths and energies listed in Table 2 to produce a rate coefficient for $\Delta N = 0$ DR of Fe XX forming Fe XIX in a plasma with a Maxwellian electron energy distribution at a temperature T_e . We treated all resonances listed, except for the near 0 eV $7d$ resonance, as delta functions. Using these resonances and the measured unresolved resonances near the series limit, we have produced a rate coefficient following the procedure described in Savin (1999). To this we have added the rate coefficient due to the $7d$ resonance. This rate coefficient is calculated using Equation 4 multiplied by the relative electron-ion velocity and integrating this over a Maxwellian distribution. The resulting $\Delta N = 0$ rate coefficient is shown in Figure 3(a). The inferred contribution due to the near 0 eV $15l$ and $7d$ resonances is $\approx 81\%$ at $k_B T_e = 0.1$ eV, $\approx 18\%$ at 1 eV, $\approx 4\%$ at 10 eV, and $\approx 1\%$ at 100 eV. We estimate the uncertainty in our experimentally-derived rate coefficient to be $\lesssim 20\%$ for $k_B T_e \gtrsim 1$ eV. At lower temperatures, the uncertainty of the strengths for the near 0 eV resonances causes a larger uncertainty which is difficult to quantify.

We have fitted our experimentally-derived $\Delta N = 0$ DR rate coefficient using

$$\alpha_{DR}(T_e) = T_e^{-3/2} \sum_i c_i e^{-E_i/k_B T_e} \quad (5)$$

where T_e is given in units of K. Table 3 lists the best-fit values for the fit parameters. The fit is good to better than 1.5% for $0.001 \leq k_B T_e \leq 10000$ eV. Although we infer above that the DR rate coefficient is non-zero at $k_B T_e = 0$ eV, our fitted DR rate coefficient eventually goes to 0 for $k_B T_e < 0.001$ eV. However, we expect this to have no significant effect on plasma modeling as it is extremely unlikely that Fe XX will ever form at temperatures below 0.001 eV (Kallman & Bautista 2001).

4. Theory

Existing theoretical rate coefficients for DR of Fe XX have been calculated in LS -coupling. Shull & van Steenberg (1982) present the fitted results of Jacobs et al. (1977). Arnaud & Raymond (1992) present the unpublished results of Roszman. Details of the theoretical techniques used for the calculations can be found in Jacobs et al. (1977) and Roszman (1987) and references therein.

There have been major theoretical advances in the study of DR since the works of Jacobs et al. and Roszman. We have carried out new calculations using AUTOSTRUCTURE, HULLAC, MCDF, and R-matrix methods, four different state-of-the-art theoretical techniques. Below we briefly describe these techniques and the results.

4.1. AUTOSTRUCTURE

DR cross section calculations were carried out in the independent-processes, isolated-resonance approximation using the code AUTOSTRUCTURE (Badnell 1986). This technique treats both the electron-electron (repulsive Coulomb) operator $V = \sum_{\alpha\beta} \frac{1}{|\vec{r}_\alpha - \vec{r}_\beta|}$ and the electron-photon (electric dipole) operator $\vec{D} = \sqrt{\frac{2\omega^3}{3\pi c^3}} \sum_{\alpha} \vec{r}_\alpha$ to first order. The subscripts α and β are electron labels and ω is the emitted photon energy.

All continuum wavefunctions $2l^5\epsilon l'$, and all resonance or bound wavefunctions $2l^5nl'$, were constructed within the distorted-wave approximation. The resulting wavefunctions were used to calculate all autoionization rates $\Gamma_{di}^a = 2\pi |\langle 2l_d^5 n_d l'_d | V | 2l_i^5 \epsilon_i l'_i \rangle|^2$ and radiative rates $\Gamma_{df}^r = 2\pi |\langle 2l_d^5 n_d l'_d | \vec{D} | 2l_f^5 n_f l'_f \rangle|^2$. Here the subscript i denotes the continuum states ($i = 1$ is the initial free electron plus the initial ionic system), d denotes the resonance states, and f denotes the final recombined states. Next, these rates were all used in the analytic expression for the (unconvoluted) DR cross section

$$\sigma_{DR}(E) = \sum_d \sigma_{DR}^d(E) = \sum_d \frac{2\pi^2}{k^2} \frac{(2J_d^t + 1)}{2(2J_{core} + 1)} \Gamma_{d1}^a \left[\frac{\sum_{f'} \Gamma_{df'}^r / 2\pi}{(E - E_d)^2 + \left(\frac{\sum_i \Gamma_{di}^a + \sum_f \Gamma_{df}^r}{2} \right)^2} \right] \quad (6)$$

which is a function of electron kinetic energy $E = \frac{1}{2}k^2$ relative to the initial state (e.g., $i = 1$). J_d^t is the total angular momentum of the resonance state, $J_{core} = 3/2$ the angular momentum of the $1s^2 2s^2 2p^3 ({}^4S_{3/2})$ initial core ionic state, and E_d the energy of the resonance state. The continuum wavefunctions are energy normalized such that $\langle \epsilon l | \epsilon' l' \rangle = \delta(\epsilon - \epsilon') \delta_{ll'}$. The sum over f' in the numerator only includes radiative transitions to bound states. Radiative decay to states that subsequently autoionize make rather small contributions to the DR process and are only included in the sum over f in the denominator.

For the initial atomic structure, the $1s$, $2s$, and $2p$ orbitals making up all possible $2l^5 ({}^{2S+1}L_J)$ ionic states, as well as the $2l^6$ recombined states, were determined from a Hartree-Fock (Froese-Fischer 1991) calculation for the $1s^2 2s^2 2p^3 ({}^4S)$ ground state of Fe XX. The 7 and 8 electron atomic structures were obtained by diagonalizing the appropriate Breit-Pauli Hamiltonian. Calculated ionic Fe XX energies are listed in Table 1. Prior to the final DR

cross section calculations, these ionic thresholds were shifted to the known spectroscopic values (Sugar & Corliss 1985) by $\lesssim 2.5$ eV. The $\epsilon_i l'_i$ and $n_f l'_f$ orbitals were subsequently determined from single-configuration continuum and bound distorted wave calculations, respectively. We included explicitly all orbital angular momentum and principal quantum numbers in the range $0 \leq l' \leq 17$ and $6 \leq n \leq 120$. Configuration mixing was minimal in these calculations. Only the $2l^6$ bound states were coupled to each other. All other $2l^5 n l'$ resonances, for all $n > 6$ and l' , were treated as non-interacting resonances.

The DR cross section is the sum of Lorentzian profiles. This analytic cross section can also be energy integrated to give resonance strengths or convoluted with the experimental energy distribution for comparison with the measured results. DR rate coefficients can be obtained by convolving the DR cross section with a Maxwellian electron distribution.

4.2. HULLAC

DR resonance strengths are calculated in the independent processes, isolated resonance, and low-density approximations. The DR cross section can then be written as the product of the cross section for dielectronic capture and the branching ratio for subsequent radiative stabilization. In the low-density limit, the branching ratio includes only radiative and autoionization decays. Basic atomic quantities are obtained using the multi-configuration HULLAC (Hebrew University Lawrence Livermore Atomic Code) computer package (Bar-Shalom et al. 2001). The calculations employ a relativistic parametric potential method for the atomic energy levels (Klapisch 1971; Klapisch et al. 1977) while using first order perturbation theory for the radiative decay rates. The autoionization rates are calculated in the distorted wave approximation, implementing a highly efficient factorization-interpolation method (Bar-Shalom et al. 1988; Oreg et al. 1991). Full configuration mixing is included within and between the configuration complexes $1s^2 2l^5 n' l' (n' \leq 6)$. For the $1s^2 2l^5 n' l' (n' > 6)$ complexes, only mixings within a given n' -complex are included. Mixing between complexes with different n' values for $n' > 6$ has only a minor effect and is neglected.

All of the dielectronic capture channels from the Fe XX ground level $1s^2 2s^2 2p^3 \ ^4S_{3/2}^o$ to the Fe XIX doubly excited levels $1s^2 2l^5 n' l'$ are included. These include the fine-structure core excitations (i.e., $2p_{1/2} - 2p_{3/2}$ core transitions). Explicit calculations are performed for $6 \leq n' \leq 25$, and $l' \leq 9$. DR contributions from $1s^2 2l^5 n' l' (n' > 25)$ configurations are estimated by applying the n'^{-3} scaling law to the individual autoionization and radiative transition rates when the n' electron is involved. Calculated Fe XX energy levels are listed in Table 1. These correspond to the various series limit energies for $\Delta N = 0$ DR. Prior to the final DR cross section calculations, the theoretical resonance energies have been adjusted

by $\lesssim 2.1$ eV so that the series limits match the spectroscopically measured energies (Sugar & Corliss 1985). All possible autoionization processes to $1s^22l^5$ levels following the initial dielectronic capture are accounted for, including those to excited states. All of the radiative decays to non-autoionizing levels are included in the branching ratio. Radiative cascades to autoionizing levels, on the average, can be shown to have little effect on the calculated branching ratios (Behar et al. 1995, 1996). Throughout this work only the electric dipole radiative transitions are computed. The calculated DR cross sections are folded with a Maxwellian distribution of the plasma electrons to obtain the DR rate coefficients.

4.3. Multiconfiguration Dirac-Fock (MCDF)

DR calculations are carried out in the independent process, isolated resonance approximation (Seaton & Storey 1976). In these approximations, the interference between DR and RR is neglected and the effects of interacting resonances are ignored. The DR cross section can then be written as a product of the resonance capture cross section and the stabilizing radiative branching ratio. The required energy levels and Auger and radiative transition rates for the autoionizing states are obtained using the Multiconfiguration Dirac-Fock (MCDF) method (Grant et al. 1980; Chen 1985). These calculations are carried out in the average-level scheme and in intermediate coupling with configuration interaction within the same principal quantum n complex. All possible Coster-Kronig channels and radiative decays to bound states are included. A one-step cascade correction is taken into account when the radiative decay of the core electron leads to an autoionizing state.

We include excitation from the ground state $1s^22s^22p^3\ ^4S_{3/2}$ to the $1s^22s^22p^3\ ^2P$, 2D and $1s^22s2p^4\ ^4P$, 2D , 2S , and 2P states. For fine-structure core excitations (i.e., $2p_{1/2} - 2p_{3/2}$ core transitions), explicit calculations are performed for $12 \leq n \leq 35$, and $l \leq 12$ autoionizing states. For $2s - 2p$ core excitations, explicit calculations are carried out for $6 \leq n \leq 35$, and $l \leq 12$ states. Contributions from $l > 12$ have been estimated by extrapolating from the $l = 10 - 12$ results. The contributions contribute $< 1\%$ to the total DR rate coefficient and are neglected in the final calculations. Calculated Fe XX energy levels are listed in Table 1. These correspond to the various series limit energies for $\Delta N = 0$ DR. Prior to the final DR cross section calculations, the theoretical resonance energies have been adjusted by $\lesssim 1.5$ eV so that the series limits match the spectroscopically determined excitation energies (Sugar & Corliss 1985). The DR cross sections for $36 \leq n \leq 120$ states are estimated by using the n^{-3} scaling law for the transition rates. DR cross sections with $6 \leq n \leq 120$ have been folded with the Maxwellian distribution of the plasma electrons to obtain the DR rate coefficients.

4.4. R-Matrix

We have also carried out calculations using the Belfast R-matrix codes for the inner region (Burke & Berrington 1993; Berrington et al. 1995) and a modified version of the STGF code for the outer region (Berrington et al. 1987). These include spin-orbit and other Breit-Pauli corrections (Scott & Taylor 1982), and have been extensively modified to include radiation damping (Robicheaux et al. 1995; Gorczyca et al. 1995, 1996), which is crucial for the present case of Fe XX. One appealing aspect of the R-Matrix technique is that the continua and resonances are coupled together as a structured continuum, unlike the perturbative methods that compute resonance and continuum distorted wave orbitals separately. This is achieved somewhat differently depending on the region of configuration space. Inside the so-called R-matrix “box” the total 8 electron wavefunction of Fe XIX is expanded in a large basis, making no distinction between resonance or continuum states. The surface amplitudes at r_a , compactly represented by the R-matrix, are determined from variational considerations. The radius of the “box” used here, $r_a = 2.2$ a.u., was chosen in order to include all $2p^53l$ bound states. Outside the R-matrix box, the continua and resonances are initially treated as separate Coulomb functions, but are then coupled by the long-range non-Coulombic potential, giving off-diagonal elements to the open-closed scattering matrix of multi-channel quantum defect theory (MQDT). Thus, the outer region wavefunction is also made up of structured continua, once physical boundary conditions are applied. Note that we find the long-range coupling to significantly affect the calculated DR cross section (Gorczyca et al. 1996).

In order to describe how the subsequent radiation from these structured continua are included in the present treatment, it helps to first show all included direct (RR) and resonant (DR) pathways leading to recombination for the case of Fe XX:

$$e^- + 2s^22p^3(^4S) \quad \rightarrow \quad \rightarrow 2s^22p^3(^4S_{3/2})n'l' \quad (2 \leq n' \leq 3) \quad (7)$$

$$\quad \rightarrow 2l^5nl \quad \rightarrow 2l^5n'l' \quad (2 \leq n' \leq 3) \quad (8)$$

$$\quad \rightarrow \quad \rightarrow 2s^22p^3(^4S_{3/2})n'l' \quad (4 \leq n' \leq 120) \quad (9)$$

$$\rightarrow 2s2p^4nl \quad \rightarrow 2s^22p^3nl \quad (6 \leq n \leq 120) \quad (10)$$

$$\rightarrow 2s2p^4nl \quad \rightarrow 2s2p^4n'l \pm 1 \quad (4 \leq n' \lesssim 5) \quad (11)$$

$$\rightarrow 2s^22p^{3*}nl \quad \rightarrow 2s^22p^{3*}n'l \pm 1 \quad (4 \leq n' \lesssim 16). \quad (12)$$

In the above pathways, the stabilizing photon emitted has been omitted. In Equation 10, the $2s2p^4nl \rightarrow 2s^22p^3nl$ radiative transition may leave the core in either its ground state or an excited state. In Equations 11 and 12, the \lesssim symbols indicate that the exact maximum value of n' depends on the specific configuration of the core electrons. This value of n' can be determined from Equation 1 for the different core configurations. The notation $2p^{3*}$ indicates

that the $2p^3$ electrons are in an excited configuration.

The direct/resonant processes in Equations 7 and 8, end up in recombined states that reside completely in the R-matrix box. Recombination into these states is treated by using a non-local, energy-dependent, imaginary optical potential in the inner-region Hamiltonian, leading to a complex R-matrix, and therefore a non-unitary S-matrix. Thus, interference between DR and RR is naturally included here. For the direct recombination shown in Equation 9, we add a term $-i\Gamma_{RR}/2$ to the diagonal open-open elements of the scattering matrix, where Γ_{RR} is computed in the hydrogenic approximation as

$$\Gamma_{RR} = 2\pi \sum_{n'=4}^{\infty} \sum_{l,l'} |\langle \epsilon l | D | n' l' \rangle|^2 \quad (13)$$

where ϵl denotes a continuum orbital.

The RR processes in Equations 7 and 9 are also used to compute a pure RR cross section, but it is important to omit all excited states $2l^5$ and scatter from the $2s^2 2p^3 ({}^4S_{3/2})$ target alone, thereby eliminating all DR resonances. Here we used partial waves J^π from $J_{max} = 10$ to $J_{max} = 25$, for both even and odd parities π . In order to get reasonable agreement with the RR results of Arnaud & Raymond (1992), we found it necessary to use a box size big enough to enclose the $2l^5 3l'$ states in order that RR to these states was not treated hydrogenically. For these lowest-lying states, the hydrogenic approximation is less valid. Subsequent runs using a box large enough for the $n = 4$ states, and treating $n = 5$ and higher hydrogenically changed the calculated RR cross section by less than 2% (see also the similar discussion by Arnaud & Raymond 1992).

To treat the core radiative decay in Equation 10, where the valence electron acts as a spectator, we modify the effective quantum number ν in the closed-channel MQDT expression by adding a term $-i\Gamma_{core}/2$ to the core energy E_{core} used in determining ν . Here ν is a continuous variable, calculated using $E_{cm} = E_{core} - Z^2/2\nu^2$, and Γ_{core} is given by

$$\Gamma_{core} = 2\pi |\langle 2s 2p^4 | D | 2s^2 2p^3 \rangle|^2, \quad (14)$$

where $Z = 19$. We treat the valence decay in Equations 11 and 12 hydrogenically, and add a term $-i\Gamma_{valence}/2$ to the diagonal closed-closed part of the unphysical scattering matrix, where

$$\Gamma_{valence} = 2\pi \sum_{n'=4}^{16} \sum_{\pm 1} |\langle nl | D | n'(l \pm 1) \rangle|^2. \quad (15)$$

Note that there is no interference considered between the RR pathway in Equation 9 and the DR pathways in Equations 10, 11, and 12, but this is expected to be less important than

the interference occurring between Equations 7 and 8 since the RR rate is strongest to the lowest lying states, and only when the RR and DR rates to the same final recombined state are comparable will any significant interference occur.

For F VII, Ar XVI, and Fe XXV, the present type of R-matrix calculation has been shown to give results nearly identical to those from the perturbative code AUTOSTRUCTURE (Gorczyca et al. 1996; Gorczyca & Badnell 1997; Mitnik et al. 1999). However, in certain highly-sensitive cases, differences between the two codes can be seen. For DR of Li II (Saghiri et al. 1999), AUTOSTRUCTURE results were not in as good agreement with the measurements as were the R-matrix results (Price 1997). In Sc IV, AUTOSTRUCTURE calculations needed to be extended to include interference effects between RR and DR before agreement was found with R-matrix results (Gorczyca et al. 1997). One aim of the present work is to search for possible interference effects in Fe XX where they would most likely occur (i.e., to short-range final recombined states). However, for highly ionized systems, such as that studied here, the effects of interference between the RR and DR channels are unlikely to influence the computed Maxwellian rate coefficient (Pindzola, Badnell, & Griffin 1992). Indeed by comparing our AUTOSTRUCTURE calculations (which here do not include interference effects) with our R-matrix results, we find in the present case that these effects are negligible on the Maxwellian rate coefficient.

R-matrix results are expected to give rise to slightly better autoionization and/or radiative widths, compared to perturbative approaches. This is due to the more flexible R-matrix basis used to describe the wavefunction of each structured continuum (i.e., continuum with embedded resonances). The R-matrix atomic structure calculations start with the same $1s$, $2s$, and $2p$ orbitals and configurations as described in § 4.1. Hence the calculated level energies are the same as for our AUTOSTRUCTURE results and prior to the final DR cross sections calculations, these energies were shifted to the spectroscopically known values (Sugar & Corliss 1985). We also calculated the $3s$, $3p$, and $3d$ orbitals optimized on the $2s^2 2p^2 3l$ configuration-average energies. These levels were included so that the $2l^5 3l'$ final recombined states were contained in the R-matrix box (see discussion above). For the resonance and continuum states all total spin and orbital angular momenta $S^t = 0 - 2$, $L^t = 0 - 27$ (even and odd parities) were used in LS-coupling, and LS-JK recoupled to include all $J^t = 0 - 25$ (even and odd parities). A basis of 20 R-matrix orbitals was used to describe each continuum $\epsilon l'$ or bound nl' orbital.

Using the radiation-damped R-matrix approach, the photorecombination cross section is computed as the flux lost through the electron-ion scattering process. Due to the inclusion of a radiative optical potential in the R-matrix Hamiltonian (Robicheaux et al. 1995), the scattering matrix $S(E)$ is no longer unitary, and its non-orthogonality can be related to the

photorecombination cross section as

$$\sigma_{PR}(E) = \sum_d \frac{\pi}{k^2} \frac{(2J_d^t + 1)}{2(2J_{core} + 1)} \sum_{\alpha} \left\{ 1 - \sum_{\beta} S_{\alpha\beta}^*(E) S_{\alpha\beta}(E) \right\}, \quad (16)$$

where α is summed over all channels coupled to the initial ionic target state $2s^22p^3(^4S_{3/2})$ and β is summed over all open, or continuum, channels. The closed, or resonance, channels have been incorporated into this scattering information via MQDT (Seaton 1983; Aymar, Greene, & Luc-Koenig 1996). In the absence of all couplings except for the resonance-continuum terms, Equation 16 reduces to the DR term in Equation 6 plus the direct RR term and the RR/DR interference term for those final recombined states that reside in the box. If all resonance states, contained in the closed-channels, are omitted from the R-matrix expansion, Equation 16 yields just the RR cross section. These RR results are used for the non-resonant background to produce RR+DR results for our AUTOSTRUCTURE, HULLAC, and MCDF results.

In order to resolve the many very narrow resonances, whose energy positions are not known analytically, the scattering matrix $S(E)$ in Equation 16 needs to be evaluated at an enormous number of energy points. This is to be contrasted with the AUTOSTRUCTURE, HULLAC, and MCDF calculations which analytically determine the resonance energies from a distorted wave bound state eigenvalue solution, that neglects the accessible continua. For the present R-matrix results, we used 800,000 points to cover the energy range $0 \leq E \leq 120$ eV; this gave an energy-mesh spacing of 1.5×10^{-4} eV, which is comparable to the $2s2p^4nl \rightarrow 2s^22p^3nl$ core radiative decay width. MQDT methods have been used to minimize the computational work. Even with this more efficient method, however, about *two days* of CPU time was required on a dual pentium pro Linux workstation, compared to the AUTOSTRUCTURE time on the same machine of about 40 minutes.

Our R-matrix results include the effects of radiation damping. Despite many of the radiative stabilizing decays here being $\Delta N = 0$ transitions, using AUTOSTRUCTURE we find radiation damping to be extremely important for Fe XX. Near the Rydberg limits, comparing the AUTOSTRUCTURE results with and without the inclusion of the $\sum_f \Gamma_{df}^r$ term in the denominator of Equation 6, we find that there is a damping reduction by more than an order of magnitude in the convoluted cross section. Just as importantly, some of the lower- n resonances are damped by factors of 2 in the convoluted cross section. Hence, theoretical methods based on inverse-photoionization calculations will, without the inclusion of radiation damping, severely overestimate the true cross section, provided that these narrow, undamped resonances are fully resolved in the first place.

4.5. Results

We have multiplied the AUTOSTRUCTURE, HULLAC, and MCDF $\Delta N = 0$ DR cross sections with the relative electron-ion velocity and convolved the results with the TSR energy spread to produce a rate coefficient for direct comparison with our experimental results. We have done the same for the R-matrix RR cross section data and added the results to the AUTOSTRUCTURE, HULLAC, and MCDF DR data. The resulting convolved RR+DR data are shown, respectively, in Figures 1(b), 1(c), and 1(d). The R-matrix results yield a unified RR+DR cross section which we multiplied by the relative electron-ion velocity and convolved with the experimental energy spread. These results are shown in Figure 1(e).

Figure 3(b) shows the AUTOSTRUCTURE, HULLAC, and MCDF $\Delta N = 0$ DR results (for $n_{max} = 120$) convolved with a Maxwell-Boltzmann electron energy distribution. We have fitted these DR rate coefficients using Equation 5. Table 3 lists the best-fit values for the fit parameters. For $0.001 \leq k_B T_e \leq 10000$ eV, the fit is good to better than 1.5% for the AUTOSTRUCTURE results and 0.8% for the MCDF results. The fit to the HULLAC results is good to better than 0.3% for $0.01 \leq k_B T_e \leq 10000$ eV. Below 0.01 eV, the fit goes to zero faster than the calculated HULLAC rate coefficient.

Because interference between the RR and DR channels appears to be unimportant, we can also produce an R-matrix DR-only rate coefficient ($n_{max} = 120$) by subtracting the RR-only R-matrix results ($n_{max} = 120$) from the RR+DR results ($n_{max} = 120$). In figure 3(b) we show our DR-only ($n_{max} = 120$) and RR-only ($n_{max} = \infty$) results. Table 3 lists the best-fit values for the DR fit parameters. For $0.001 \leq k_B T_e \leq 10000$ eV, the fit is good to better than 1.0% for the R-matrix results. Including DR contributions from $n = 120$ to ∞ is predicted by us to have an insignificant effect below $k_B T_e = 10$ eV, and to increase our experimentally-derived DR rate coefficient by 1% at 27 eV, by 3% at 65 eV, by 5% at 268 eV, and by 5.6% at 10,000 eV.

Our RR rate coefficient ($n_{max} = \infty$) is listed in Table 4. In order to converge at energies $\lesssim 1$ eV, we found it necessary to top-up our R-matrix RR results with hydrogenic calculations of RR into $J \geq 26$ using AUTOSTRUCTURE.

5. Discussion

Table 1 gives the experimental and theoretical energies for all Fe XX $n = 2$ levels. The spectroscopically derived energies of Sugar & Corliss (1985) are listed first. Also given are the unshifted energies calculated using the AUTOSTRUCTURE, HULLAC, and MCDF techniques as well as from calculations by Bhatia et al. (1989), Donnelly et al. (1999), and

Zhang & Pradhan (2000). Our MCDF energies and the results of Zhang & Pradhan agree to within $\approx 2\%$ with the experimental values. Our AUTOSTRUCTURE, HULLAC, and R-matrix results and those of Bhatia et al. lie within $\approx 3\%$ of experiment. The energies of Donnelly et al. lie within $\approx 4\%$ of the experimental values.

AUTOSTRUCTURE, HULLAC, and MCDF calculations use a perturbative technique and yield DR resonance strengths and energies. The R-matrix calculations use a non-perturbative method and yield unified RR+DR recombination results. Comparisons of individual resonance strengths and energies between experiment and theory are most straightforward for perturbative calculations. For these results the energy-integrated resonance strength

$$S_d = \int_{E_d - \Delta E/2}^{E_d + \Delta E/2} \sigma_{DR}^d(E) dE \quad (17)$$

can be calculated in analytic form, thereby giving the contribution from each isolated resonance d . We compare our experimental results with the non-perturbative R-matrix results to the extent that is straightforwardly possible.

DR resonances are identified in Table 2 by their dominant component. AUTOSTRUCTURE, HULLAC, and MCDF results have been used as a guide in the resonance assignment. In general, unambiguous identification is possible. One clear exception is for the $2s2p^4(^4P_{3/2})7d_{3/2}$ ($J = 3$) and $2s2p^4(^4P_{3/2})7d_{5/2}$ ($J = 3$) resonances. AUTOSTRUCTURE predicts these resonances to lie, respectively, at ≈ 0.04 and ≈ 0.3 eV. MCDF predicts them at ≈ 0.3 and ≈ 0.04 eV. The ambiguity in resonance assignment is most likely due to strong mixing between these two states. HULLAC predicts the $7d_{3/2}$ resonance to occur at ≈ 0.3 eV and that the $7d_{5/2}$ level lies below the Fe XIX continuum. Our fit to the unresolved near 0 eV recombination signal suggests this latter resonance is broad and straddles the ionization threshold for Fe XIX. Whether this level lies above or below the continuum is an example of the uncertainty in the resonance energies typical for all calculations (see below).

Another example of the uncertainty in the resonance energies is shown by the unresolved near 0 eV $2s^22p^3(^2D_{5/2}^o)15l$ resonance. Our quantum defect, AUTOSTRUCTURE, and MCDF calculations find that the $15i$ is the lowest lying DR resonance for this complex. HULLAC calculates that the $15f$, g , and h levels are also DR resonances.

Figure 4 shows the ratio of the AUTOSTRUCTURE, HULLAC, and MCDF resonance energies relative to the measured resonance energies. Below 2 eV, agreement between theory and experiment is not that good, with discrepancies between theory and experiment of up to 30%, 35%, and 24% for AUTOSTRUCTURE, HULLAC, and MCDF, respectively. A visual comparison between R-matrix results and experiment finds discrepancies of up to 25% in this energy range. In Figure 5 we compare the theoretical and experimental results. The

AUTOSTRUCTURE, MCDF, and R-matrix results, largely predict the correct resonance strengths. A uniform shift of the theoretical results to lower energies would dramatically improve the agreement between theory and experiment. In the energy range shown, the HULLAC results appear to be correctly predicting some of the DR resonances and miss out on others.

An extreme example of the discrepancies of theoretical with the measured resonance energies is shown by the resonance predicted by AUTOSTRUCTURE, MCDF, and R-matrix (but not HULLAC) calculations to occur at ≈ 0.04 eV. As discussed in § 2, this resonance probably occurs at an energy below 0.015 eV, contributing to the unresolved, near 0 eV recombination signal. These discrepancies of theory with experiment below 0.8 eV makes DR of Fe XX an excellent case for testing atomic structure calculations on ions with partially filled outer shells.

For energies above 2 eV, AUTOSTRUCTURE and MCDF calculated resonance energies agree with experiment to within 2%. R-matrix energies agree with experiment to within 3%. HULLAC agrees with experiment to within 5%. The relative agreement between theory and experiment improves as the collision energy increases.

Figure 6 shows the ratio of the AUTOSTRUCTURE, HULLAC, and MCDF resonance strengths relative to the measured resonance strengths. We use the data listed in Table 2. The mean value of this ratio is $0.98 \pm 0.30(1\sigma)$ for the AUTOSTRUCTURE results, $0.90 \pm 0.33(1\sigma)$ for the HULLAC results, and $1.02 \pm 0.30(1\sigma)$ for the MCDF results. These results do not change significantly if we leave out of our analysis the weakest 10% of the measured resonances. Our R-matrix results are in good agreement with the AUTOSTRUCTURE results and show similar scatter in the theory-to-experiment ratio of resonance strengths. The mean values all lie within our estimated total experimental error limits. However, the 1σ standard deviations for these ratios show that a significant number of calculated resonance strengths fall outside the estimated relative experimental uncertainty limits of $\lesssim 10\%$.

Between 0.08 and 1 eV, AUTOSTRUCTURE, HULLAC, MCDF and R-matrix calculations all yield resonance strengths smaller than experiment. The cause of this systematic shift is unlikely to be due to our method for extracting resonance strengths from the experimental results. The spectrum between 0.08 and 1 eV is well resolved and we have a high degree of confidence in the accuracy of the fit to the measured non-resonant background which we subtract out to fit for the DR resonance strengths and energies.

Shown in Figure 7 are the resonance strength ratios for the AUTOSTRUCTURE/MCDF, HULLAC/MCDF, and HULLAC/AUTOSTRUCTURE results. The mean values of these ratios are, respectively, $0.96 \pm 0.10(1\sigma)$, $0.88 \pm 0.26(1\sigma)$, and $0.92 \pm 0.28(1\sigma)$. These results

do not change significantly if we leave out of our analysis those resonances corresponding to the weakest 10% of the measured resonances. Agreement between our AUTOSTRUCTURE and MCDF results is good, much better than it is for either calculation with experiment. Our HULLAC results are in somewhat poorer agreement with our AUTOSTRUCTURE and MCDF calculations.

A comparison between the various theoretical resonance strengths as well as with the experimental results indicates that the HULLAC methodology for calculating DR forming $2s^22p^3nl$ resonance configurations is incomplete. For example, HULLAC tends to underestimate significantly the $2s^22p^3(^2D_{3/2,5/2}^o)nl$ resonance strengths and to overestimate significantly the $2s^22p^3(^2P_{1/2,3/2}^o)nl$ ($l \geq 3$) resonance strengths. These errors are most likely due to configuration mixings induced by the parametric potential, transferring contributions from one series to another, and to the fact that HULLAC does not include the one-electron operator autoionization transitions in which the initial and final states differ by only one orbital. These interactions can increase or decrease the rate or have no effect at all. Work is underway to modify HULLAC to include the one-electron operator (Bar-Shalom 2001).

Another point of note is that the AUTOSTRUCTURE and MCDF results find a factor of ≈ 2 drop between the resonance strength for the $2s^22p^3(^2P_{1/2}^o)21l$ ($l \geq 0$) and the $2s^22p^3(^2P_{1/2}^o)22l$ ($l \geq 0$) levels. This is attributed to the opening up of the $2s^22p^3(^2P_{1/2}^o)nl \rightarrow 2s^22p^3(^2D_{5/2})+e^-$ Auger channel which reduces the radiative branching ratio by about a half. HULLAC results predict this Auger channel to open up between the $2s^22p^3(^2P_{1/2}^o)24l$ ($l \geq 0$) and $2s^22p^3(^2P_{1/2}^o)25l$ ($l \geq 0$) resonances.

There are a number of other outstanding discrepancies. Here we only call attention to the most glaring examples. HULLAC underestimates the $2s2p^4(^2P_{3/2})6d$ resonance strengths between $\approx 15 - 16$ eV. HULLAC also underestimates the resonance strength for two $2s2p^4(^2P_{3/2})6f$ resonances at 17.229 and 17.242 eV. AUTOSTRUCTURE underestimates the $2s^22p^3(^2D_{3/2}^o)17d_{3/2}$ ($J = 3$) resonance strength at ≈ 0.09 eV by a factor of ≈ 2 .

5.1. Rate Coefficients

RR calculations have been carried out using R-matrix techniques and topped up using AUTOSTRUCTURE as described above. Arnaud & Raymond (1992) have calculated the rate coefficient for RR of Fe XX and presented a fit to their results which is supposed to be valid between 10^5 and 10^8 K. Their results are plotted in Figure 3(a). We find that their rate coefficient agrees with our R-matrix results to within 10% for $k_B T_e$ of between $\approx 10^{3.4}$ and $\approx 10^{7.8}$ K.

The calculations of Jacobs et al. (1977) and Roszman (Arnaud & Raymond 1992) were carried out using perturbative techniques, but they only published Maxwellian-averaged rate coefficients. Savin et al. (1999) demonstrated that comparisons of only Maxwellian-averaged rate coefficients cannot be used reliably to distinguish between different theoretical techniques. Disagreement between experiment and theory can be used to demonstrate the inadequacy of a particular theoretical technique. However, agreement between experiment and theory can be fortuitous. A detailed comparison of resonance strengths and energies is the only way to verify the accuracy of DR rate coefficient calculations. Unfortunately, neither Jacobs et al. nor Roszman published their calculated resonance strengths and energies.

Figure 3(a) shows the theoretical $\Delta N = 0$ DR rate coefficients of Jacobs et al. as fitted by Shull & van Steenberg (1982) and of Roszman as reported by Arnaud & Raymond (1992). Fe XX is predicted to peak in fractional abundance in an optically thin, low-density photoionized plasma of cosmic abundances at $k_B T_e \approx 35$ eV (Kallman & Bautista 2001). At this temperature, our experimentally derived DR rate coefficient is a factor of ≈ 1.8 larger than the rate coefficient of Roszman and of ≈ 4 times larger than the rate coefficient of Jacobs et al. The reason for these discrepancies is most likely because these calculations did not correctly predict the DR resonance structure at the relevant energies. Also, neither calculation accounts for DR via $2p_{1/2} \rightarrow 2p_{3/2}$ core excitations. The experimentally-derived DR rate coefficient is ≈ 4 times larger than the RR rate coefficient at $k_B T_e \approx 35$ eV.

We have calculated the $\Delta N = 0$ rate coefficient for DR of Fe XX using our AUTOSTRUCTURE, HULLAC, MCDF, and R-Matrix techniques. The results are shown in Figure 3(b). For $k_B T_e \gtrsim 10$ eV, our experimental and theoretical results agree to better than $\approx 15\%$. This temperature range includes the predicted zone of formation for Fe XX in a photoionized plasma of cosmic abundances. We note that for $k_B T_e \geq 100$ eV, $N = 2 \rightarrow N' = 3$ DR begins to contribute more than 10% to the total DR rate coefficient (Arnaud & Raymond 1992). We plan to measure DR via this core excitation at a future date. Agreement below $k_B T_e \lesssim 1$ eV is difficult to quantify due to current theoretical and experimental limitation for studying resonances near 0 eV.

6. Conclusions

We have measured the resonance strengths and energies for $\Delta N = 0$ DR of Fe XX. The relative experimental uncertainty is estimated at $\lesssim 10\%$ and the total experimental uncertainty at $\lesssim 20\%$. We have also calculated resonance strengths and energies using the state-of-the art AUTOSTRUCTURE, HULLAC, MCDF, and R-matrix methods. On average we find good agreement between the theoretical and experimental resonance strengths.

However, a large number of the theoretical resonance strengths differ from the measured values by more than three times the relative experimental uncertainty limits. These discrepancies suggest errors in the calculated level populations and line emission spectrum for the recombined ions.

We have used our experimental and theoretical results to produce Maxwellian-averaged rate coefficients for $\Delta N = 0$ DR of Fe XX. For $k_B T_e \gtrsim 10$ eV (which includes the predicted temperature of formation for Fe XX in a photoionized plasma), theory and experiment agree to better than $\approx 15\%$. Apparently many of the discrepancies between the theoretical and experimental resonance strengths average away when one calculates the Maxwellian-averaged rate coefficient.

Agreement for $k_B T_e \lesssim 1$ eV is difficult to quantify due to current theoretical and experimental limitation. Published *LS*-coupling DR rate coefficients are in poor agreement with experiment for $k_B T_e \lesssim 80$ eV. Lastly, we have calculated the rate coefficient for RR of Fe XX. Our RR results are in good agreement with published calculations.

This work was supported in part by NASA High Energy Astrophysics X-Ray Astronomy Research and Analysis grant NAG5-5123 and NASA Space Astrophysics Research and Analysis Program grant NAG5-5261. Travel to and living expenses at TSR for DWS were funded by NATO Collaborative Research Grant CRG-950911. The experimental work has been supported in part by the German Federal Minister for Education and Research (BMBF) under Contract Nos. 06 GI 475, 06 GI 848, and 06 HD 854I. NRB was supported in part by PPARC through a grant (PPA/G/S/1997/00783) to the University of Strathclyde. Work performed at Lawrence Livermore National Laboratory was under the auspices of the US Department of Energy by the University of California, Lawrence Livermore National Laboratory, under Contract number W-7405-ENG-48. TWG was supported in part by the NSF through a grant to the Institute for Theoretical Atomic and Molecular Physics at Harvard University and the Smithsonian Astrophysical Observatory.

REFERENCES

- Arnaud, M., & Raymond, J. C. 1992, *ApJ*, 398, 394
- Aymar, M., Greene, C. H., & Luc-Koenig, E. 1996, *Rev. Mod. Phys.*, 68, 1015
- Babb, J. F., Habs, D., Spruch, L., & Wolf, A. 1992, *Z. Phys. D*, 23, 197
- Badnell, N. R. 1986, *J. Phys. B*, 19, 3827

- Bar-Shalom, A., Klapisch, M., & Oreg, J. 1988, *Phys. Rev. A*, 38, 1733
- Bar-Shalom, A. 2001, private communication
- Bar-Shalom, A., Klapisch, M., & Oreg, J. 2001, *J. Quant. Spectrosc. Radiat. Transfer*, in press
- Behar, E., Mandelbaum, P., Schwob, J. L., Bar-Shalom, A., Oreg, J., & Goldstein, W. H. 1995, *Phys. Rev. A*, 52, 3770
- Behar, E., Mandelbaum, P., Schwob, J. L., Bar-Shalom, A., Oreg, J., & Goldstein, W. H. 1996, *Phys. Rev. A*, 54, 3070
- Berrington, K. A., Burke, P. G., Butler, K., Seaton, M. J., Storey, P. J., Taylor, K. T., and Yan, Y. 1987, *J. Phys. B*, 20, 6379
- Berrington, K. A., Eissner, W. B., & Norrington, P. H. 1995, *Comput. Phys. Commun.*, 92, 290
- Bhatia, A. K., Seely, J. F., & Feldman, U. 1989, *At. Data Nucl. Data Tables*, 43, 99
- Burke, P. G., & Berrington, K. A. 1993, *Atomic and Molecular Processes: An R-matrix Approach*, (Bristol: IOP Publishing)
- Chen, M. H. 1985, *Phys. Rev. A*, 31, 1449
- Cheng, K. T., Kim, Y.-K., & Desclaux, J. P. 1979, *At. Data Nucl. Data Tables*, 24, 111
- Cottam, J., Kahn, S. M., Brinkman, A. C., den Herder, J. W., & Erd, C. 2001, *A&A*, 365, L277
- Donnelly, D., Bell, K. L., & Keenan, F. P. 1999, *MNRAS*, 307, 595
- Ferland, G. J., Korista, K. T., Verner, D. A., Ferguson, J. W., Kingdon, J. B., & Verner, E. M. 1998, *PASP*, 110, 761
- Froese-Fischer, C. 1991, *Comput. Phys. Commun.*, 64, 369
- Gorczyca, T. W., Robicheaux, F., Badnell, N. R., & Pindzola, M. S. 1995, *Phys. Rev. A*, 52, 3852
- Gorczyca, T. W., Robicheaux, F., Badnell, N. R., & Pindzola, M. S. 1996, *Phys. Rev. A*, 54, 2107
- Gorczyca, T. W., & Badnell, N. R. 1997, *Phys. Rev. Lett.*, 79, 2783

- Gorczyca, T. W., Pindzola, M. S., Robicheaux, F., & Badnell, N. R., 1997, *Phys. Rev. A*, 56, 4742
- Grant, I. P., McKenzie, B. J., Norrington, P. H., Mayers, D. F., & Pyper, N. C. 1980, *Comput. Phys. Commun.*, 21, 207
- Gwinner, G. et al. 2000, *Phys. Rev. Lett.*, 84, 4822
- Hess, C. J., Kahn, S. M., & Paerels, F. B. S. 1997, *ApJ*, 478, 94
- Hoffknecht, A. et al. 1998, *J. Phys. B*, 31, 2415
- Hoffknecht, A., Schippers, S., Müller, A., Gwinner, G., Schwalm, D., & Wolf, A. 2001, *Physica Scripta*, accepted
- Jacobs, V. L., Davis, J., Kepple, P. C., & Blaha, M. 1977, *ApJ*, 211, 605
- Kallman, T. R. & Bautista M. 2001, *ApJS*, 133, 221
- Kaspi, S., Brandt, W. N., Netzer, H., Sambruna, R., Chartas, G., Garmire, G. P., & Nousek, J. A. 2000, *ApJ*, 535, L17
- Kilgus, G., Habs, D., Schwalm, D., Wolf, A., Badnell, N. R., & Müller, A. 1992, *Phys. Rev. A*, 46, 5730
- Kinkhabwala, A. et al. 2001, in preparation
- Klapisch, M. 1971, *Comput. Phys. Commun.*, 2, 239
- Klapisch, M., Schwob, J. L., Fraenkel, B., & Oreg, J. 1977, *J. Opt. Soc. Am.*, 67, 148
- Lampert, A., Wolf, A., Habs, D., Kilgus, G., Schwalm, D., Pindzola, M. S., & Badnell, N. R. 1996, *Phys. Rev. A*, 53, 1413
- Marxer, H., & Spruch, L. 1991, *Phys. Rev. A*, 43, 1268
- Mitnik, D. M., Pindzola, M. S., & Badnell, N. R. 1999, *Phys. Rev. A* **59**, 3592
- Müller, A., et al. 1987, *Phys. Rev. A*, 36, 599
- Müller, A., & Wolf, A. 1997, in *Accelerator-Based Atomic Physics Techniques and Applications*, ed. S. M. Shafroth & J. C. Austin, (New York: American Institute of Physics), 147
- Oreg, J., Goldstein, W. H., Klapisch, M., & Bar-Shalom, A. 1991, *Phys. Rev. A*, 44, 1750

- Paerels, F. et al. 2000, *ApJ*, 533, L135
- Pindzola, M. S., Badnell, N. R., & Griffin, D. C. 1992, *Phys. Rev. A*, 46, 5725
- Price, A. D. 1997, Ph.D. Thesis, University of Strathclyde, UK
- Robicheaux, F., Gorczyca, T. W., Pindzola, M. S., & Badnell, N. R. 1995, *Phys. Rev. A*, 52, 1319
- Roszman, L. J. 1987, *Phys. Rev. A*, 35, 3368
- Saghiri, A. A. et al. 1999, *Phys. Rev. A*, 60, R3350.
- Savin, D. W. 1999, *ApJ*, 523, 855
- Savin, D. W. et al. 1997, *ApJ*, 489, L115
- Savin, D. W., et al. 1999, *ApJS*, 123, 687
- Savin, D. W., et al. 2000 in *Proceedings of the 12th APS Topical Conference on Atomic Processes in Plasmas*, Reno Nevada, ed. R. C. Mancini (New York: American Institute of Physics), p. 267
- Schippers, S., Bartsch, T., Brandau, C., Gwinner, G., Linkemann, J., Müller, A., Saghiri, A. A., & Wolf, A. 1998, *J. Phys. B*, 31, 4873
- Schippers, S., Bartsch, T., Brandau, C., Müller, A., Gwinner, G., Wissler, G., Beutelspacher, M., Grieser, G., & Wolf, A. 2001, *Phys. Rev. A*, 62, 022708
- Scott, N. S., & Taylor, K. T. 1982, *Comput. Phys. Commun.*, 25, 347
- Seaton, M. J., & Storey, P. J. 1976, in *Atomic Processes and Applications*, ed. P. G. Burke & B. L. Moisewitch (North-Holland, Amsterdam), 133
- Seaton, M. J. 1983, *Rep. Prog. Phys.* 46, 167
- Shull, J. M., & van Steenberg, M. 1982, *ApJS*, 48, 95; erratum *ApJS*49, 351
- Sugar, J., & Corliss, C. 1985, *J. Phys. Chem. Ref. Data*, 24, Suppl. 2
- Theodosiou, C. E., Inokuti, M., & Manson, S. T. 1986, *At. Data Nucl. Data Tables*, 35, 473
- Zhang, H. L., & Pradhan, A. K. 2000, *MNRAS*, 313, 13

Table 1. Experimental and (unshifted) theoretical energy levels (relative to the ground state) for the $n = 2$ shell of Fe XX.

Level	Energy (eV)						
	Experiment ^a	AUTOSTRUCTURE ^{b,c}	Bahtia et al. ^d	Donnelly et al. ^e	HULLAC ^b	MCDF ^b	Zhang & Pradhan ^f
$2s^2 2p^3 \ 4S_{3/2}^o$	0	0	0	0	0	0	0
$2s^2 2p^3 \ 2D_{3/2}^o$	17.1867	17.4428	17.5337	17.5652	17.3514	17.4848	17.400
$2s^2 2p^3 \ 2D_{5/2}^o$	21.8373	22.5298	22.5013	22.6023	22.4259	22.2628	21.376
$2s^2 2p^3 \ 2P_{1/2}^o$	32.2694	32.1386	32.3219	32.49241	31.9788	32.1682	32.245
$2s^2 2p^3 \ 2P_{3/2}^o$	40.0890	39.9930	40.2327	40.29434	40.0720	40.0987	39.908
$2s \ 2p^4 \ 4P_{5/2}$	93.3266	92.9521	93.1364	93.43567	93.4074	93.2280	93.198
$2s \ 2p^4 \ 4P_{3/2}$	101.769	101.1239	101.429	101.5764	101.5300	101.906	101.30
$2s \ 2p^4 \ 4P_{1/2}$	104.486	103.8390	104.154	104.2588	104.3240	104.592	103.99
$2s \ 2p^4 \ 2D_{3/2}$	129.262	130.0774	130.2383	130.2458	130.5768	129.635	129.91
$2s \ 2p^4 \ 2D_{5/2}$	131.220	132.2033	132.4077	132.3882	132.5973	131.506	131.65
$2s \ 2p^4 \ 2S_{1/2}$	148.193	148.8263	149.0889	149.1895	149.3152	148.891	148.595
$2s \ 2p^4 \ 2P_{3/2}$	154.042	155.5766	155.9993	155.5839	156.2177	155.532	154.967
$2s \ 2p^4 \ 2P_{1/2}$	166.144	167.3363	167.9012	167.4207	167.9513	167.437	166.799
$2p^5 \ 2P_{3/2}$	242.330	244.6941	245.6268	244.4497	245.6736	244.0624	243.455
$2p^5 \ 2P_{1/2}$	255.680	258.1554	259.2832	257.8325	258.9285	257.3803	256.768

^aSugar & Corliss (1985).

^bPresent results.

^cAlso for R-matrix results (see § 4.4.)

^dBhatia et al. (1989).

^eDonnelly et al. (1999).

^fZhang & Pradhan (2000).

Table 2. Comparison of the measured and calculated resonance energies E_d and energy-integrated cross sections S_d for Fe XX to Fe XIX $\Delta N = 0$ DR.

Dominant component	E_d (eV)				S_d (10^{-21} cm ² eV)			
	AUTOSTRUCTURE ^a	HULLAC ^a	MCDF ^a	Experiment ^{b,c}	AUTOSTRUCTURE	HULLAC	MCDF	Experiment ^b
$2s^2 2p^3(^2D_{5/2})15f^{d,e}$		6.407E-02				11435.9		
$2s^2 2p^3(^2D_{5/2})15g^{d,e}$		8.774E-02				3660.8		
$2s^2 2p^3(^2D_{5/2})15h^{d,e}$		9.276E-02				1212.3		
$2s^2 2p^3(^2D_{5/2})15i^d$	4.734E-03	9.604E-02	4.0E-04	1.163E-03	17991.0	373.1	85381	141882.0
$2s^2 2p^3(^2D_{5/2})15k^d$	5.216E-03	9.883E-02	8.0E-04	2.099E-03	7494.9	$\ll 0.1$	51801	105417.0
$2s^2 2p^3(^2D_{5/2})15l^d$	5.591E-03	0.1008	1.0E-03	2.801E-03	3633.4	$\ll 0.1$	13740	63979.5
$2s^2 2p^3(^2D_{5/2})15m^d$	5.893E-03	0.1008	1.4E-03	3.347E-03	2072.4	$\ll 0.1$	6064	25492.4
$2s^2 2p^3(^2D_{5/2})15n^d$	6.140E-03	0.1008	1.8E-03	3.783E-03	1270.4	$\ll 0.1$	3234	10574.9
$2s^2 2p^3(^2D_{5/2})15o^d$	6.347E-03	0.1008	2.0E-03	4.141E-03	720.07	$\ll 0.1$	1688	6862.1
$2s^2 2p^3(^2D_{5/2})15q^d$	6.522E-03	0.1008	2.2E-03	4.438E-03	326.65	$\ll 0.1$	735	3049.8
$2s^2 2p^3(^2D_{5/2})15r^d$	6.673E-03	0.1008	2.4E-03	4.690E-03	101.22	$\ll 0.1$	405	1756.9
$2s^2 2p^3(^2D_{5/2})15t^d$	6.804E-03	0.1008	2.6E-03	4.906E-03	15.799	$\ll 0.1$	225	1021.1
$2s2p^4(^4P_{3/2})7d_{3/2} (J = 3)^{d,e}$	0.0576			0.0030	36208.0			450000.0
$2s2p^4(^4P_{3/2})7d_{5/2} (J = 3)^{d,e}$			0.0455	0.0030			36100.0	450000.0
$2s^2 2p^3(^2D_{3/2}^o)17d_{3/2} (J = 2)$	0.0867	0.0954	0.0751		1646.7	1070.5	1745.0	
$2s^2 2p^3(^2D_{3/2}^o)17d_{3/2} (J = 1)$	0.0905	0.0985	0.0790		771.0	240.7	848.3	
$2s^2 2p^3(^2D_{3/2}^o)17d_{3/2} (J = 3)$	0.0903	0.1001	0.0794		316.0	1123.7	700.6	
$2s^2 2p^3(^2D_{3/2}^o)17d_{5/2} (J = 4)$	0.0887	0.1006	0.0810		980.4	315.7	1045.0	
$2s^2 2p^3(^2D_{3/2}^o)17d_{3/2} (J = 0)$	0.0971	0.1050	0.0861		165.9	95.5	184.0	
Blend	0.0870	0.09842	0.0783	0.0810 \pm 0.0002	3880.0	2846.1	4522.9	4956.9 \pm 96.3
$2s^2 2p^3(^2D_{3/2}^o)17d_{5/2} (J = 3)$	0.0999	0.1098	0.0913		2669.0	2005.3	2943.0	
$2s^2 2p^3(^2D_{3/2}^o)17d_{5/2} (J = 2)$	0.1099	0.1206	0.1019		2096.0	950.1	2048.0	
$2s^2 2p^3(^2D_{3/2}^o)17d_{5/2} (J = 1)$	0.1165	0.1273	0.1083		1029.2	679.4	989.6	
Blend	0.1065	0.1159	0.0977	0.1019 \pm 0.0002	5794.2	3634.8	5980.6	8020.0 \pm 147.4
$2s^2 2p^3(^2D_{3/2}^o)17f$	0.1750	0.1914	0.1678	0.1690 \pm 0.0018	2274.3	958.7	2316.8	2873.3 \pm 126.7
$2s^2 2p^3(^2D_{3/2}^o)17i (l \geq 3)$	0.1870	0.2099	0.1839	0.1906 \pm 0.0033	1565.9	57.2	1277.6	2108.4 \pm 225.8
$2s2p^4(^4P_{1/2})7p_{1/2} (J = 0)$	0.2919	0.2967	0.2749		584.1	588.5	646.3	
$2s2p^4(^4P_{1/2})7p_{1/2} (J = 1)$	0.2894	0.2997	0.2761		1845.8	1715.1	1986.0	
Blend	0.2900	0.2989	0.2758	0.2248 \pm 0.0025	2429.9	2303.6	2632.3	3101.8 \pm 56.9
$2s2p^4(^4P_{3/2})7d_{5/2} (J = 3)^d$	0.3484			0.2978 \pm 0.0002	7961.6			9250.4 \pm 99.4

Table 2—Continued

Dominant component	E_d (eV)				S_d (10^{-21} cm ² eV)			
	AUTOSTRUCTURE ^a	HULLAC ^a	MCDF ^a	Experiment ^{b,c}	AUTOSTRUCTURE	HULLAC	MCDF	Experiment ^b
$2s2p^4(^4P_{3/2})7d_{3/2}$ ($J = 3$) ^d		0.3015	0.3444	0.2978 ± 0.0002		6518.5	7089.0	9250.4 ± 99.4
$2s2p^4(^4P_{3/2})7d_{5/2}$ ($J = 2$)	0.4321	0.3841	0.4306	0.3860 ± 0.0004	4696.0	3699.3	4188.0	5344.0 ± 91.5
$2s2p^4(^4P_{1/2})7p_{3/2}$ ($J = 2$)	0.4815	0.5088	0.4834	0.4313 ± 0.0008	1810.6	1659.1	1814.0	2289.0 ± 73.0
$2s2p^4(^4P_{3/2})7d_{5/2}$ ($J = 1$)	0.5382	0.4902	0.5362	0.4955 ± 0.0004	3597.9	2560.5	3040.0	4101.6 ± 77.3
$2s2p^4(^4P_{1/2})7p_{3/2}$ ($J = 1$)	0.7646	0.7917	0.7621	0.7015 ± 0.0011	1413.2	1023.3	1255.0	1741.7 ± 64.3
$2s2p^4(^4P_{3/2})7f_{5/2}$ ($J = 1$)	1.1687	1.1100	1.1653		257.3	322.5	238.4	
$2s2p^4(^4P_{3/2})7f_{5/2}$ ($J = 2$)	1.2267	1.1679	1.2212		842.1	1024.5	941.0	
$2s2p^4(^4P_{3/2})7f_{7/2}$ ($J = 5$)	1.2407	1.1760	1.2246		1963.0	2523.9	2318.0	
Blend	1.2308	1.1684	1.2196	1.1861 ± 0.0012	3062.4	3870.9	3497.4	3014.9 ± 153.6
$2s2p^4(^4P_{3/2})7f_{5/2}$ ($J = 4$)	1.2877	1.2278	1.2741		1548.3	1696.3	1731.0	
$2s2p^4(^4P_{3/2})7f_{5/2}$ ($J = 3$)	1.3035	1.2405	1.2916		1180.7	1424.0	1356.0	
Blend	1.2945	1.2336	1.2818	1.2361 ± 0.0022	2729.0	3120.3	3087.0	2855.1 ± 147.0
$2s2p^4(^4P_{3/2})7f_{7/2}$ ($J = 2$)	1.3602	1.3009	1.3501		794.7	736.8	837.8	
$2s2p^4(^4P_{3/2})7f_{7/2}$ ($J = 4$)	1.3704	1.3062	1.3542		1453.4	1563.1	1629.0	
$2s2p^4(^4P_{3/2})7f_{7/2}$ ($J = 3$)	1.4047	1.3458	1.3934		1101.1	1069.4	1181.0	
Blend	1.3793	1.3176	1.3659	1.3103 ± 0.0008	3349.4	3369.3	3647.8	4025.0 ± 80.5
$2s2p^4(^4P_{3/2})7g_{7/2}$ ($J = 2$)	1.4342	1.3752	1.4252		183.35	183.3	162.2	
$2s2p^4(^4P_{3/2})7g_{9/2}$ ($J = 3$)	1.4545	1.3927	1.4420		471.6	465.4	425.1	
$2s2p^4(^4P_{3/2})7g_{7/2}$ ($J = 5$)	1.4587	1.4002	1.4456		1031.2	1059.2	1051.0	
$2s2p^4(^4P_{3/2})7g_{9/2}$ ($J = 6$)	1.4705	1.4082	1.4542		1208.9	1272.5	1241.0	
Blend	1.4614	1.4009	1.4476	1.4270 ± 0.0009	2895.0	2980.3	2879.3	2936.8 ± 94.1
$2s2p^4(^4P_{3/2})7g_{7/2}$ ($J = 3, 4$)	1.4986	1.4471	1.4949		1453.0	1492.5	1466.1	
$2s2p^4(^4P_{3/2})7l$ ($l \geq 4$)	1.5173	1.4516	1.4985		8848.6	9162.2	8777.5	
$2s2p^4(^4P_{3/2})7g_{9/2}$ ($J = 4, 5$)	1.5214	1.4546	1.5020		1798.0	1897.6	1833.8	
Blend	1.5157	1.4515	1.4986	1.4852 ± 0.0003	12100.1	12552.3	12077.4	11738.0 ± 107.9
$2s^22p^3(^2D_{3/2}^o)18s$ ($J = 1, 2$)	1.6999	1.6869	1.6731	1.6562 ± 0.0063	31.6	27.7	40.8	104.6 ± 24.6
$2s^22p^3(^2D_{3/2}^o)18p$	1.8204	1.8212	1.8043	1.7964 ± 0.0047	91.0	70.5	94.4	147.2 ± 25.7
$2s^22p^3(^2D_{3/2}^o)18d$	1.9505	1.9616	1.9424		416.4	295.3	411.8	

Table 2—Continued

Dominant component	E_d (eV)				S_d (10^{-21} cm ² eV)			
	AUTOSTRUCTURE ^a	HULLAC ^a	MCDF ^a	Experiment ^{b,c}	AUTOSTRUCTURE	HULLAC	MCDF	Experiment ^b
$2s2p^4(^2S_{1/2})6s$ ($J = 1$)	2.0269	2.0808	1.9620		256.8	288.7	339.7	
Blend	1.9796	2.0205	1.9513	1.9398 ± 0.0022	673.2	584.0	751.5	703.0 ± 30.4
$2s^22p^3(^2D_{3/2}^o)18l$ ($l \geq 3$)	2.0178	2.0312	2.0120		289.1	79.6	274.7	
$2s^22p^3(^2D_{5/2}^o)16s$ ($J = 2, 3$)	2.1845	2.2154	2.1430		47.9	54.2	61.9	
Blend	2.0415	2.1058	2.0361	2.0101 ± 0.0025	337.0	133.8	336.6	409.6 ± 30.7
$2s^22p^3(^2P_{1/2}^o)13s$	2.2733	2.3486	2.2686		18.6	21.8	18.8	
$2s^22p^3(^2D_{5/2}^o)16p$	2.3585	2.4070	2.3354		134.2	120.2	132.1	
$2s2p^4(^2S_{1/2})6s$ ($J = 0$)	2.4620	2.5244	2.4147		71.1	75.4	90.5	
Blend	2.3943	2.4419	2.3599	2.3264 ± 0.0038	205.3	217.4	241.4	254.3 ± 26.9
$2s^22p^3(^2D_{5/2}^o)16d$	2.5482	2.6107	2.5358	2.5305 ± 0.0017	605.7	520.0	573.4	589.0 ± 21.9
$2s^22p^3(^2P_{1/2}^o)13p_{1/2}$ ($J = 1$)	2.5758	2.6593	2.5739		12.2	18.0	11.1	
$2s^22p^3(^2D_{5/2}^o)16f$	2.6283	2.6975	2.6245		273.8	265.6	277.5	
$2s^22p^3(^2P_{1/2}^o)13p_{3/2}$ ($J = 1$)	2.6229	2.7096	2.6247		23.7	18.0	24.8	
$2s^22p^3(^2P_{1/2}^o)13p_{3/2}$ ($J = 2$)	2.6306	2.7174	2.6319		31.9	25.5	33.3	
$2s2p^4(^4P_{1/2})7d_{3/2}$ ($J = 2$)	2.7002	2.7144	2.6955		433.0	380.8	434.8	
$2s2p^4(^4P_{1/2})7d_{3/2}$ ($J = 1$)	2.7202	2.7384	2.7224		342.1	266.0	320.3	
Blend	2.6837	2.7153	2.6805	2.6387 ± 0.0008	1116.7	973.9	1110.6	1166.9 ± 17.5
$2s^22p^3(^2D_{5/2}^o)16l$ ($l \geq 4$)	2.6466	2.7207	2.6426		232.1	249.8	197.8	
$2s^22p^3(^2P_{1/2}^o)13p_{1/2}$ ($J = 0$)	2.6512	2.7351	2.6502		8.0	6.3	8.8	
$2s2p^4(^4P_{1/2})7d_{5/2}$ ($J = 3$)	2.7864	2.7968	2.7742		780.0	633.7	752.3	
Blend	2.7535	2.7750	2.7459	2.7131 ± 0.0009	1020.1	889.8	958.9	827.9 ± 22.8
$2s^22p^3(^2P_{1/2}^o)13d$	2.9893	3.0716	2.9883	2.9826 ± 0.0018	340.4	270.4	325.8	304.9 ± 17.1
$2s^22p^3(^2P_{1/2}^o)13l$ ($l \geq 3$)	3.1745	3.2693	3.1710		144.1	351.0	134.5	
$2s2p^4(^4P_{1/2})7d_{5/2}$ ($J = 2$)	3.2834	3.3013	3.2749		853.59	552.7	735.5	
$2s^22p^3(^2D_{3/2}^o)19s$ ($J = 1, 2$)	3.3028	3.2811	3.2796		13.8	11.9	17.7	
Blend	3.2682	3.2419	3.2593	3.2214 ± 0.0012	1011.5	915.6	887.7	926.4 ± 22.0
$2s^22p^3(^2D_{3/2}^o)19p$	3.4051	3.3988	3.3895	3.3934 ± 0.0021	41.1	31.1	42.8	25.1 ± 13.1

Table 2—Continued

Dominant component	E_d (eV)				S_d (10^{-21} cm ² eV)			
	AUTOSTRUCTURE ^a	HULLAC ^a	MCDF ^a	Experiment ^{b,c}	AUTOSTRUCTURE	HULLAC	MCDF	Experiment ^b
$2s^2 2p^3(^2D_{3/2}^o)19d$	3.5157	3.5189	3.5080	3.5102 ± 0.0038	196.3	136.0	194.5	202.9 ± 19.3
$2s^2 2p^3(^2D_{3/2}^o)19l$ ($l \geq 3$)	3.5734	3.5791	3.5660	3.5704 ± 0.0055	137.0	37.3	134.1	147.2 ± 22.2
$2s2p^4(^4P_{1/2})7f_{5/2}$ ($J = 2$)	3.9787	3.9882	3.9714		281.1	323.0	321.5	
$2s2p^4(^4P_{1/2})7f_{5/2}$ ($J = 3$)	3.9867	3.9936	3.9745		390.4	454.5	448.6	
$2s2p^4(^4P_{1/2})7f_{7/2}$ ($J = 4$)	4.0096	4.0128	3.9923		491.8	560.9	562.1	
Blend	3.9945	4.0003	3.9813	3.9390 ± 0.0010	1163.3	1338.4	1332.2	1024.2 ± 16.8
$2s2p^4(^4P_{1/2})7f_{7/2}$ ($J = 3$)	4.1012	4.1122	4.0894	4.0319 ± 0.0021	378.8	317.6	395.1	379.7 ± 19.1
$2s2p^4(^4P_{1/2})7l$ ($l \geq 4$)	4.2149	4.2254	4.2035	4.1861 ± 0.0003	3006.6	3014.7	3023.7	2722.2 ± 20.9
$2s^2 2p^3(^2D_{5/2}^o)17s$	4.4533	4.4823	4.4200	4.3832 ± 0.0201	19.4	22.0	25.0	39.2 ± 15.2
$2s^2 2p^3(^2D_{5/2}^o)17p$	4.5982	4.6427	4.5787	4.5872 ± 0.0140	57.0	51.3	56.3	52.0 ± 15.1
$2s^2 2p^3(^2D_{3/2}^o)20p$	4.7568	4.7317	4.7457		25.1	18.6	26.2	
$2s^2 2p^3(^2D_{5/2}^o)17d$	4.7561	4.8011	4.7578		270.4	232.8	256.0	
$2s^2 2p^3(^2P_{3/2}^o)12s$ ($J = 1, 2$)	4.6936	4.7712	4.7820		24.4	24.1	23.3	
Blend	4.7496	4.7938	4.7591	4.7537 ± 0.0030	319.9	275.5	305.4	204.2 ± 13.5
$2s^2 2p^3(^2D_{5/2}^o)17l$ ($l \geq 3$)	4.8323	4.8887	4.8254		220.3	234.8	217.7	
$2s^2 2p^3(^2D_{3/2}^o)20l$ ($l \geq 2$)	4.8718	4.8410	4.8649		206.6	101.6	205.5	
Blend	4.8514	4.8743	4.8446	4.8490 ± 0.0022	426.9	336.4	422.7	457.1 ± 17.9
$2s^2 2p^3(^2P_{3/2}^o)12p_{1/2}$ ($J = 1$)	5.1934	5.1852	5.1924		15.2	12.3	16.3	
$2s^2 2p^3(^2P_{3/2}^o)12p_{1/2}$ ($J = 3$)	5.2155	5.2096	5.2163		4.4	14.4	6.9	
$2s^2 2p^3(^2P_{3/2}^o)12p_{1/2}$ ($J = 2$)	5.2194	5.2102	5.2171		18.7	19.0	21.3	
$2s^2 2p^3(^2P_{3/2}^o)12p_{3/2}$ ($J = 1$)	5.2312	5.2244	5.2314		13.9	11.8	14.5	
$2s^2 2p^3(^2P_{3/2}^o)12p_{3/2}$ ($J = 2$)	5.2551	5.2498	5.2570		23.0	16.9	24.5	
$2s2p^4(^2S_{1/2})6p_{1/2}$ ($J = 0$)	5.3722	5.4509	5.3409		10.2	14.0	15.1	
Blend	5.2444	5.2542	5.2445	5.2589 ± 0.0050	85.4	88.4	98.8	83.0 ± 8.6
$2s^2 2p^3(^2P_{3/2}^o)12p_{3/2}$ ($J = 0$)	5.3694	5.3629	5.3724		4.9	3.7	5.1	
$2s2p^4(^2S_{1/2})6p_{1/2}$ ($J = 1$)	5.5090	5.5892	5.4728		119.2	125.4	126.0	
Blend	5.5035	5.5827	5.4697	5.4383 ± 0.0031	124.1	129.1	131.1	92.4 ± 6.9
$2s^2 2p^3(^2P_{3/2}^o)12d$	5.7194	5.7103	5.7154	5.7240 ± 0.0019	382.7	316.8	391.4	366.6 ± 15.2

Table 2—Continued

Dominant component	E_d (eV)				S_d (10^{-21} cm ² eV)			
	AUTOSTRUCTURE ^a	HULLAC ^a	MCDF ^a	Experiment ^{b,c}	AUTOSTRUCTURE	HULLAC	MCDF	Experiment ^b
$2s2p^4(^2S_{1/2})6p_{3/2}$ ($J = 2$)	5.7870	5.9011	5.7871		151.8	156.9	158.8	
$2s^22p^3(^2D_{3/2}^o)21s$ ($J = 1, 2$)	5.8433	5.8097	5.8252		5.7	4.2	7.3	
Blend	5.7890	5.8987	5.7888	5.8059 ± 0.0092	157.5	161.1	166.1	115.7 ± 11.0
$2s^22p^3(^2D_{3/2}^o)21p$	5.9189	5.9102	5.9058		17.4	11.4	18.1	
$2s^22p^3(^2P_{3/2}^o)12f$	5.9359	5.9285	5.9333		65.7	171.9	70.2	
Blend	5.9323	5.9274	5.9277	5.8959 ± 0.0073	83.1	183.3	88.2	151.6 ± 19.3
$2s^22p^3(^2P_{3/2}^o)12l$ ($l \geq 4$)	5.9680	5.9738	5.9706		3.8	111.5	1.2	
$2s2p^4(^2S_{1/2})6p_{3/2}$ ($J = 1$)	5.9565	6.0717	5.9556		44.5	49.6	45.8	
$2s^22p^3(^2D_{3/2}^o)21l$ ($l \geq 2$)	6.0182	6.0043	6.0113		144.0	66.1	142.1	
Blend	6.0029	6.0040	5.9976	6.0351 ± 0.0041	192.3	227.2	189.1	187.1 ± 11.3
$2s^22p^3(^2D_{5/2}^o)18s$ ($J = 2, 3$)	6.3507	6.3732	6.3233	6.3075 ± 0.0185	11.4	12.7	14.7	10.9 ± 4.6
$2s^22p^3(^2D_{5/2}^o)18p$	6.4726	6.5082	6.4541		33.9	30.2	33.6	
$2s^22p^3(^2P_{1/2}^o)14s$	6.4642	6.5269	6.4599		5.2	6.2	5.2	
Blend	6.4715	6.5114	6.4549	6.4990 ± 0.0057	39.1	36.4	38.8	40.6 ± 5.5
$2s^22p^3(^2D_{5/2}^o)18l$ ($l \geq 2$)	6.6342	6.6873	6.6250		296.4	281.1	288.0	
$2s^22p^3(^2P_{1/2}^o)14p$	6.7424	6.8088	6.7416		23.4	21.4	24.0	
Blend	6.6421	6.6959	6.6340	6.6744 ± 0.0020	319.8	302.5	312.0	292.3 ± 8.4
$2s^22p^3(^2D_{3/2}^o)22l$ ($l \geq 0$)	7.0023	6.9749	6.9904		120.0	58.1	125.1	
$2s^22p^3(^2P_{1/2}^o)14d$	7.0360	7.1045	7.0327		115.2	93.1	110.2	
Blend	7.0188	7.0547	7.0102	7.0792 ± 0.0036	235.2	151.2	235.3	218.3 ± 11.4
$2s^22p^3(^2P_{1/2}^o)14l$ ($l \geq 3$)	7.1840	7.2638	7.1812	7.2397 ± 0.0084	50.0	124.4	47.0	58.8 ± 10.9
$2s2p^4(^2P_{3/2})6s$ ($J = 1, 2$)	7.9915	8.0245	7.9186		211.8	243.5	288.0	
$2s^22p^3(^2D_{3/2}^o)23l$ ($l \geq 0$)	7.8658	7.8369	7.9228		96.4	43.3	85.1	
Blend	7.9522	7.9962	7.9196	7.8708 ± 0.0033	308.2	286.8	373.1	326.6 ± 14.3
$2s^22p^3(^2D_{5/2}^o)19l$ ($l \geq 0$)	8.1732	8.2139	8.1615	8.2136 ± 0.0029	233.9	209.6	230.8	253.4 ± 11.9

Table 2—Continued

Dominant component	E_d (eV)				S_d (10^{-21} cm ² eV)			
	AUTOSTRUCTURE ^a	HULLAC ^a	MCDF ^a	Experiment ^{b,c}	AUTOSTRUCTURE	HULLAC	MCDF	Experiment ^b
$s^2 2p^3(^2D_{3/2}^o)24l$ ($l \geq 0$)	8.6277	8.5996	8.6206	8.6581 ± 0.0054	77.2	30.6	78.4	72.3 ± 8.8
$2s^2 2p^3(^2D_{3/2}^o)25l$ ($l \geq 0$)	9.2999	9.4499	9.2932		63.2	20.3	64.2	
$2s2p^4(^2P_{1/2})6d_{3/2}$ ($J = 1$)	9.3639	9.4735	9.3673		94.9	103.9	103.0	
$2s2p^4(^2P_{1/2})6d_{3/2}$ ($J = 2$)	9.4730	9.5652	9.4567		205.6	178.8	195.0	
$2s^2 2p^3(^2D_{5/2}^o)20l$ ($l \leq 2$)	9.4802	9.4873	9.4659		105.5	88.8	102.0	
$2s2p^4(^2P_{1/2})6d_{5/2}$ ($J = 3$)	9.4961	9.5760	9.4703		271.1	247.3	266.0	
Blend	9.4537	9.5400	9.4360	9.4117 ± 0.0023	740.3	639.1	730.2	666.6 ± 15.1
$2s^2 2p^3(^2D_{5/2}^o)20l$ ($l \geq 3$)	9.5526	9.5784	9.5457	9.5853 ± 0.0064	66.1	68.6	67.6	65.0 ± 13.3
$2s^2 2p^3(^2P_{1/2}^o)15s$	9.8746	9.8758	9.8303		2.6	3.3	2.8	
$2s^2 2p^3(^2D_{3/2}^o)26l$ ($l \leq 1$)	9.8425	9.9739	9.8322		7.2	2.8	8.0	
$2s2p^4(^2P_{1/2})6d_{5/2}$ ($J = 2$)	9.8623	9.9524	9.8457		45.9	47.1	34.1	
Blend	9.8603	9.9488	9.8423	9.7502 ± 0.0162	55.7	53.2	44.9	59.1 ± 10.9
$2s^2 2p^3(^2D_{3/2}^o)26l$ ($l \geq 2$)	9.9043	10.052	9.8995	9.9212 ± 0.0162	45.5	13.7	45.7	53.1 ± 11.2
$2s^2 2p^3(^2P_{1/2}^o)15p$	10.083	10.105	10.060		12.6	11.7	13.2	
$2s^2 2p^3(^2P_{3/2}^o)13s$ ($J = 1, 2$)	10.092	10.198	10.085		8.7	8.8	9.0	
Blend	10.087	10.145	10.070	10.101 ± 0.029	21.3	20.5	22.2	21.0 ± 14.3
$2s^2 2p^3(^2P_{1/2}^o)15d$	10.298	10.345	10.296	10.315 ± 0.012	63.7	51.8	61.7	33.9 ± 11.8
$2s^2 2p^3(^2P_{1/2}^o)15l$ ($l \geq 3$)	10.434	10.475	10.415		27.5	69.1	27.3	
$2s^2 2p^3(^2D_{3/2}^o)27l$ ($l \geq 0$)	10.427	10.558	10.421		44.7	14.0	45.4	
$2s^2 2p^3(^2P_{3/2}^o)13p$	10.441	10.554	10.440		31.3	30.2	35.7	
$2s^2 2p^3(^2D_{5/2}^o)21s$ ($J = 2, 3$)	10.494	10.496	10.475		4.3	4.1	5.5	
Blend	10.436	10.506	10.428	10.470 ± 0.006	107.8	117.4	113.9	138.6 ± 16.8
$2s^2 2p^3(^2D_{5/2}^o)21l$ ($l \geq 1$)	10.662	10.686	10.647	10.711 ± 0.028	127.7	96.4	130.0	134.7 ± 70.4
$2s^2 2p^3(^2P_{3/2}^o)13l$ ($l \geq 2$)	10.846	11.024	10.844		185.7	247.7	196.0	
$2s^2 2p^3(^2D_{3/2}^o)28l$ ($l \geq 0$)	10.902	11.019	10.896		38.3	12.3	38.9	
Blend	10.856	11.024	10.852	10.881 ± 0.026	224.0	260.0	234.9	213.6 ± 72.5

Table 2—Continued

Dominant component	E_d (eV)				S_d (10^{-21} cm ² eV)			
	AUTOSTRUCTURE ^a	HULLAC ^a	MCDF ^a	Experiment ^{b,c}	AUTOSTRUCTURE	HULLAC	MCDF	Experiment ^b
$2s2p^4(^2P_{3/2})6p_{1/2}$ ($J = 2$)	11.208	11.278	11.169	11.099 ± 0.004	135.8	145.6	142.0	120.8 ± 12.7
$2s^22p^3(^2D_{3/2}^o)29l$ ($l \geq 0$)	11.328	11.441	11.323		33.2	10.4	33.7	
$2s2p^4(^2P_{1/2})6f$	11.435	11.508	11.406		579.7	605.5	631.0	
$2s2p^4(^2P_{3/2})6p_{1/2}$ ($J = 1$)	11.495	11.569	11.459		9.1	16.5	15.9	
$2s^22p^3(^2D_{5/2}^o)22l$ ($l \leq 1$)	11.561	11.585	11.544		13.6	7.9	14.6	
$2s2p^4(^2P_{3/2})6p_{3/2}$ ($J = 2$)	11.555	11.659	11.550		111.9	110.6	119.0	
$2s2p^4(^2P_{3/2})6p_{3/2}$ ($J = 3$)	11.586	11.698	11.579		62.6	61.8	58.9	
Blend	11.461	11.544	11.437	11.435 ± 0.001	810.1	812.7	873.1	683.9 ± 11.9
$2s^22p^3(^2D_{5/2}^o)22l$ ($l \geq 2$)	11.665	11.687	11.659		91.0	72.4	89.2	
$2s2p^4(^2P_{1/2})6g$	11.704	11.783	11.677		450.7	461.5	464.0	
$2s2p^4(^2P_{1/2})6h$	11.736	11.812	11.706		267.4	274.4	280.0	
$2s^22p^3(^2D_{3/2}^o)30l$ ($l \geq 0$)	11.713	11.818	11.707		29.0	9.1	29.4	
$2s2p^4(^2P_{3/2})6p_{3/2}$ ($J = 0$)	11.808	11.922	11.808		1.2	1.6	1.9	
Blend	11.710	11.785	11.685	11.749 ± 0.001	839.3	819.0	864.5	794.9 ± 11.1
$2s^22p^3(^2D_{3/2}^o)31l$ ($l \geq 0$)	12.061	12.158	12.056		25.5	8.0	25.9	
$2s2p^4(^2P_{3/2})6p_{3/2}$ ($J = 1$)	12.261	12.376	12.260		77.9	84.4	82.8	
Blend	12.212	12.357	12.211	12.172 ± 0.009	103.4	92.4	108.7	88.2 ± 10.5
$2s^22p^3(^2D_{3/2}^o)32l$ ($l \geq 0$)	12.664	12.468	12.371		20.1	7.1	22.9	
$2s2p^4(^4P_{5/2})8s$ ($J = 3$)	12.466	12.525	12.435		32.2	46.4	46.7	
$2s^22p^3(^2D_{5/2}^o)23l$ ($l \geq 0$)	12.520	12.541	12.511		85.0	65.2	84.7	
$2s^22p^3(^2P_{1/2}^o)16s$ ($J = 0, 1$)	12.618	12.617	12.581		1.7	2.1	1.8	
Blend	12.530	12.532	12.469	12.539 ± 0.009	139.0	120.8	156.1	168.2 ± 16.7
$2s^22p^3(^2D_{3/2}^o)33l$ ($l \geq 0$)	12.664	12.749	12.659		20.1	6.3	20.3	
$2s2p^4(^4P_{5/2})8s$ ($J = 2$)	12.749	12.814	12.721		35.1	32.9	42.5	
$2s^22p^3(^2P_{1/2}^o)16p$	12.789	12.806	12.770		8.1	7.5	8.5	
Blend	12.727	12.804	12.709	12.787 ± 0.011	63.3	46.7	71.3	50.9 ± 13.8
$2s^22p^3(^2D_{3/2}^o)34l$ ($l \geq 0$)	12.926	13.006	12.922		18.0	5.7	18.2	
$2s^22p^3(^2P_{1/2}^o)16l$ ($l \geq 2$)	13.003	13.063	12.995		58.3	78.3	58.1	

Table 2—Continued

Dominant component	E_d (eV)				S_d (10^{-21} cm ² eV)			
	AUTOSTRUCTURE ^a	HULLAC ^a	MCDF ^a	Experiment ^{b,c}	AUTOSTRUCTURE	HULLAC	MCDF	Experiment ^b
Blend	12.985	13.059	12.978	13.046 ± 0.011	76.3	84.0	76.3	87.9 ± 12.7
$2s^2 2p^3(^2D_{3/2}^o)35l$ ($l \geq 0$)	13.167	13.239	13.162		16.2	5.2	16.4	
$2s^2 2p^3(^2D_{5/2}^o)24l$ ($l \geq 0$)	13.281	13.290	13.273		70.4	47.9	70.1	
$2s^2 2p^3(^2D_{3/2}^o)36l$ ($l \geq 0$)	13.387	13.458	13.393		14.7	4.6	14.9	
Blend	13.278	13.299	13.273	13.342 ± 0.010	101.3	57.7	101.4	118.9 ± 14.5
$2s^2 2p^3(^2D_{3/2}^o)37l$ ($l \geq 0$)	13.590	13.657	13.595	13.672 ± 0.018	13.3	4.2	13.5	13.2 ± 6.8
$2s^2 2p^3(^2D_{3/2}^o)38l$ ($l \geq 0$)	13.777	13.840	13.781		12.1	3.8	12.3	
$2s2p^4(^4P_{5/2})8p_{1/2}$ ($J = 2, 3$)	13.892	13.968	13.878		79.3	82.7	83.9	
Blend	13.877	13.962	13.866	13.916 ± 0.006	91.4	86.5	96.2	113.4 ± 15.3
$2s^2 2p^3(^2D_{5/2}^o)25l$ ($l \geq 0$)	13.953	14.150	13.945		59.1	33.1	59.0	
$2s^2 2p^3(^2D_{3/2}^o)39l$ ($l \geq 0$)	13.950	14.009	13.954		11.1	3.5	11.3	
$2s2p^4(^4P_{5/2})8p_{3/2}$ ($J = 4$)	14.031	14.118	14.026		53.9	60.6	55.6	
$2s2p^4(^4P_{5/2})8p_{3/2}$ ($J = 3$)	14.105	14.191	14.097		96.7	81.6	89.7	
$2s^2 2p^3(^2D_{3/2}^o)40l$ ($l \geq 0$)	14.110	14.164	14.113		10.1	3.3	10.3	
Blend	14.042	14.155	14.033	14.082 ± 0.005	230.9	182.1	225.9	247.7 ± 16.0
$2s^2 2p^3(^2D_{3/2}^o)41l$ ($l \geq 0$)	14.258	14.310	14.261		9.3	3.0	9.5	
$2s^2 2p^3(^2P_{3/2}^o)14s$	14.283	14.377	14.277		4.9	4.9	5.0	
$2s2p^4(^4P_{5/2})8p_{3/2}$ ($J = 1$)	14.280	14.370	14.277		50.4	38.7	43.8	
$2s^2 2p^3(^2D_{3/2}^o)42l$ ($l \geq 0$)	14.396	14.445	14.398		8.6	2.8	8.7	
$2s2p^4(^4P_{5/2})8p_{3/2}$ ($J = 2$)	14.407	14.495	14.401		78.6	67.2	70.8	
Blend	14.351	14.443	14.347	14.377 ± 0.013	151.8	116.6	137.8	149.5 ± 12.9
$2s^2 2p^3(^2D_{5/2}^o)26l$ ($l \geq 0$)	14.459	14.730	14.541		50.3	27.8	50.2	
$2s^2 2p^3(^2P_{3/2}^o)14p$	14.562	14.661	14.560		17.8	17.3	20.3	
$2s^2 2p^3(^2D_{3/2}^o)43l$ ($l \geq 0$)	14.525	14.572	14.562		7.9	2.6	8.1	
$2s^2 2p^3(^2D_{3/2}^o)44l$ ($l \geq 0$)	14.644	14.689	14.646		7.3	2.4	7.5	
Blend	14.558	14.696	14.533	14.593 ± 0.010	83.3	50.1	86.1	104.1 ± 10.8
$2s^2 2p^3(^2D_{3/2}^o)nl$ ($n = 45 - 47, l \geq 0$)	14.857	14.896	14.854		19.0	6.0	19.4	
$2s^2 2p^3(^2P_{1/2}^o)17s$	14.887	14.884	14.855		1.2	1.8	1.2	

Table 2—Continued

Dominant component	E_d (eV)				S_d (10^{-21} cm ² eV)			
	AUTOSTRUCTURE ^a	HULLAC ^a	MCDF ^a	Experiment ^{b,c}	AUTOSTRUCTURE	HULLAC	MCDF	Experiment ^b
$2s^2 2p^3 (^2P_{3/2}^o) 14d$	14.865	14.966	14.861		91.7	75.5	95.4	
$2s^2 2p^3 (^2P_{3/2}^o) 14l$ ($l \geq 3$)	15.002	15.115	14.998		17.0	68.9	18.5	
$2s^2 2p^3 (^2P_{1/2}^o) 17p$	15.029	15.042	15.013		5.7	6.6	6.0	
Blend	14.888	15.030	14.885	14.936 ± 0.008	134.6	158.8	140.5	206.2 ± 12.5
$2s^2 2p^3 (^2D_{5/2}^o) 27l$ ($l \geq 0$)	15.079	15.247	15.072		43.3	24.0	43.2	
$2s 2p^4 (^2P_{3/2}) 6d_{5/2}$ ($J = 3$)	15.109	15.190	15.087		157.2	30.1	159.0	
$2s^2 2p^3 (^2D_{3/2}^o) nl$ ($n = 48 - 49$, $l \geq 0$)	15.092	15.128	15.092		10.6	3.4	10.8	
$2s^2 2p^3 (^2P_{1/2}^o) 17l$ ($l \geq 2$)	15.208	15.258	15.200		41.5	74.2	41.4	
Blend	15.119	15.237	15.103	15.094 ± 0.005	252.6	131.7	254.4	326.2 ± 13.3
$2s 2p^4 (^2P_{3/2}) 6d_{3/2}$ ($J = 2$)	15.232	15.318	15.217		126.0	26.0	122.0	
$2s^2 2p^3 (^2D_{3/2}^o) nl$ ($n = 50 - 52$, $l \geq 0$)	15.290	15.323	15.290		13.6	4.4	13.8	
$2s 2p^4 (^2P_{3/2}) 6d_{3/2}$ ($J = 3$)	15.327	15.427	15.312		146.2	76.6	155.0	
$2s 2p^4 (^2P_{3/2}) 6d_{5/2}$ ($J = 4$)	15.350	15.437	15.322		169.7	58.8	181.0	
Blend	15.308	15.411	15.290	15.290 ± 0.003	455.5	165.8	471.8	404.6 ± 10.5
$2s 2p^4 (^4P_{5/2}) 8d_{5/2}$ ($J = 4$)	15.432	15.508	15.419		74.2	76.7	77.6	
$2s 2p^4 (^4P_{5/2}) 8d_{3/2}$ ($J = 3$)	15.430	15.510	15.423		58.5	60.7	61.3	
$2s 2p^4 (^2P_{3/2}) 6d_{3/2}$ ($J = 1$)	15.449	15.538	15.440		65.3	13.3	56.4	
$2s 2p^4 (^4P_{5/2}) 8d_{3/2}$ ($J = 2$)	15.475	15.557	15.472		42.8	43.9	44.6	
$2s^2 2p^3 (^2D_{3/2}^o) nl$ ($n = 53 - 55$, $l \geq 0$)	15.496	15.524	15.494		11.3	3.7	11.5	
$2s 2p^4 (^4P_{5/2}) 8d_{5/2}$ ($J = 5$)	15.536	15.611	15.520		92.5	93.7	96.6	
$2s 2p^4 (^4P_{5/2}) 8d_{3/2}$ ($J = 1$)	15.538	15.621	15.537		26.6	26.6	27.3	
$2s^2 2p^3 (^2D_{5/2}^o) 28l$ ($l \geq 0$)	15.554	15.709	15.547		37.7	20.9	37.5	
$2s 2p^4 (^2P_{3/2}) 6d_{3/2}$ ($J = 0$)	15.634	15.715	15.614		8.0	1.5	5.3	
Blend	15.485	15.566	15.475	15.522 ± 0.003	416.9	341.0	418.1	405.3 ± 8.8
$2s 2p^4 (^4P_{5/2}) 8d_{3/2}$ ($J = 4$)	15.733	15.814	15.721		71.7	66.5	71.5	
$2s^2 2p^3 (^2D_{3/2}^o) nl$ ($n = 56 - 62$, $l \geq 0$)	15.758	15.782	15.756		19.9	6.5	20.3	
$2s 2p^4 (^2P_{3/2}) 6d_{5/2}$ ($J = 1$)	15.857	15.936	15.832		59.8	17.5	52.8	
$2s 2p^4 (^4P_{5/2}) 8d_{5/2}$ ($J = 0$)	15.912	15.988	15.900		21.6	15.7	18.7	
$2s 2p^4 (^4P_{5/2}) 8d_{5/2}$ ($J = 3$)	15.956	16.036	15.943		174.8	124.0	149.0	
$2s 2p^4 (^4P_{5/2}) 8d_{5/2}$ ($J = 1$)	15.962	16.039	15.949		79.3	55.8	67.6	
Blend	15.894	15.970	15.875	15.813 ± 0.008	427.1	286.0	379.9	470.8 ± 45.7

Table 2—Continued

Dominant component	E_d (eV)				S_d (10^{-21} cm ² eV)			
	AUTOSTRUCTURE ^a	HULLAC ^a	MCDF ^a	Experiment ^{b,c}	AUTOSTRUCTURE	HULLAC	MCDF	Experiment ^b
$2s2p^4(^2P_{3/2})6d_{5/2}$ ($J = 2$)	15.989	16.064	15.953		292.8	90.8	268.0	
$2s^22p^3(^2D_{5/2}^o)29l$ ($l \geq 0$)	15.986	16.124	15.974		29.3	18.3	32.8	
$2s2p^4(^4P_{5/2})8d_{5/2}$ ($J = 2$)	16.003	16.083	15.992		152.2	105.4	128.0	
$2s^22p^3(^2D_{3/2}^o)nl$ ($n = 63 - 71$, $l \geq 0$)	16.075	16.094	16.073		17.2	5.6	17.5	
Blend	15.996	16.079	15.970	15.992 ± 0.004	491.5	220.1	446.3	474.2 ± 40.6
$2s2p^4(^4P_{5/2})8f_{5/2}$ ($J = 4$)	16.356	16.425	16.338		80.5	96.5	89.5	
$2s2p^4(^4P_{5/2})8f_{7/2}$ ($J = 5$)	16.366	16.433	16.346		100.5	120.8	112.0	
$2s2p^4(^4P_{5/2})8f_{5/2}$ ($J = 3$)	16.368	16.439	16.353		59.2	69.2	64.8	
$2s^22p^3(^2D_{5/2}^o)30l$ ($l \geq 0$)	16.365	16.499	16.360		29.1	16.1	28.9	
$2s^22p^3(^2D_{3/2}^o)nl$ ($n = 72 - 85$, $l \geq 0$)	16.369	16.382	16.366		16.4	5.3	16.8	
$2s2p^4(^4P_{5/2})8f_{5/2}$ ($J = 2$)	16.394	16.466	16.382		33.5	37.9	35.5	
$2s2p^4(^4P_{5/2})8f_{7/2}$ ($J = 6$)	16.427	16.494	16.405		119.8	139.0	132.0	
$2s2p^4(^4P_{5/2})8f_{5/2}$ ($J = 1$)	16.435	16.497	16.413		5.6	6.9	5.7	
$2s2p^4(^4P_{5/2})8f_{5/2}$ ($J = 0$)	16.446	16.518	16.435		0.1	0.2	0.2	
$2s2p^4(^4P_{5/2})8f_{7/2}$ ($J = 4$)	16.455	16.529	16.439		81.0	71.3	80.9	
$2s2p^4(^4P_{5/2})8f_{5/2}$ ($J = 5$)	16.478	16.536	16.444		101.0	101.1	105.0	
$2s2p^4(^4P_{5/2})8f_{7/2}$ ($J = 3$)	16.478	16.551	16.462		58.7	52.1	58.2	
Blend	16.412	16.481	16.393	16.404 ± 0.004	685.4	716.4	729.5	703.9 ± 36.5
$2s2p^4(^4P_{5/2})8f_{7/2}$ ($J = 2$)	16.507	16.579	16.491		37.4	35.3	37.0	
$2s2p^4(^4P_{5/2})8f_{7/2}$ ($J = 1$)	16.526	16.598	16.511		22.7	22.3	22.5	
$2s2p^4(^4P_{5/2})8l$ ($l \geq 4$)	16.561	16.632	16.544		1672.5	1386.0	1680.0	
$2s^22p^3(^2D_{3/2}^o)nl$ ($n = 86 - 120$, $l \geq 0$)	16.680	16.688	16.685		18.6	6.1	18.1	
$2s^22p^3(^2D_{5/2}^o)31l$ ($l \geq 0$)	16.713	16.838	16.707		25.8	14.3	25.6	
$2s^22p^3(^2P_{1/2}^o)18l$ ($l \leq 1$)	16.901	16.880	16.866		3.8	4.9	5.4	
Blend	16.564	16.633	16.547	16.585 ± 0.015	1780.8	1468.9	1788.6	1766.2 ± 44.4
$2s^22p^3(^2D_{5/2}^o)32l$ ($l \geq 0$)	17.029	17.145	17.022		23.0	12.8	22.9	
$2s^22p^3(^2P_{1/2}^o)18l$ ($l \geq 2$)	17.054	17.090	17.047		31.1	40.4	31.0	
$2s2p^4(^2P_{3/2})6f_{7/2}$ ($J = 4$)	17.157	17.229	17.122		172.2	39.7	195.0	
$2s2p^4(^2P_{3/2})6f_{5/2}$ ($J = 3$)	17.159	17.242	17.134		135.8	32.9	151.0	
Blend	17.141	17.179	17.115	17.077 ± 0.003	362.1	125.8	399.9	256.5 ± 8.6

Table 2—Continued

Dominant component	E_d (eV)				S_d (10^{-21} cm ² eV)			
	AUTOSTRUCTURE ^a	HULLAC ^a	MCDF ^a	Experiment ^{b,c}	AUTOSTRUCTURE	HULLAC	MCDF	Experiment ^b
$2s2p^4(^2P_{3/2})6f_{5/2}$ ($J = 2$)	17.230	17.315	17.210		21.5	23.7	96.1	
$2s2p^4(^2P_{3/2})6f_{5/2}$ ($J = 4$)	17.299	17.386	17.274		41.3	47.5	50.3	
$2s2p^4(^2P_{3/2})6f_{7/2}$ ($J = 3$)	17.304	17.384	17.277		35.4	38.4	41.8	
$2s2p^4(^2P_{3/2})6f_{7/2}$ ($J = 5$)	17.336	17.411	17.299		36.9	42.0	45.9	
$2s^22p^3(^2D_{5/2}^o)33l$ ($l \geq 0$)	17.316	17.425	17.310		11.3	11.5	11.4	
$2s2p^4(^2P_{3/2})6f_{5/2}$ ($J = 1$)	17.394	17.481	17.377		42.1	45.3	44.9	
$2s2p^4(^2P_{3/2})6f_{7/2}$ ($J = 2$)	17.454	17.534	17.428		42.7	42.6	46.2	
Blend	17.346	17.427	17.296	17.312 ± 0.007	231.2	251.0	336.6	156.5 ± 8.8
$2s2p^4(^2P_{3/2})6l$ ($l \geq 4$)	17.555	17.640	17.553		268.9	288.5	308	
$2s^22p^3(^2D_{5/2}^o)34l$ ($l \geq 0$)	17.578	17.681	17.572		10.2	10.4	10.3	
Blend	17.556	17.641	17.554	17.544 ± 0.003	279.1	298.9	318.3	312.2 ± 10.0
$2s^22p^3(^2D_{5/2}^o)35l$ ($l \geq 0$)	17.818	17.915	17.812		9.2	9.4	9.9	39
$2s^22p^3(^2P_{3/2}^o)15l$ ($l \leq 1$)	17.866	17.910	17.846		5.2	5.5	8.3	—
$2s^22p^3(^2D_{5/2}^o)36l$ ($l \geq 0$)	18.039	18.130	18.043		8.4	8.5	9.1	
Blend	17.910	17.992	17.899	17.724 ± 0.061	22.8	23.4	27.3	63.6 ± 19.1
$2s^22p^3(^2P_{3/2}^o)15l$ ($l \geq 2$)	18.139	18.282	18.134		35.1	47.4	40.1	
$2s^22p^3(^2D_{5/2}^o)37l$ ($l \geq 0$)	18.242	18.328	18.245		7.6	7.7	8.3	
$2s^22p^3(^2D_{5/2}^o)38l$ ($l \geq 0$)	18.429	18.510	18.431		7.0	7.1	7.6	
$2s^22p^3(^2P_{1/2}^o)19l$ ($l \geq 0$)	18.594	18.628	18.584		12.8	23.3	13.3	
$2s^22p^3(^2D_{5/2}^o)39l$ ($l \geq 0$)	18.601	18.678	18.603		6.4	6.5	6.9	
Blend	18.307	18.419	18.297	18.255 ± 0.029	68.9	92.0	76.2	91.5 ± 12.1
$2s^22p^3(^2D_{5/2}^o)nl$ ($n = 40 - 44$, $l \geq 0$)	19.017	19.084	19.018	18.968 ± 0.032	25.1	25.5	27.3	26.3 ± 10.2
$2s^22p^3(^2D_{5/2}^o)nl$ ($n = 45 - 53$, $l \geq 0$)	19.737	19.783	19.732		27.7	28.1	30.1	
$2s^22p^3(^2P_{1/2}^o)20l$ ($l \geq 0$)	19.930	19.939	19.921		10.3	18.0	10.5	
$2s2p^4(^2P_{1/2})6s$ ($J = 0, 1$)	20.085	20.128	20.019		11.3	13.1	15.0	
Blend	19.857	19.907	19.845	19.913 ± 0.027	49.3	59.2	55.6	47.1 ± 11.0
$2s^22p^3(^2D_{5/2}^o)nl$ ($n = 54 - 63$, $l \geq 0$)	20.367	20.401	20.365	20.375 ± 0.021	17.5	17.7	19.0	19.1 ± 6.5
$2s^22p^3(^2P_{3/2}^o)16l$ ($l \geq 0$)	20.781	20.906	20.759		27.6	51.3	33.8	

Table 2—Continued

Dominant component	E_d (eV)				S_d (10^{-21} cm ² eV)			
	AUTOSTRUCTURE ^a	HULLAC ^a	MCDF ^a	Experiment ^{b,c}	AUTOSTRUCTURE	HULLAC	MCDF	Experiment ^b
$2s^2 2p^3 ({}^2D_{5/2}^o)nl$ ($n = 64 - 76$, $l \geq 0$)	20.807	20.833	20.803		13.0	13.2	14.2	
$2s2p^4 ({}^4P_{3/2})8s_{1/2}$ ($J = 2$)	20.941	20.865	20.912		13.0	17.5	18.2	
Blend	20.826	20.885	20.811	20.866 ± 0.022	53.6	82.0	66.2	61.1 ± 9.9
$2s^2 2p^3 ({}^2P_{1/2}^o)21l$ ($l \geq 0$)	21.080	21.089	21.072		8.4	17.5	8.6	
$2s2p^4 ({}^4P_{3/2})8s_{1/2}$ ($J = 1$)	21.157	21.088	21.131		6.5	6.2	8.0	
$2s^2 2p^3 ({}^2D_{5/2}^o)nl$ ($n = 77 - 120$, $l \geq 0$)	21.247	21.260	21.243		16.8	17.0	18.4	
Blend	21.184	21.160	21.175	21.203 ± 0.032	31.7	40.7	35.0	39.6 ± 7.8
$2s^2 2p^3 ({}^2P_{1/2}^o)22l$ ($l \geq 0$)	22.076	22.083	22.069		4.8	10.6	4.8	
$2s2p^4 ({}^4P_{3/2})8p_{1/2}$ ($J = 1$)	22.296	22.237	22.285		15.3	14.7	15.3	
$2s2p^4 ({}^4P_{3/2})8p_{1/2}$ ($J = 2$)	22.448	22.394	22.438		27.3	26.5	27.4	
$2s2p^4 ({}^4P_{3/2})8p_{3/2}$ ($J = 3$)	22.448	22.403	22.449		31.9	31.0	31.8	
Blend	22.396	22.330	22.390	22.413 ± 0.028	79.3	82.8	79.3	71.9 ± 17.7
$2s2p^4 ({}^4P_{3/2})8p_{3/2}$ ($J = 2$)	22.609	22.566	22.610		41.5	33.3	37.3	
$2s2p^4 ({}^4P_{3/2})8p_{3/2}$ ($J = 1$)	22.688	22.640	22.683		26.7	21.4	23.9	
$2s2p^4 ({}^4P_{3/2})8p_{3/2}$ ($J = 0$)	22.781	22.730	22.774		5.6	4.6	5.3	
$2s^2 2p^3 ({}^2P_{3/2}^o)17l$ ($l \leq 1$)	22.835	22.868	22.815		1.5	1.4	2.1	
Blend	22.654	22.611	22.654	22.600 ± 0.022	75.3	60.7	68.6	80.0 ± 15.3
$2s^2 2p^3 ({}^2P_{1/2}^o)23l$ ($l \geq 0$)	22.945	22.949	22.938		4.1	8.4	4.1	
$2s2p^4 ({}^2D_{3/2})7s$ ($J = 1, 2$)	22.824	23.043	22.949		1.9	2.0	2.8	
$2s^2 2p^3 ({}^2P_{3/2}^o)17l$ ($l \geq 2$)	23.017	23.114	23.004		10.6	13.9	13.0	
Blend	22.977	23.051	22.983	23.097 ± 0.065	16.6	24.3	19.9	15.1 ± 13.8
$2s2p^4 ({}^2P_{1/2})6p_{1/2}$ ($J = 0$)	23.461	23.516	23.410		0.00	0.01	0.01	
$2s2p^4 ({}^2P_{1/2})6p_{1/2}$ ($J = 1$)	23.571	23.644	23.529		2.7	2.6	2.4	
$2s2p^4 ({}^2P_{1/2})6p_{3/2}$ ($J = 2$)	23.681	23.781	23.671		0.4	0.4	0.4	
$2s2p^4 ({}^4P_{1/2})8s$ ($J = 1$)	23.678	23.673	23.680		7.7	9.2	10.7	
$2s^2 2p^3 ({}^2P_{1/2}^o)24l$ ($l \geq 0$)	23.708	23.696	23.706		3.5	6.3	3.4	
$2s2p^4 ({}^4P_{3/2})8d_{3/2}$ ($J = 0$)	23.849	23.786	23.834		6.2	4.2	3.3	
$2s2p^4 ({}^2P_{1/2})6p_{3/2}$ ($J = 1$)	23.900	23.988	23.878		10.0	10.0	8.5	
Blend	23.780	23.826	23.747	23.752 ± 0.014	30.5	30.1	28.7	34.6 ± 10.1

Table 2—Continued

Dominant component	E_d (eV)				S_d (10^{-21} cm ² eV)			
	AUTOSTRUCTURE ^a	HULLAC ^a	MCDF ^a	Experiment ^{b,c}	AUTOSTRUCTURE	HULLAC	MCDF	Experiment ^b
$2s2p^4(^4P_{3/2})8d_{3/2}$ ($J = 1$)	23.904	23.855	23.906		20.9	18.1	20.0	
$2s2p^4(^4P_{3/2})8d_{5/2}$ ($J = 4$)	23.937	23.811	23.928		45.5	44.1	47.0	
$2s2p^4(^4P_{3/2})8d_{3/2}$ ($J = 2$)	23.985	23.935	23.984		34.7	30.7	33.8	
$2s2p^4(^4P_{3/2})8d_{5/2}$ ($J = 3$)	24.027	23.975	24.021		43.7	40.5	44.7	
Blend	23.971	23.895	23.967	23.980 ± 0.007	144.8	133.4	145.5	144.1 ± 8.0
$2s2p^4(^4P_{3/2})8d_{3/2}$ ($J = 3$)	24.229	24.179	24.223		62.6	46.1	55.8	
$2s2p^4(^4P_{3/2})8d_{5/2}$ ($J = 2$)	24.289	24.238	24.284		51.3	38.5	46.4	
$2s2p^4(^4P_{3/2})8d_{5/2}$ ($J = 1$)	24.359	24.308	24.354		44.8	31.7	39.4	
$2s^22p^3(^2P_{1/2}^o)25l$ ($l \geq 0$)	24.380	24.557	24.380		3.0	4.5	2.9	
Blend	24.287	24.246	24.281	24.274 ± 0.080	161.7	120.8	144.5	132.7 ± 11.3
$2s^22p^3(^2P_{3/2}^o)18l$ ($l \geq 0$)	24.846	24.935	24.831		9.5	12.1	11.5	
$2s2p^4(^4P_{3/2})8l$ ($l \geq 3$)	24.951	24.886	24.933		806.2	846.1	858.0	41
$2s2p^4(^2D_{5/2})7s$ ($J = 2$)	25.124	25.180	25.000		0.3	0.4	0.6	
$2s2p^4(^2D_{3/2})7p_{1/2}$ ($J = 1, 2$)	25.028	25.118	25.001		1.0	1.3	1.5	
$2s2p^4(^4P_{1/2})8p_{1/2}$ ($J = 0, 1$)	25.228	25.111	25.087		18.5	18.4	19.3	
$2s2p^4(^4P_{1/2})8p_{3/2}$ ($J = 2$)	25.228	25.251	25.226		22.7	22.4	23.0	
Blend	24.961	24.901	24.943	24.978 ± 0.035	858.2	900.7	913.9	816.6 ± 137.6
$2s2p^4(^2D_{3/2})7p_{3/2}$ ($J = 0, 1, 2, 3$)	25.258	25.466	25.369		2.4	3.0	3.4	
$2s2p^4(^4P_{1/2})8p_{3/2}$ ($J = 1$)	25.416	25.438	25.410		25.3	19.7	22.6	
Blend	25.402	25.442	25.405	25.583 ± 0.017	27.7	22.7	26.0	11.0 ± 5.9
$2s^22p^3(^2P_{3/2}^o)19l$ ($l \geq 0$)	26.412	26.491	26.400	26.415 ± 0.075	7.6	9.6	9.1	21.6 ± 9.9
$2s2p^4(^4P_{1/2})8d_{3/2}$ ($J = 2$)	26.695	26.710	26.688		28.1	26.2	28.9	
$2s2p^4(^4P_{1/2})8d_{3/2}$ ($J = 1$)	26.707	26.724	26.704		21.4	18.2	20.7	
$2s2p^4(^4P_{1/2})8d_{5/2}$ ($J = 3$)	26.752	26.764	26.740		50.1	44.2	49.4	
Blend	26.726	26.740	26.717	26.742 ± 0.008	99.6	88.6	99.0	88.2 ± 6.5
$2s2p^4(^4P_{1/2})8d_{5/2}$ ($J = 2$)	27.084	27.100	27.074	27.062 ± 0.014	55.3	39.7	48.4	23.8 ± 5.5
$2s2p^4(^2P_{1/2})6d$	27.547	27.616	27.504		15.0	15.3	15.4	
$2s2p^4(^2D_{3/2})7d$	27.638	27.672	27.589		13.8	11.9	15.2	

Table 2—Continued

Dominant component	E_d (eV)				S_d (10^{-21} cm ² eV)			
	AUTOSTRUCTURE ^a	HULLAC ^a	MCDF ^a	Experiment ^{b,c}	AUTOSTRUCTURE	HULLAC	MCDF	Experiment ^b
$2s2p^4(^4P_{1/2})8l$ ($l \geq 3$)	27.667	27.674	27.650		404.4	424.4	422.0	
$2s^22p^3(^2P_{3/2}^o)20l$ ($l \geq 0$)	27.749	27.796	27.738		6.2	7.0	8.5	
Blend	27.663	27.674	27.645	27.715 ± 0.006	439.4	458.6	461.1	424.9 ± 9.4
$2s2p^4(^2D_{3/2})7l$ ($l \geq 3$)	28.707	28.943	28.853		40.5	40.6	44.1	
$2s^22p^3(^2P_{3/2}^o)21l$ ($l \geq 0$)	28.899	28.945	28.889		5.1	4.9	6.2	
$2s2p^4(^2P_{1/2})6f$	29.391	29.468	29.362		3.2	3.5	3.5	
Blend	28.772	28.981	28.890	29.001 ± 0.044	48.8	49.0	53.8	59.6 ± 15.0
$2s2p^4(^2P_{1/2})6l$ ($l = 4, 5$)	29.666	29.748	29.644		1.9	2.1	1.5	
$2s2p^4(^2D_{5/2})7d$	29.612	29.766	29.762		0.8	0.6	0.5	
$2s2p^4(^4P_{5/2})9s$	29.861	29.879	29.789		11.5	13.9	15.7	
$2s^22p^3(^2P_{3/2}^o)22l$ ($l \geq 0$)	29.895	29.939	29.886		4.3	4.1	5.2	
Blend	29.838	29.874	29.801	29.918 ± 0.019	18.5	20.7	22.9	40.4 ± 7.2
$2s^22p^3(^2P_{3/2}^o)23l$ ($l \geq 0$)	30.765	30.807	30.756		3.7	3.3	4.4	
$2s2p^4(^2D_{5/2})7l$ ($l \geq 3$)	30.800	30.849	30.765		0.8	0.7	0.7	
$2s2p^4(^4P_{5/2})9p$	30.992	31.033	30.970		91.9	83.7	89.7	
$2s^22p^3(^2P_{3/2}^o)24l$ ($l \geq 0$)	31.527	31.553	31.519		3.2	2.5	3.8	
Blend	30.999	31.038	30.980	31.038 ± 0.018	99.6	90.2	98.6	95.0 ± 13.4
$2s2p^4(^4P_{5/2})9d_{5/2}$ ($J = 4$)	31.882	31.938	31.867		21.5	21.4	22.6	
$2s2p^4(^4P_{5/2})9d_{3/2}$ ($J = 3$)	31.881	31.939	31.870		17.7	18.0	18.8	
$2s2p^4(^4P_{5/2})9d_{3/2}$ ($J = 2$)	31.912	31.972	31.904		13.4	13.4	14.1	
$2s2p^4(^4P_{5/2})9d_{5/2}$ ($J = 5$)	31.912	32.009	31.937		29.7	29.3	31.3	
$2s2p^4(^4P_{5/2})9d_{3/2}$ ($J = 1$)	31.955	32.016	31.949		8.5	8.3	8.8	
Blend	31.917	31.973	31.904	32.006 ± 0.010	90.8	90.4	95.6	78.3 ± 9.3
$2s2p^4(^4P_{5/2})9d_{3/2}$ ($J = 4$)	32.091	32.150	32.076		16.2	12.9	15.4	
$2s^22p^3(^2P_{3/2}^o)25l$ ($l \geq 0$)	32.200	32.412	32.192		2.7	2.2	3.3	
$2s2p^4(^4P_{5/2})9d_{5/2}$ ($J = 0$)	32.217	32.272	32.203		6.0	4.5	5.3	
$2s2p^4(^4P_{5/2})9d_{5/2}$ ($J = 3$)	32.247	32.304	32.232		36.2	23.9	29.7	
$2s2p^4(^4P_{5/2})9d_{5/2}$ ($J = 1$)	32.251	32.307	32.237		22.0	15.6	18.6	
$2s2p^4(^4P_{5/2})9d_{5/2}$ ($J = 2$)	32.279	32.337	32.266		38.7	27.0	32.5	
Blend	32.235	32.293	32.218	32.376 ± 0.011	121.8	86.1	104.8	105.9 ± 11.6

Table 2—Continued

Dominant component	E_d (eV)				S_d (10^{-21} cm ² eV)			
	AUTOSTRUCTURE ^a	HULLAC ^a	MCDF ^a	Experiment ^{b,c}	AUTOSTRUCTURE	HULLAC	MCDF	Experiment ^b
$2s2p^4(^4P_{5/2})9l$ ($l \geq 3$)	32.642	32.702	32.621		662.8	555.6	709.0	
$2s^22p^3(^2P_{3/2}^o)26l$ ($l \geq 0$)	32.796	32.999	32.789		1.9	1.8	2.5	
Blend	32.642	32.702	32.622	32.745 ± 0.002	664.7	557.4	711.5	621.0 ± 11.7
$2s^22p^3(^2P_{3/2}^o)nl$ ($27 \leq n \lesssim 120$, $l \geq 0$)	33.255-39.743	33.296-39.732	33.245-39.745	$33.125 - 40.089$	20.5	18.5	25.7	54.3 ± 46.6
$2s2p^4(^4P_{3/2})9s$ ($J = 1, 2$)	38.314	38.334	38.286	38.362 ± 0.091	6.5	7.6	8.6	14.4 ± 8.5
$2s2p^4(^4P_{3/2})9p$	39.383	39.433	39.374	39.412 ± 0.016	59.3	53.5	56.5	43.2 ± 6.6
$2s2p^4(^4P_{3/2})9d$	40.499	40.543	40.482	40.529 ± 0.011	116.7	100.3	115.0	98.7 ± 7.5
$2s2p^4(^4P_{1/2})9s$ ($J = 1$)	41.008	41.038	41.014		2.7	3.1	3.5	
$2s2p^4(^4P_{3/2})9l$ ($l \geq 3$)	41.079	41.142	41.062		343.2	343.8	374.5	
Blend	41.078	41.142	41.062	41.112 ± 0.003	345.9	346.9	378.0	325.5 ± 6.7
$2s2p^4(^2S_{1/2})7s$ ($J = 0, 1$)	42.023	42.073	41.974		1.0	1.2	1.4	
$2s2p^4(^4P_{1/2})9p$	42.115	42.163	42.100		25.1	23.5	24.9	
$2s2p^4(^4P_{5/2})10s$ ($J = 2, 3$)	42.154	42.155	42.127		6.1	7.3	8.1	
Blend	42.120	42.158	42.101	42.112 ± 0.041	32.2	32.0	34.4	94.8 ± 13.3
$2s2p^4(^4P_{5/2})10p$	42.976	42.993	42.955		47.9	44.2	47.1	
$2s2p^4(^4P_{1/2})9d_{3/2}$ ($J = 2$)	43.109	43.169	43.100		11.4	10.9	11.9	
$2s2p^4(^4P_{1/2})9d_{3/2}$ ($J = 1$)	43.117	43.179	43.111		8.5	7.5	8.3	
$2s2p^4(^4P_{1/2})9d_{5/2}$ ($J = 3$)	43.149	43.207	43.136		19.6	18.0	19.7	
Blend	43.046	43.082	43.031	43.104 ± 0.011	87.4	80.6	87.0	74.3 ± 6.3
$2s2p^4(^4P_{1/2})9d_{5/2}$ ($J = 2$)	43.381	43.441	43.369		18.7	13.6	16.4	
$2s2p^4(^4P_{5/2})10d$	43.776	43.784	43.747		110.3	94.0	104.0	
$2s2p^4(^4P_{1/2})9l$ ($l \geq 3$)	43.795	43.865	43.779		180.4	180.1	190.0	
Blend	43.763	43.818	43.747	43.831 ± 0.006	309.4	287.7	310.4	303.7 ± 10.4
$2s2p^4(^4P_{5/2})10l$ ($l \geq 3$)	44.176	44.208	44.152	44.241 ± 0.003	364.3	303.5	394.0	333.0 ± 9.0
$2s2p^4(^2S_{1/2})7d$	46.525	46.594	46.505	46.526 ± 0.020	3.2	2.9	3.5	9.9 ± 2.4
$2s2p^4(^2P_{3/2})7s$ ($J = 1, 2$)	47.796	47.840	47.748		3.6	4.4	5.1	
$2s2p^4(^2S_{1/2})7l$ ($l \geq 3$)	47.847	47.923	47.791		5.1	7.0	7.2	

Table 2—Continued

Dominant component	E_d (eV)				S_d (10^{-21} cm ² eV)			
	AUTOSTRUCTURE ^a	HULLAC ^a	MCDF ^a	Experiment ^{b,c}	AUTOSTRUCTURE	HULLAC	MCDF	Experiment ^b
Blend	47.826	47.891	47.777	47.865 ± 0.093	8.7	11.4	12.3	17.8 ± 4.8
$2s2p^4(^2P_{3/2})7p_{3/2}$ ($J = 1$)	50.452	50.541	50.444		1.8	2.2	2.0	
$2s2p^4(^4P_{3/2})10s$ ($J = 1, 2$)	50.603	50.605	50.579		3.3	3.9	4.3	
Blend	50.550	50.582	50.536	50.634 ± 0.079	5.1	6.1	6.3	6.3 ± 3.4
$2s2p^4(^4P_{5/2})11s$ ($J = 2, 3$)	51.194	51.180	51.169		4.0	4.8	5.3	
$2s2p^4(^4P_{3/2})10p$	51.382	51.406	51.372		31.8	29.0	30.6	
$2s2p^4(^2D_{3/2})8d_{3/2}$ ($J = 3$)	51.520	51.522	51.415		1.5	1.1	1.2	
Blend	51.367	51.379	51.344	51.346 ± 0.023	37.3	34.9	37.1	45.5 ± 4.8
$2s2p^4(^4P_{5/2})11p$	51.809	51.806	51.789	51.852 ± 0.050	30.7	28.6	30.3	36.2 ± 4.5
$2s2p^4(^2D_{3/2})8l$ ($l \geq 3$)	52.258	52.509	52.402		12.6	12.8	14.2	
$2s2p^4(^4P_{3/2})10l$ ($l \geq 2$)	52.514	52.562	52.507		285.3	283.5	303.0	
$2s2p^4(^4P_{5/2})11l$ ($l \geq 2$)	52.643	52.651	52.622		319.3	282.6	308.0	
$2s2p^4(^2P_{3/2})7d$	52.517	52.556	52.746		10.4	9.9	11.4	
Blend	52.575	52.603	52.565	52.640 ± 0.016	627.6	588.8	636.6	533.0 ± 7.3
$2s2p^4(^2P_{3/2})7l$ ($l \geq 3$)	53.695	53.773	53.678		17.5	24.7	25.0	
$2s2p^4(^4P_{1/2})10l$ ($l \leq 1$)	54.107	54.031	53.991		14.7	15.9	16.7	
Blend	53.883	53.874	53.803	53.982 ± 0.056	32.2	40.6	41.7	47.1 ± 9.5
$2s2p^4(^4P_{1/2})10d$	54.901	54.923	54.883	54.876 ± 0.033	33.7	29.7	32.8	20.8 ± 5.9
$2s2p^4(^4P_{1/2})10l$ ($l \geq 3$)	55.331	55.374	55.316	55.320 ± 0.007	118.0	122.9	126.0	147.4 ± 7.3
$2s2p^4(^4P_{5/2})12p$	58.506	58.487	58.486	58.498 ± 0.065	21.6	20.3	21.5	35.8 ± 9.6
$2s2p^4(^4P_{5/2})12l$ ($l \geq 2$)	59.151	59.142	59.132	59.210 ± 0.004	239.4	211.5	235.0	204.2 ± 6.1
$2s2p^4(^4P_{3/2})11p$	60.223	60.226	60.212	60.2 – 60.5 ^f	21.2	19.5	20.5	9.0 ± 5.0
$2s2p^4(^4P_{3/2})11d$	60.825	60.826	60.811	60.784 ± 0.040	44.4	39.3	43.3	49.1 ± 11.9
$2s2p^4(^4P_{3/2})11l$ ($l \geq 3$)	61.149	61.162	61.134	61.152 ± 0.009	162.2	162.9	177.0	148.7 ± 11.4
$2s2p^4(^4P_{1/2})11p$	62.946	62.949	62.931	62.940 ± 0.059	9.9	9.5	9.9	17.3 ± 5.1
$2s2p^4(^4P_{5/2})13s$ ($J = 2, 3$)	63.334	63.295	63.303		2.3	2.7	2.9	
$2s2p^4(^4P_{1/2})11d$	63.589	63.542	63.522		22.3	20.0	21.8	
$2s2p^4(^4P_{5/2})13p$	63.704	63.672	63.684		16.3	15.3	16.2	

Table 2—Continued

Dominant component	E_d (eV)				S_d (10^{-21} cm ² eV)			
	AUTOSTRUCTURE ^a	HULLAC ^a	MCDF ^a	Experiment ^{b,c}	AUTOSTRUCTURE	HULLAC	MCDF	Experiment ^b
Blend	63.620	63.577	63.571	63.592 ± 0.042	40.9	38.0	40.9	26.0 ± 4.9
$2s2p^4(^4P_{1/2})11l$ ($l \geq 3$)	63.866	63.883	63.851		89.4	90.4	96.2	
$2s2p^4(^4P_{5/2})13d$	64.063	64.028	64.040		24.5	32.4	35.2	
Blend	63.908	63.921	63.902	63.916 ± 0.012	113.9	122.8	131.4	112.4 ± 5.6
$2s2p^4(^4P_{5/2})13l$ ($l \geq 3$)	64.250	64.228	64.230	64.306 ± 0.005	155.5	136.7	156.0	164.6 ± 3.9
$2s2p^4(^4P_{3/2})12l$ ($l \leq 2$)	67.236	67.184	67.190	67.233 ± 0.215	47.1	44.6	48.2	42.0 ± 32.1
$2s2p^4(^4P_{3/2})12l$ ($l \geq 3$)	67.639	67.634	67.624		130.8	128.4	143.0	
$2s2p^4(^4P_{5/2})14l$ ($l \leq 1$)	67.780	67.727	67.753		14.7	14.3	15.2	
Blend	67.653	67.643	67.636	67.688 ± 0.013	145.5	142.7	158.2	142.6 ± 28.7
$2s2p^4(^4P_{5/2})14l$ ($l \geq 2$)	68.230	68.192	68.211		161.7	141.3	162.0	
$2s2p^4(^2D_{3/2})9l$ ($l \geq 2$)	68.377	68.508	68.406		8.0	10.2	11.4	
Blend	68.237	68.213	68.224	68.309 ± 0.005	169.7	151.5	173.4	156.4 ± 5.6
$2s2p^4(^4P_{1/2})12p$	69.646	69.633	69.632	69.810 ± 0.152	7.3	7.0	7.3	15.6 ± 5.6
$2s2p^4(^4P_{1/2})12l$ ($l \geq 2$)	70.310	70.310	70.298		89.6	87.0	94.7	
$2s2p^4(^2S_{1/2})8d$	70.490	70.589	70.469		1.5	1.5	1.7	
Blend	70.313	70.315	70.301	70.352 ± 0.010	91.1	88.5	96.4	90.0 ± 4.7
$2s2p^4(^2S_{1/2})8l$ ($l \geq 3$)	71.383	71.477	71.356		2.9	3.6	3.5	
$2s2p^4(^4P_{5/2})15l$ ($l \geq 0$)	71.442	71.387	71.419		150.7	133.1	154.0	
$2s2p^4(^4P_{3/2})13s$ ($J = 1, 2$)	71.778	71.738	71.750		1.4	1.6	1.7	
Blend	71.444	71.393	71.421	71.506 ± 0.005	155.0	138.3	159.2	155.0 ± 4.8
$2s2p^4(^4P_{3/2})13p$	72.127	72.099	72.115	72.273 ± 0.055	11.8	11.0	11.5	16.6 ± 3.8
$2s2p^4(^4P_{3/2})13l$ ($l \geq 2$)	72.654	72.634	72.641	72.723 ± 0.005	135.8	129.5	145.0	137.4 ± 4.6
$2s2p^4(^4P_{5/2})16l$ ($l \geq 0$)	74.098	74.031	74.076	74.172 ± 0.009	133.1	171.1	137.0	127.4 ± 5.9
$2s2p^4(^4P_{1/2})13p$	74.847	74.820	74.833		5.6	5.4	5.6	
$2s2p^4(^2P_{3/2})8p$	74.897	74.985	74.880		1.7	1.9	1.9	
Blend	74.859	74.863	74.845	74.886 ± 0.012	7.3	7.3	7.5	6.0 ± 4.1

Table 2—Continued

Dominant component	E_d (eV)				S_d (10^{-21} cm ² eV)			
	AUTOSTRUCTURE ^a	HULLAC ^a	MCDF ^a	Experiment ^{b,c}	AUTOSTRUCTURE	HULLAC	MCDF	Experiment ^b
$2s2p^4(^4P_{1/2})13l$ ($l \geq 2$)	75.373	75.356	75.360	75.420 ± 0.013	75.2	72.0	79.8	72.0 ± 5.4
$2s2p^4(^4P_{5/2})17l$ ($l \geq 0$)	76.298	76.221	76.276		116.8	117.6	123.0	
$2s2p^4(^2P_{3/2})8d$	76.424	76.498	76.392		5.3	5.3	5.9	
$2s2p^4(^4P_{3/2})14l$ ($l \leq 2$)	76.419	76.371	76.403		29.7	27.4	29.5	
Blend	76.326	76.258	76.304	76.332 ± 0.009	151.8	150.3	158.4	115.2 ± 5.5
$2s2p^4(^4P_{3/2})14l$ ($l \geq 3$)	76.696	76.662	76.680	76.727 ± 0.011	98.8	94.7	107.0	127.2 ± 5.5
$2s2p^4(^2P_{3/2})8l$ ($l \geq 3$)	77.233	77.320	77.209	77.278 ± 0.044	11.3	14.4	15.1	12.4 ± 3.9
$2s2p^4(^4P_{5/2})18l$ ($l \geq 0$)	78.140	78.055	78.119	78.218 ± 0.009	106.5	94.0	113.0	102.2 ± 5.4
$2s2p^4(^4P_{1/2})14l$ ($l \geq 0$)	79.361	79.321	79.342	79.448 ± 0.056	70.3	67.4	74.9	64.7 ± 22.2
$2s2p^4(^4P_{5/2})19l$ ($l \geq 0$)	79.699	79.612	79.678		98.4	96.5	105.0	
$2s2p^4(^2D_{3/2})10l$ ($l \geq 0$)	79.841	79.925	79.861		7.3	8.0	9.1	
$2s2p^4(^4P_{3/2})15l$ ($l \geq 0$)	79.888	79.835	79.866		111.9	107.4	120.0	
Blend	79.801	79.737	79.782	79.866 ± 0.023	217.6	211.9	233.1	197.0 ± 23.1
$2s2p^4(^4P_{5/2})20l$ ($l \geq 0$)	81.029	80.924	81.008	81.090 ± 0.008	91.7	87.7	97.4	92.0 ± 5.3
$2s2p^4(^4P_{5/2})21l$ ($l \geq 0$)	82.174	82.055	82.153	82.202 ± 0.022	86.0	76.1	91.4	86.9 ± 16.1
$2s2p^4(^4P_{3/2})16l$ ($l \geq 1$)	82.544	82.483	82.522		100.7	104.3	109.0	
$2s2p^4(^4P_{1/2})15l$ ($l \geq 1$)	82.607	82.558	82.592		62.7	59.7	66.0	
Blend	82.568	82.510	82.548	82.578 ± 0.019	163.4	164.0	175.0	148.7 ± 16.2
$2s2p^4(^4P_{5/2})22l$ ($l \geq 0$)	83.166	83.054	83.145	83.225 ± 0.012	81.1	74.5	86.3	87.2 ± 6.7
$2s2p^4(^4P_{5/2})nl$ ($23 \leq n \lesssim 120$, $l \geq 0$)	84.031-92.986	83.775-92.990	83.854-92.966		2371.6	1823.5	2487.4	
$2s2p^4(^4P_{3/2})nl$ ($17 \leq n \lesssim 120$, $l \geq 0$)	84.740-101.425	84.580-101.431	84.337-101.408		2337.2	1929.4	2419.5	
$2s2p^4(^4P_{1/2})nl$ ($16 \leq n \lesssim 120$, $l \geq 0$)	85.257-104.140	84.734-104.149	84.782-104.125		1339.8	1161.1	1396.1	
Blend	84.031-104.140	83.775-104.149	83.854-104.125	$83.600 - 104.485$	6048.6	4914.0	6303.0	5250.8 ± 55.5
$2s2p^4(^2P_{3/2})10l$ ($l \geq 2$)	104.80	104.85	104.78		10.3	10.9	12.7	
$2s2p^4(^2P_{1/2})9l$ ($l \geq 2$)	105.01	105.09	104.99		0.5	0.5	0.5	
Blend	104.81	104.86	104.79	104.98 ± 0.04	10.8	11.4	13.2	22.5 ± 5.4

Table 2—Continued

Dominant component	E_d (eV)				S_d (10^{-21} cm ² eV)			
	AUTOSTRUCTURE ^a	HULLAC ^a	MCDF ^a	Experiment ^{b,c}	AUTOSTRUCTURE	HULLAC	MCDF	Experiment ^b

^aWeighted energy: $E_d = \sum E_d S_d / \sum S_d$.

^b 1σ statistical fitting uncertainties only.

^cAbsolute energy scale uncertainty $\lesssim 0.5\%$ for $E \lesssim 25$ eV and $\lesssim 0.2\%$ for $E \gtrsim 25$ eV.

^dSee § 3 about the experimental results.

^eSee § 5 about the theoretical results.

^fUnable to fit for resonance energy.

Table 3. Rate coefficient fit parameters for $\Delta N = 0$ DR of Fe XX forming Fe XIX ($n_{max} = 120$). The units are $\text{cm}^3 \text{s}^{-1} \text{K}^{1.5}$ for c_i and eV for E_i .

Parameter	Experiment	AUTOSTRUCTURE	HULLAC	MCDF	R-matrix
c_1	8.53E-05	1.38E-05	6.25E-05	4.51E-06	9.80E-06
c_2	1.62E-04	3.29E-05	9.68E-05	2.88E-06	3.47E-05
c_3	7.71E-05	3.02E-06	2.69E-04	1.41E-04	3.25E-05
c_4	4.04E-05	1.96E-04	3.19E-04	8.29E-05	3.04E-05
c_5	1.75E-04	5.17E-04	3.08E-03	1.84E-04	1.35E-04
c_6	6.73E-04	2.49E-03	3.01E-03	5.45E-04	1.30E-04
c_7	2.85E-03	2.92E-03	7.62E-03	3.37E-03	6.57E-04
c_8	3.18E-03	2.13E-03	1.55E-02	3.98E-03	3.06E-03
c_9	1.40E-02	9.27E-03	5.97E-02	1.75E-02	3.60E-03
c_{10}	2.88E-03	9.40E-03	2.33E-03	7.44E-02	1.47E-02
c_{11}	5.78E-02	7.55E-02	...	9.05E-03	9.41E-03
c_{12}	1.26E-02	5.26E-02
c_{13}	1.30E-02
E_1	1.07E-03	1.02E-03	6.34E-02	4.04E-04	5.83E-04
E_2	4.42E-03	3.59E-03	1.01E-01	1.44E-03	3.19E-03
E_3	1.34E-02	1.40E-02	2.91E-01	4.57E-02	7.34E-03
E_4	5.00E-02	6.46E-02	5.00E-01	9.37E-02	2.71E-02
E_5	1.29E-01	2.99E-01	1.37E+00	2.49E-01	5.45E-02
E_6	3.57E-01	1.14E+00	3.67E+00	4.71E-01	1.26E-01
E_7	1.30E+00	2.86E+00	1.11E+01	1.45E+00	4.02E-01
E_8	3.29E+00	4.98E+00	2.76E+01	4.23E+00	1.35E+00

Table 3—Continued

Parameter	Experiment	AUTOSTRUCTURE	HULLAC	MCDF	R-matrix
E_9	1.33E+01	1.42E+01	8.52E+01	1.60E+01	3.69E+00
E_{10}	3.76E+01	2.04E+01	2.52E+02	7.40E+01	1.46E+01
E_{11}	6.60E+01	7.98E+01	...	2.29E+02	4.63E+01
E_{12}	2.12E+02	7.21E+01
E_{13}	1.50E+02

Table 4. R-matrix rate coefficient for RR of Fe XX forming Fe XIX as a function of plasma temperature for $n_{max} = \infty$. The R-matrix results have been topped-up using AUTOSTRUCTURE for RR into $J \geq 26$ levels.

$k_B T_e$ (eV)	Rate ($\text{cm}^3 \text{ s}^{-1}$)	$k_B T_e$ (eV)	Rate ($\text{cm}^3 \text{ s}^{-1}$)	$k_B T_e$ (eV)	Rate ($\text{cm}^3 \text{ s}^{-1}$)	$k_B T_e$ (eV)	Rate ($\text{cm}^3 \text{ s}^{-1}$)
0.001	1.347E-08	0.1	1.082E-09	10	6.071E-11	1000	1.729E-12
0.002	9.578E-09	0.2	7.277E-10	20	3.832E-11	2000	8.811E-13
0.003	7.759E-09	0.3	5.706E-10	30	2.896E-11	3000	5.814E-13
0.004	6.639E-09	0.4	4.777E-10	40	2.353E-11	4000	4.286E-13
0.005	5.871E-09	0.5	4.154E-10	50	1.995E-11	5000	3.364E-13
0.006	5.309E-09	0.6	3.699E-10	60	1.740E-11	6000	2.749E-13
0.007	4.875E-09	0.7	3.354E-10	70	1.549E-11	7000	2.311E-13
0.008	4.530E-09	0.8	3.082E-10	80	1.400E-11	8000	1.984E-13
0.009	4.249E-09	0.9	2.862E-10	90	1.280E-11	9000	1.732E-13
0.01	4.014E-09	1	2.681E-10	100	1.182E-11	10000	1.531E-13
0.02	2.769E-09	2	1.763E-10	200	6.953E-12		
0.03	2.203E-09	3	1.364E-10	300	5.020E-12		
0.04	1.861E-09	4	1.128E-10	400	3.942E-12		
0.05	1.628E-09	5	9.706E-11	500	3.249E-12		
0.06	1.460E-09	6	8.576E-11	600	2.764E-12		
0.07	1.332E-09	7	7.724E-11	700	2.405E-12		
0.08	1.231E-09	8	7.055E-11	800	2.129E-12		
0.09	1.150E-09	9	6.516E-11	900	1.909E-12		

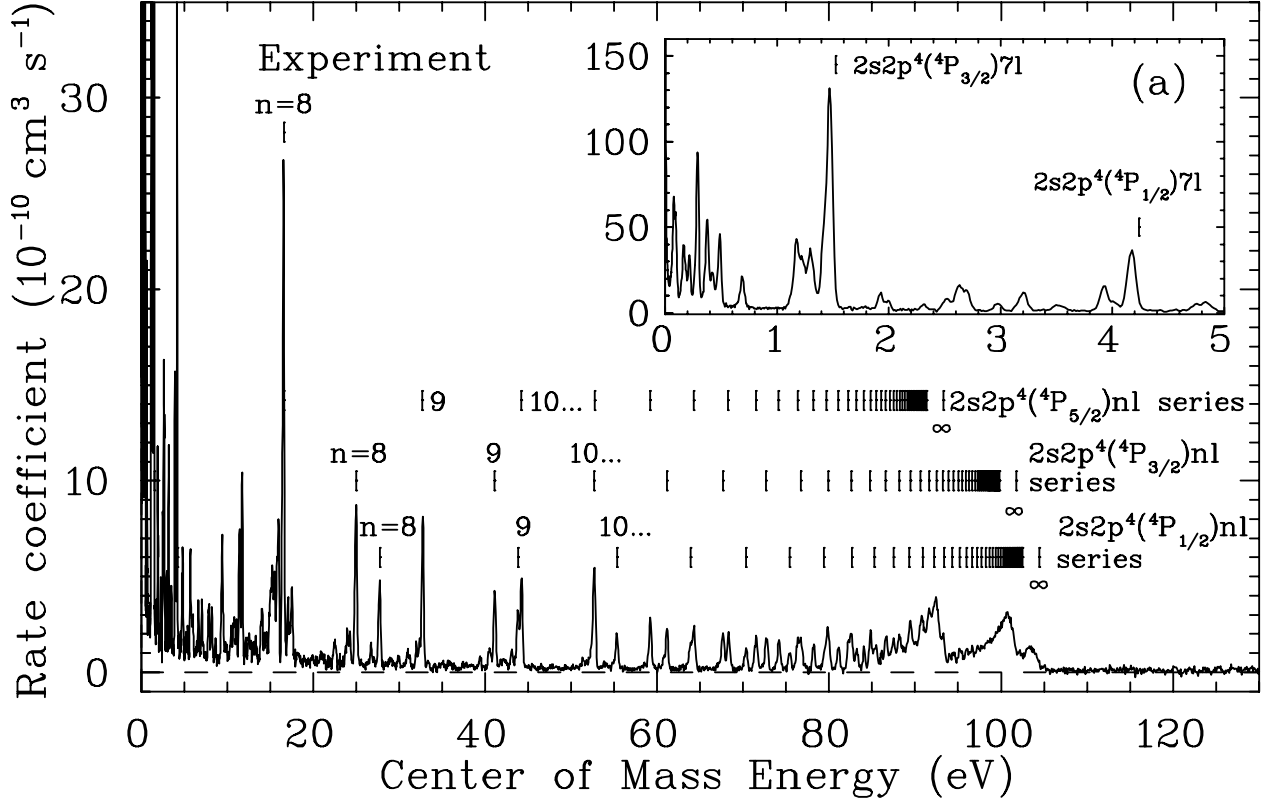


Fig. 1.— Fe XX to Fe XIX $\Delta N = 0$ DR resonance structure: (a) Experimental, (b) AUTOSTRUCTURE, (c) HULLAC, (d) MCDF, and (e) R-matrix results. The experimental and theoretical data represent the DR and RR cross sections times the electron-ion relative velocity convolved with the energy spread of the experiment (i.e., a rate coefficient) and are shown versus electron-ion center-of-mass collision energy. In (a) resonances resulting from the ${}^4S_{3/2}^o - {}^4P_{5/2}$, ${}^4S_{3/2}^o - {}^4P_{3/2}$, and ${}^4S_{3/2}^o - {}^4P_{1/2}$ core excitations are labeled for capture into high l levels. Unlabeled resonances are due to capture into low l levels or due to DR via other core excitations. Many of the unlabeled resonances below ≈ 40 eV are due to DR via $2p_{1/2} - 2p_{3/2}$ core excitations. The nonresonant “background” rate coefficient in (a) is due primarily to RR. In (b), (c), and (d) we have added the convolved, non-resonant RR contribution obtained from our R-matrix calculations to our DR results.

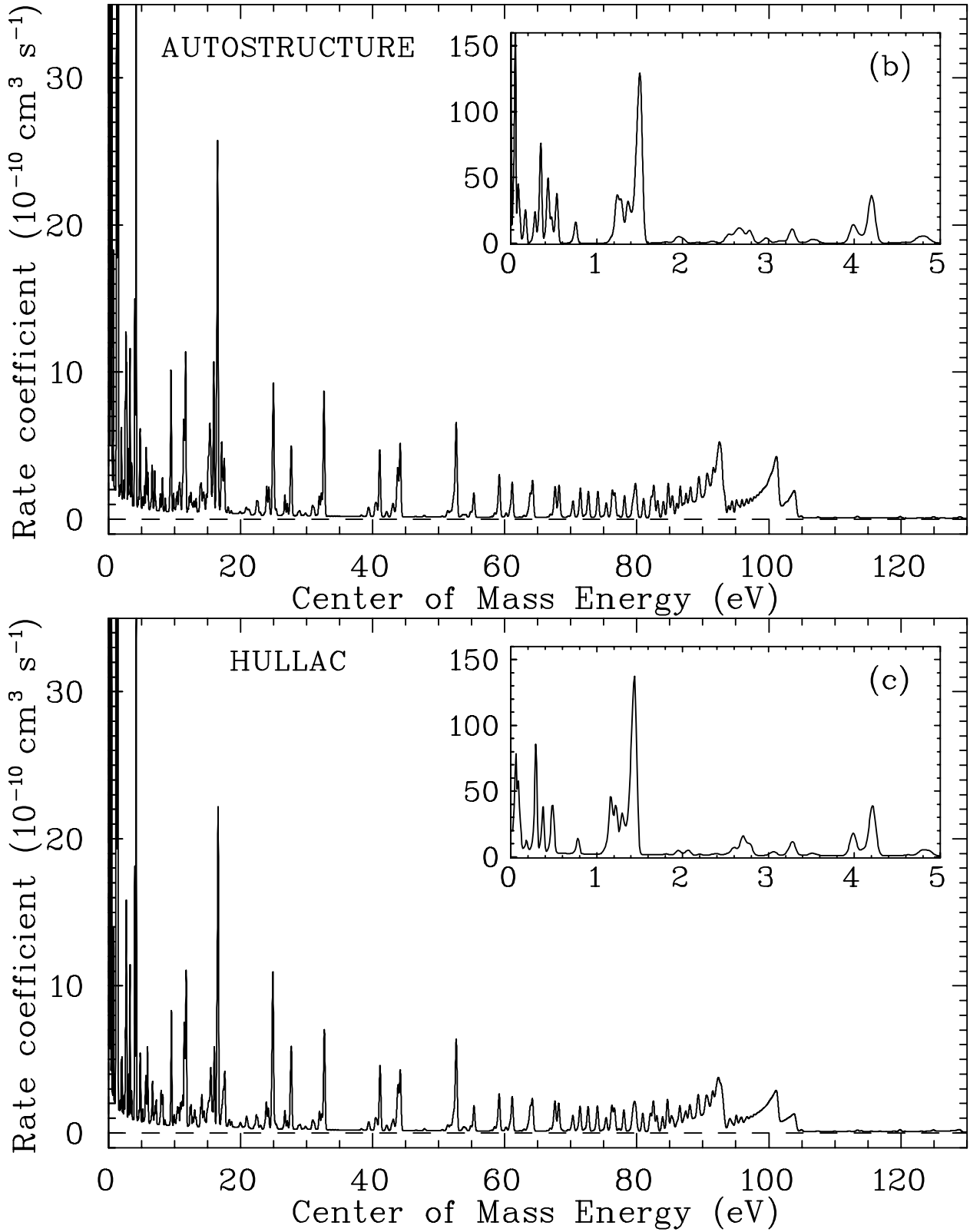


Fig. 1.— *Continued*

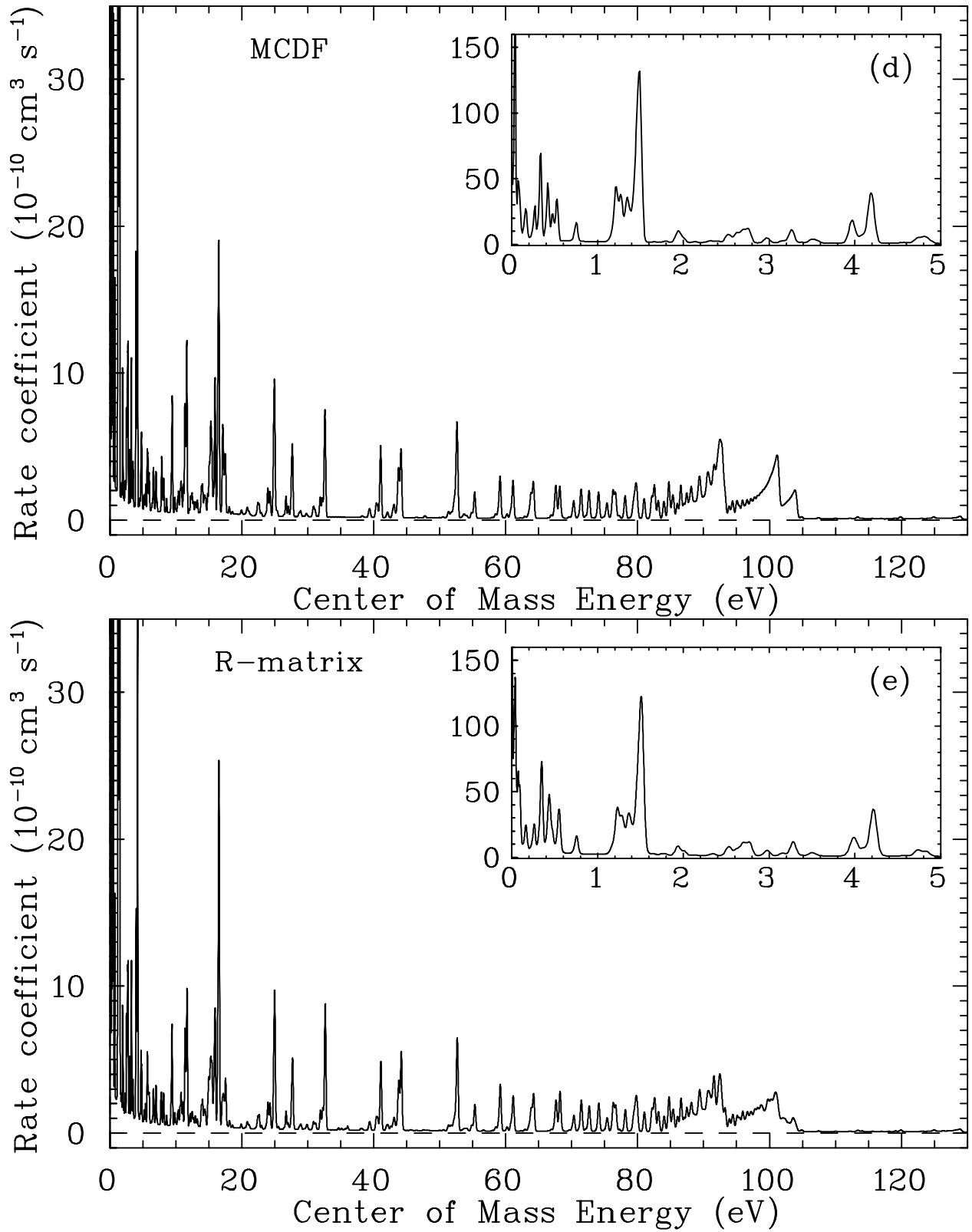


Fig. 1.— *Continued*

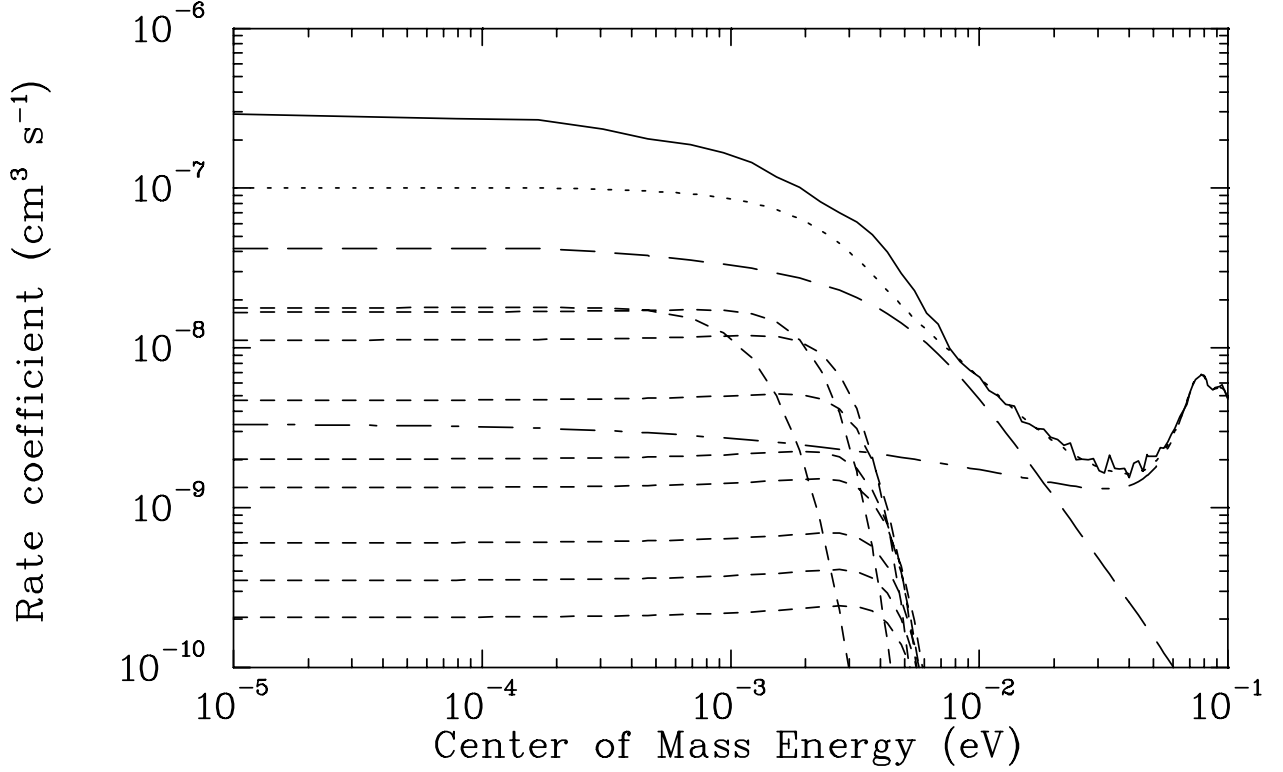


Fig. 2.— Measured and fitted Fe XX to Fe XIX $\Delta N = 0$ DR resonance structure below 0.1 eV. The experimental results are shown by the *solid curve*. The *dotted-long-dashed curve* is the fit to the data using our calculated RR rate coefficient and taking into account all resolved resonances. The *dotted curve* is the fit including the estimated contributions from the unresolved $2s^2 2p^3 ({}^2D_{5/2}^o) 15l$ (*short-dashed curves*) and $2s 2p^4 ({}^4P_{3/2}) 7d$ (*long dashed curve*) resonances (see § 3).

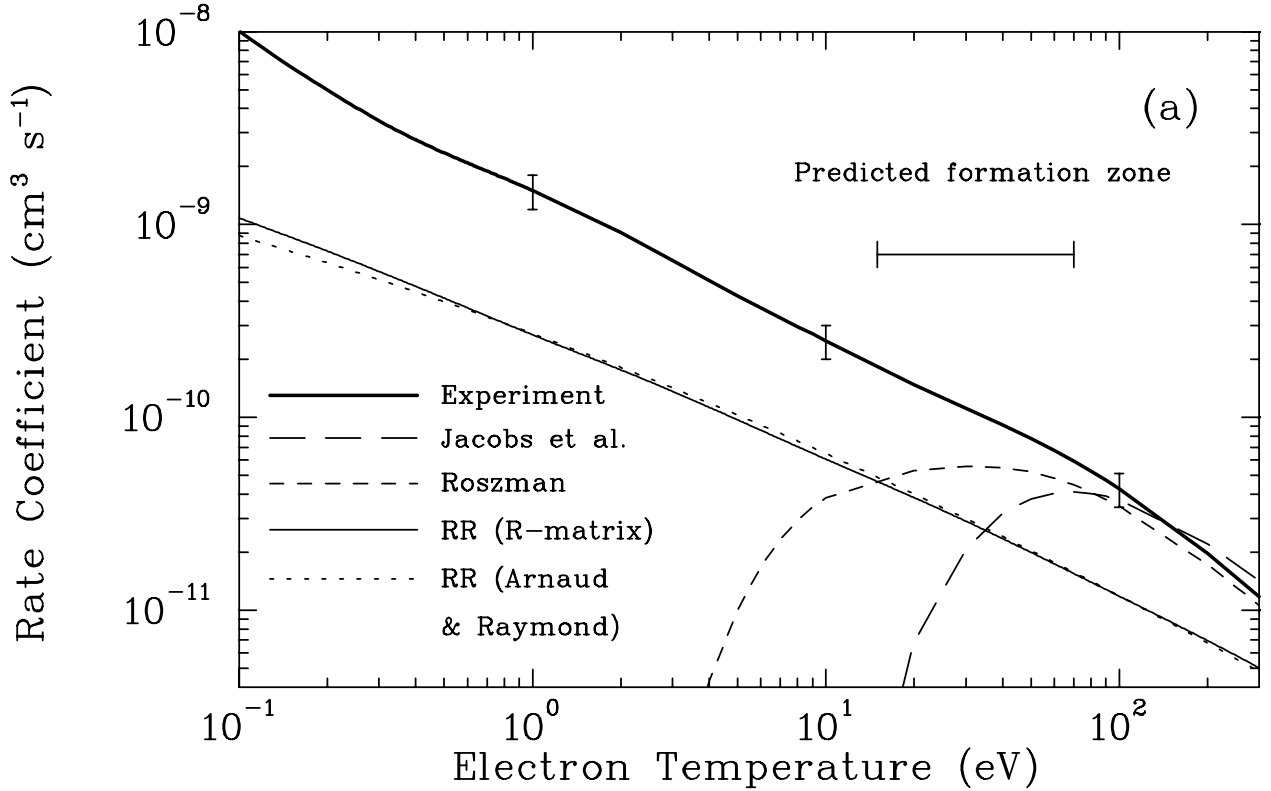


Fig. 3.— Fe XX to Fe XIX Maxwellian-averaged rate coefficient for $\Delta N = 0$ DR from $k_B T_e = 0.1$ to 300 eV. (a) The *thick solid curve* represents our experimentally-derived rate coefficient using the results shown in Figure 1(a) and listed in Table 2. The error bars represent the estimated maximum experimental uncertainty of 20% for $k_B T_e \geq 10$ eV. The *long-dashed curve* shows the *LS*-coupling calculations of Jacobs et al. (1977) as fitted by Shull & van Steenberg (1982). The *short-dashed curve* shows the unpublished *LS*-coupling calculations of Roszman as given by Arnaud & Raymond (1992). The *thin solid curve* is our R-matrix RR rate coefficient ($n_{max} = \infty$) which has been topped up using AUTOSTRUCTURE. Also shown is the recommended RR rate coefficient of Arnaud & Raymond (1992; *dotted curve*).

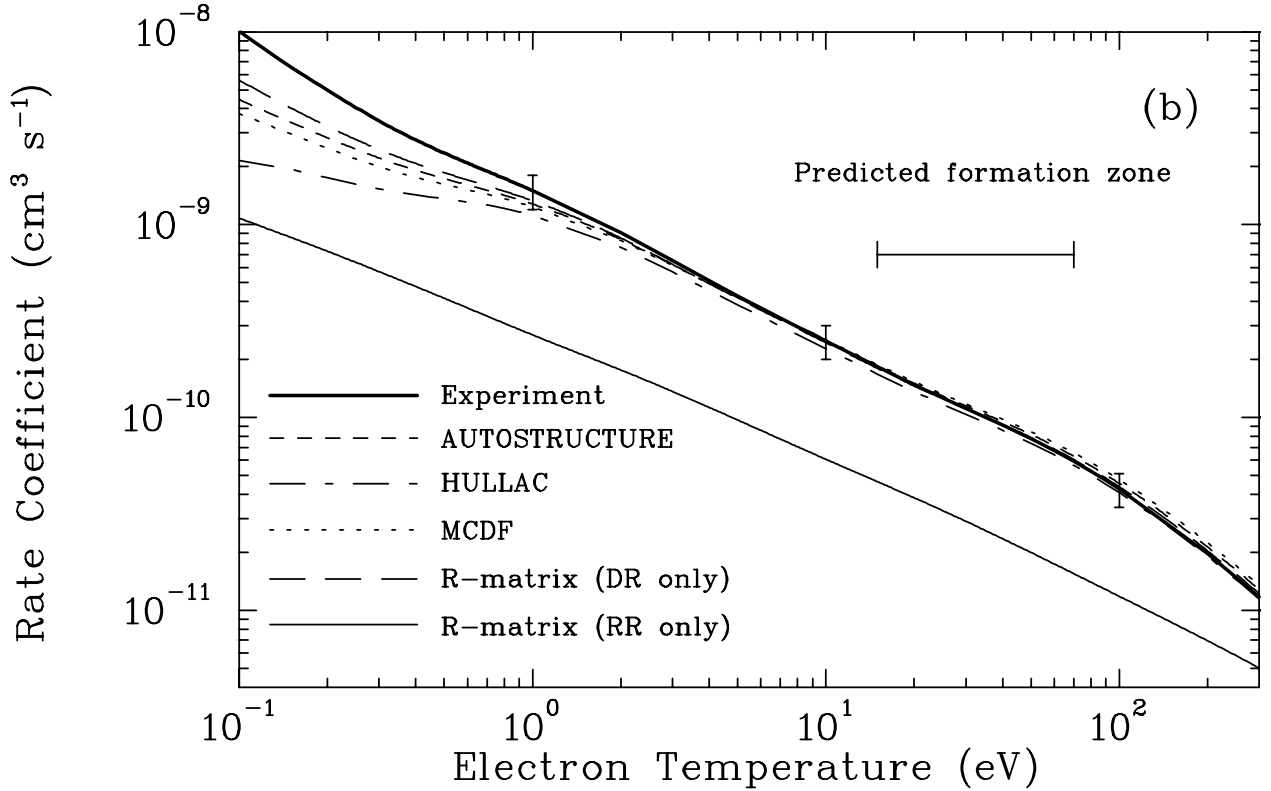


Fig. 3.— *Continued.* (b) In addition to our experimentally-derived DR rate coefficient (*thick solid curve*) and our topped up R-matrix RR rate coefficient (*thin solid curve*), both from (a), we also show our AUTOSTRUCTURE (*short-dashed curve*), HULLAC (*dotted-long-dashed curve*), MCDF (*dotted curve*), and R-matrix results (minus the R-matrix RR contribution, *long dashed curve*). All DR rate coefficients in (b) are for an $n_{max} = 120$. The formation zone for Fe XX for an optically thin, low-density photoionized plasma of cosmic abundances as predicted by XSTAR (Kallman & Bautista 2001) is shown by the horizontal solid line in both (a) and (b).

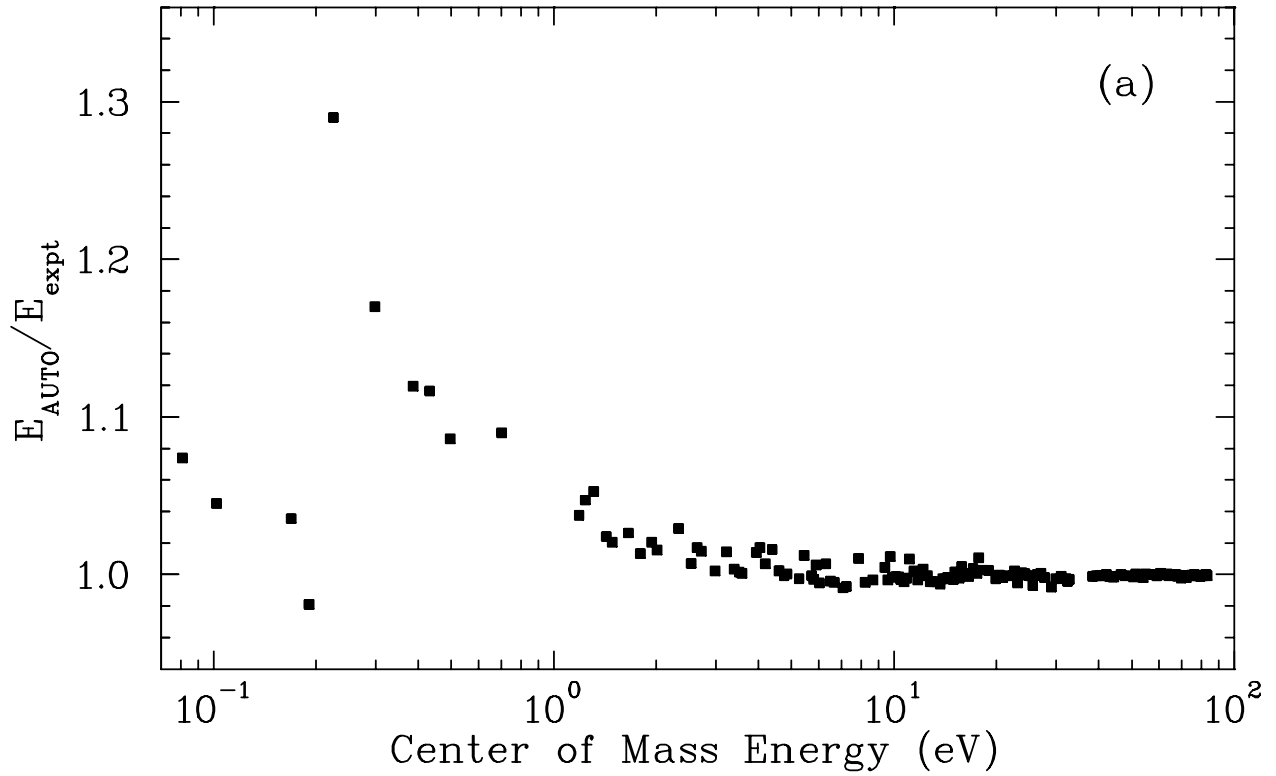


Fig. 4.— The ratio of the (a) AUTOSTRUCTURE, (b) HULLAC, and (c) MCDF resonance energies relative to the measured resonance energies as a function of center-of-mass collision energy from 0.07 to 100 eV.

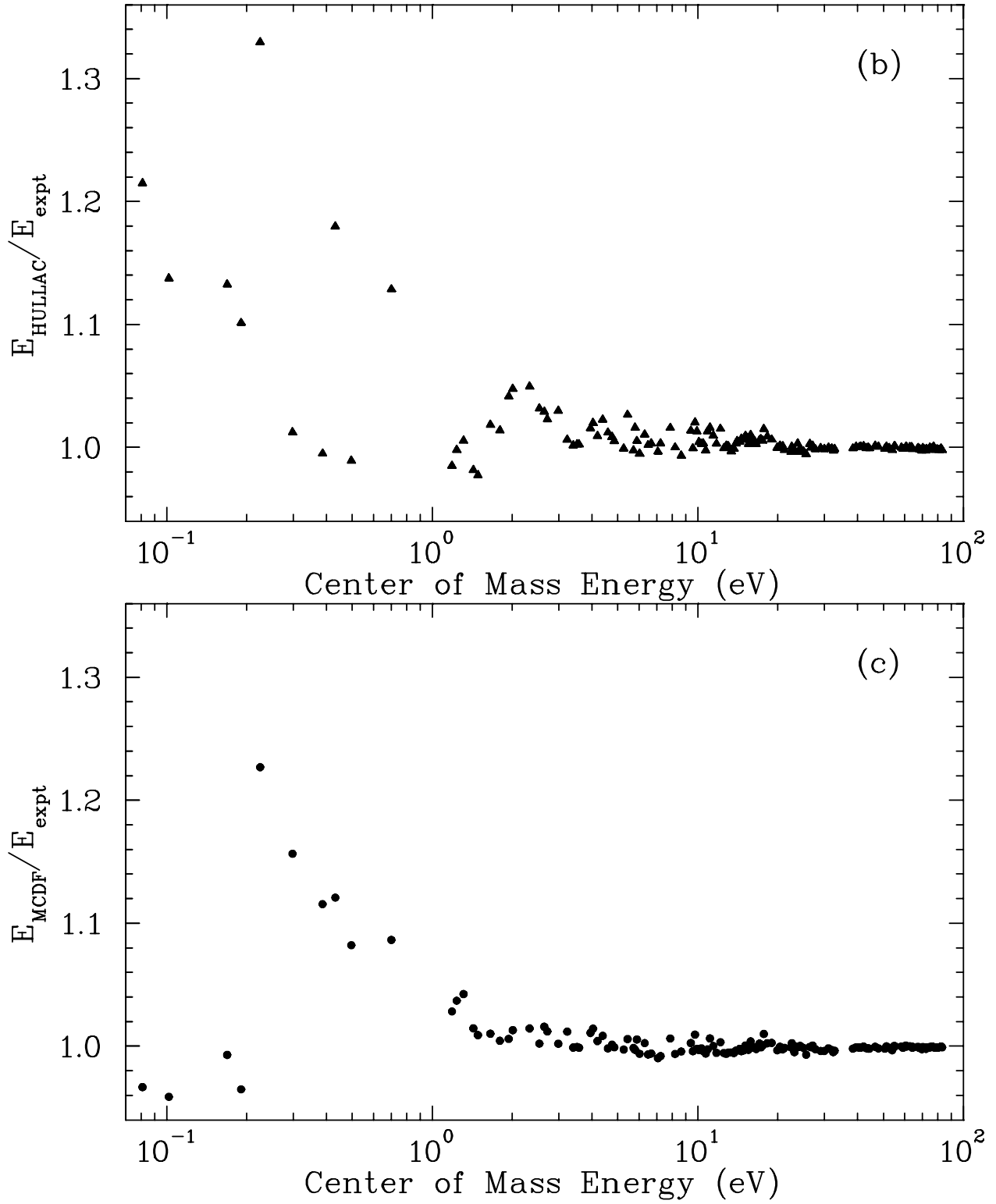


Fig. 4.— *Continued*

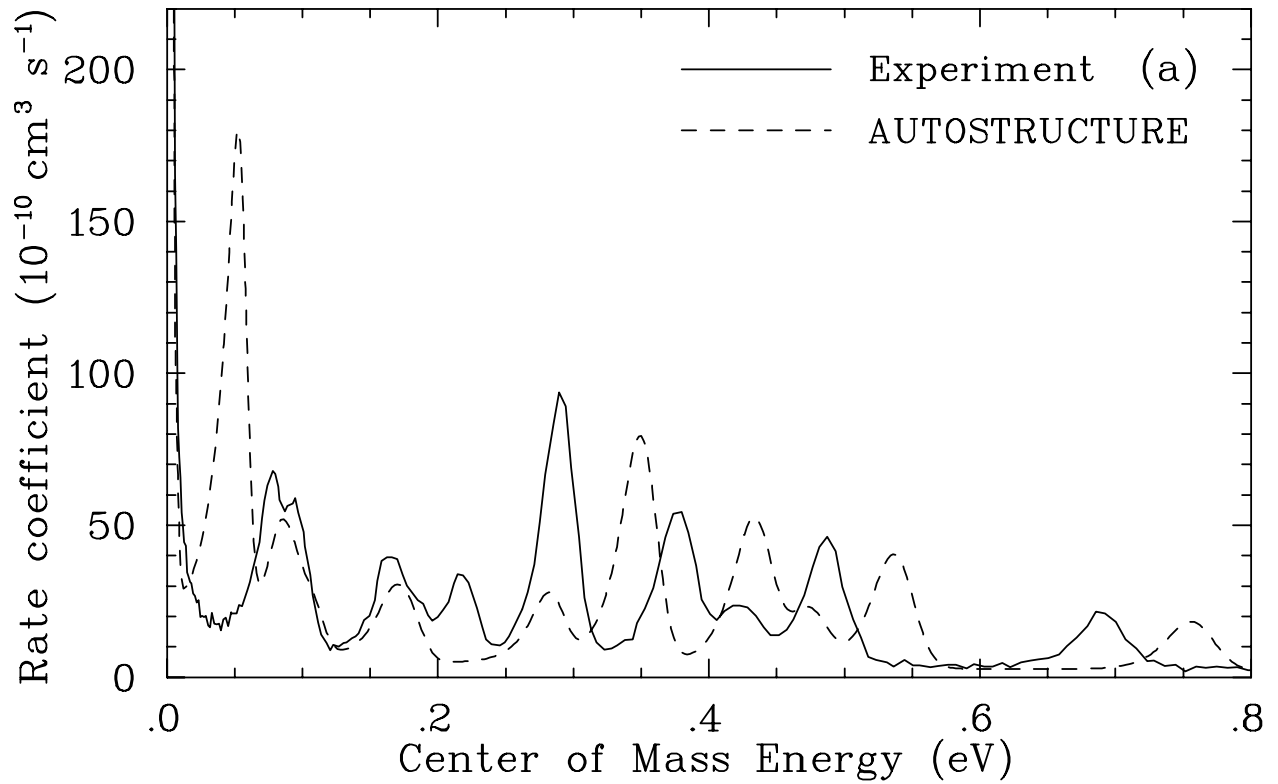


Fig. 5.— Theoretical Fe XX to Fe XIX $\Delta N = 0$ DR resonance structure between 0.015 and 0.8 eV compared to our experimental results: (a) AUTOSTRUCTURE, (b) HULLAC, (c) MCDF, and (d) R-matrix results. See Figure 1 for details.

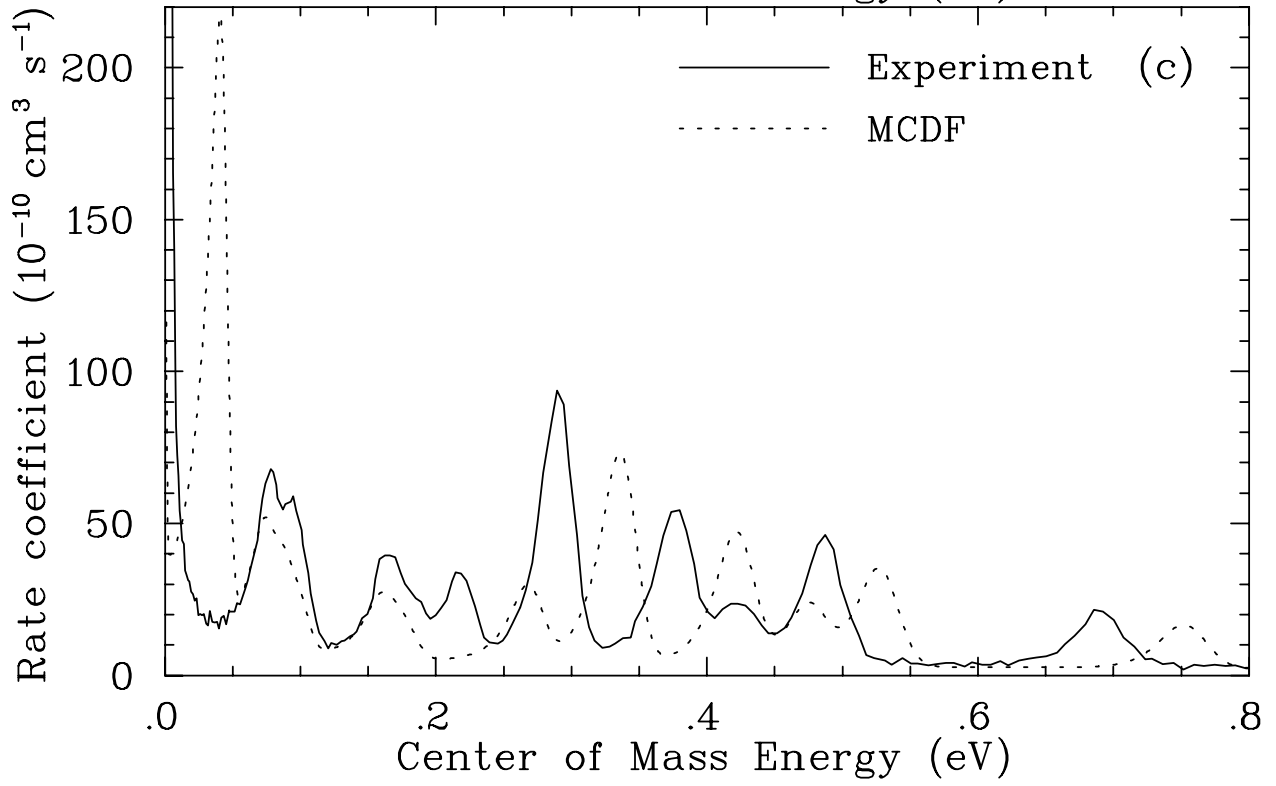
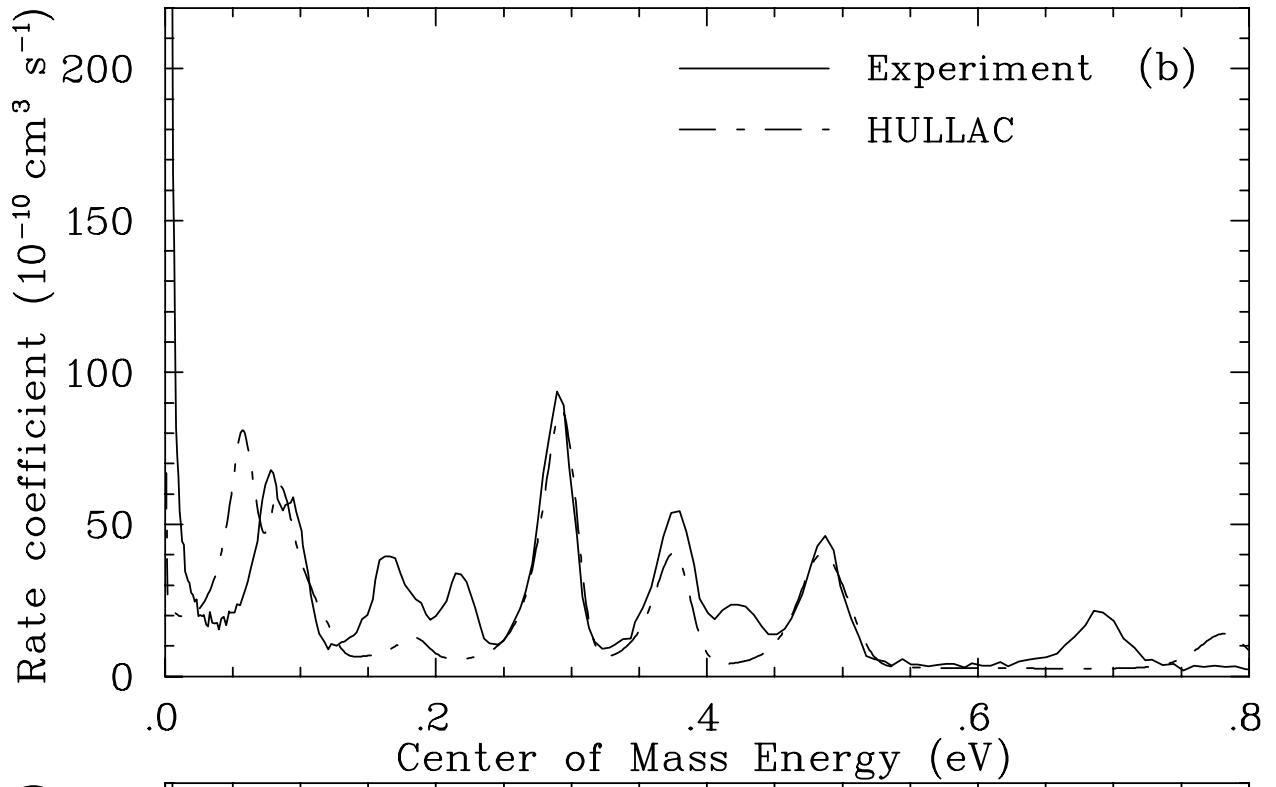


Fig. 5.— *Continued*

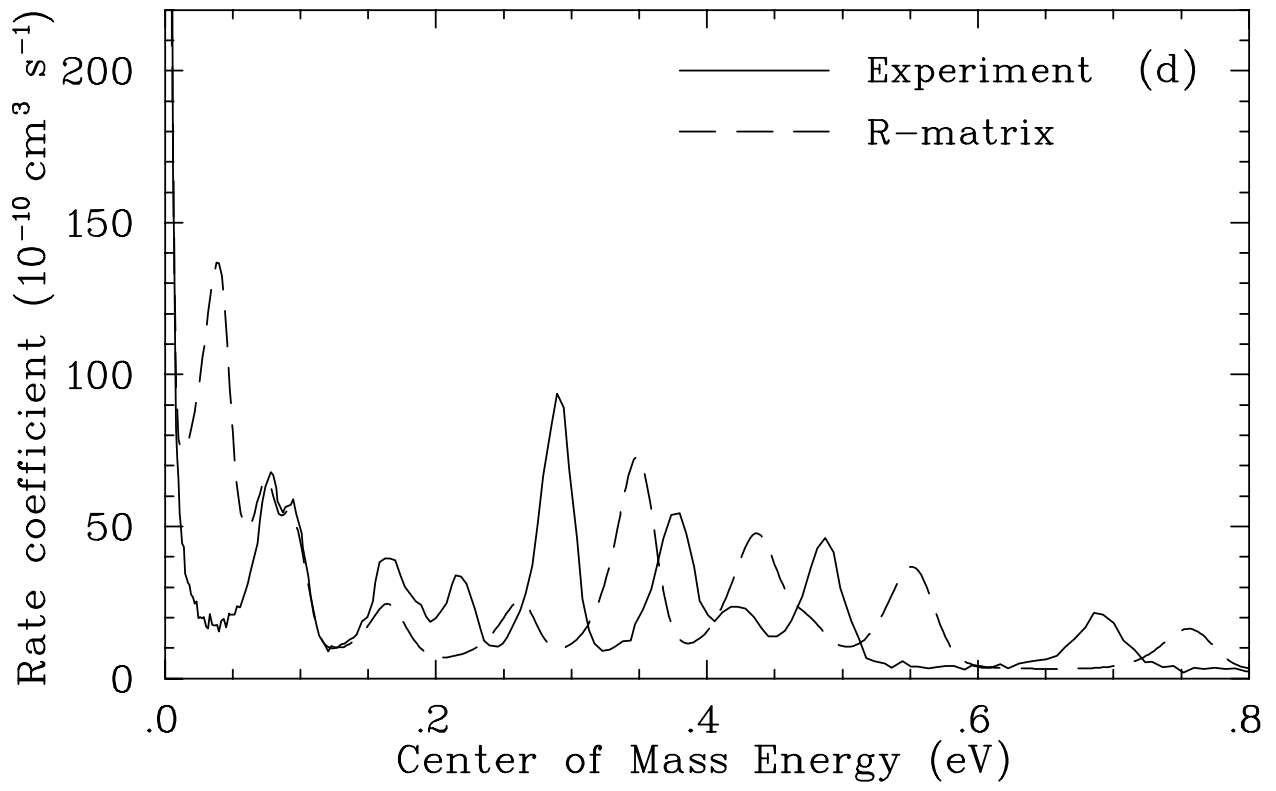


Fig. 5.— *Continued*

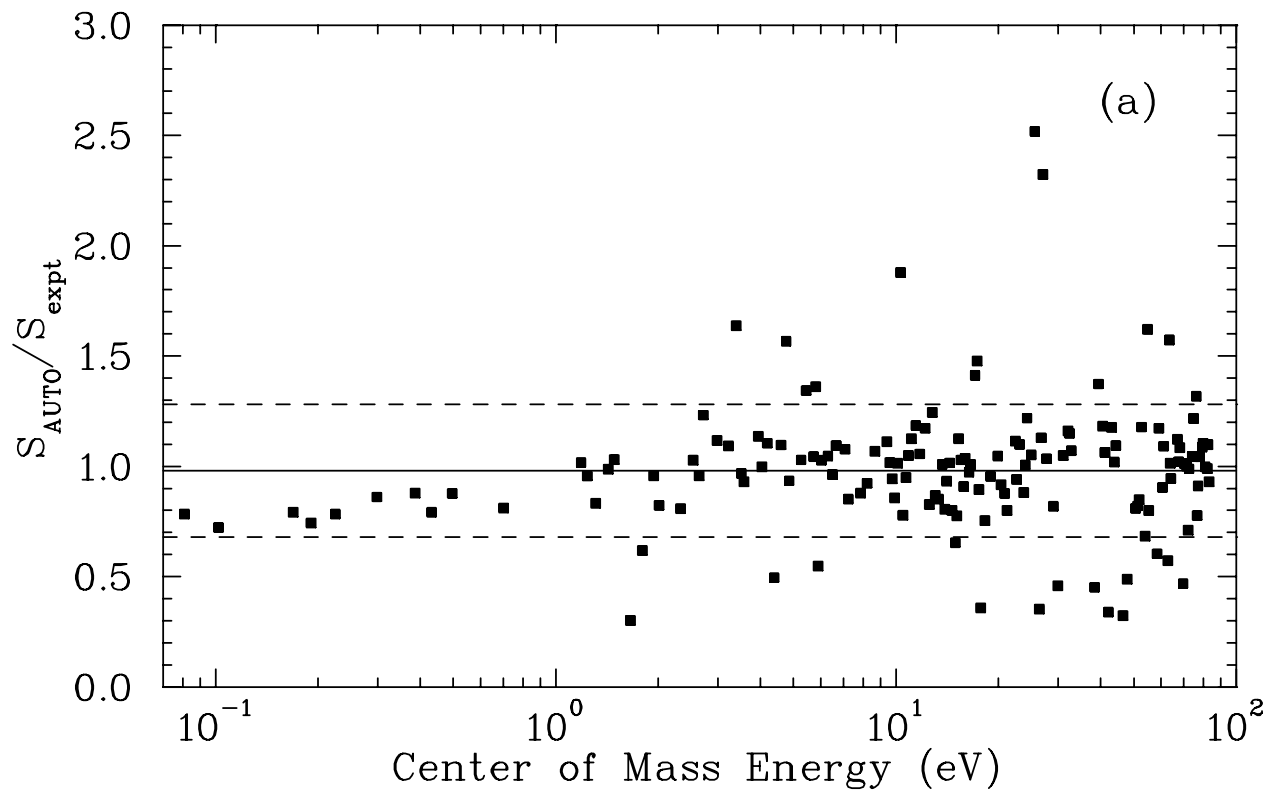


Fig. 6.— The ratio of the resonance strengths given in Table 2 for our (a) AUTOSTRUCTURE/experiment, (b) HULLAC/experiment, and (c) MCDF/experiment, results. Resonance strength ratios are shown as a function of center-of-mass collision energy from 0.07 to 100 eV. The solid lines show the average value for the various ratios. The dashed lines show the 1σ standard deviation from these average values.

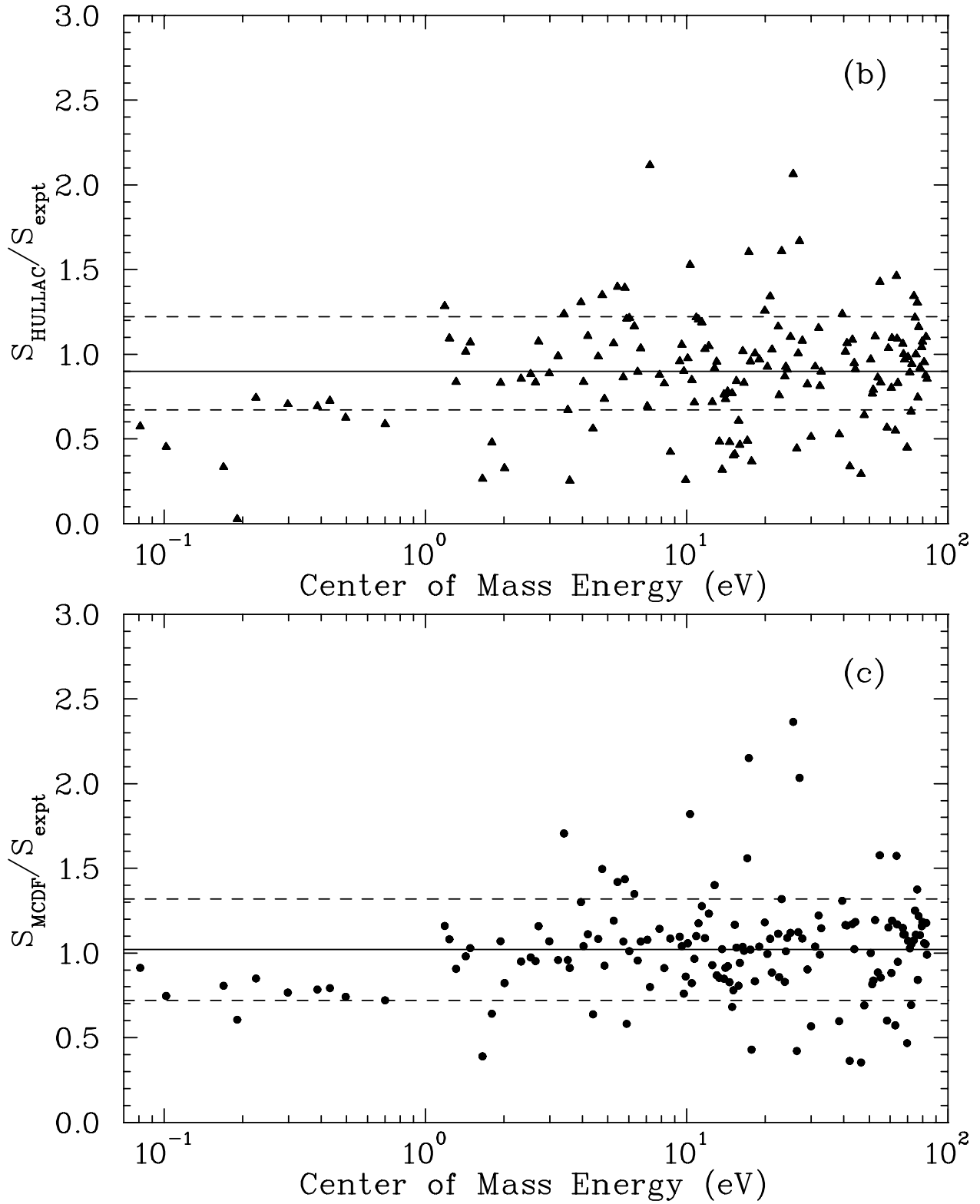


Fig. 6.— *Continued*

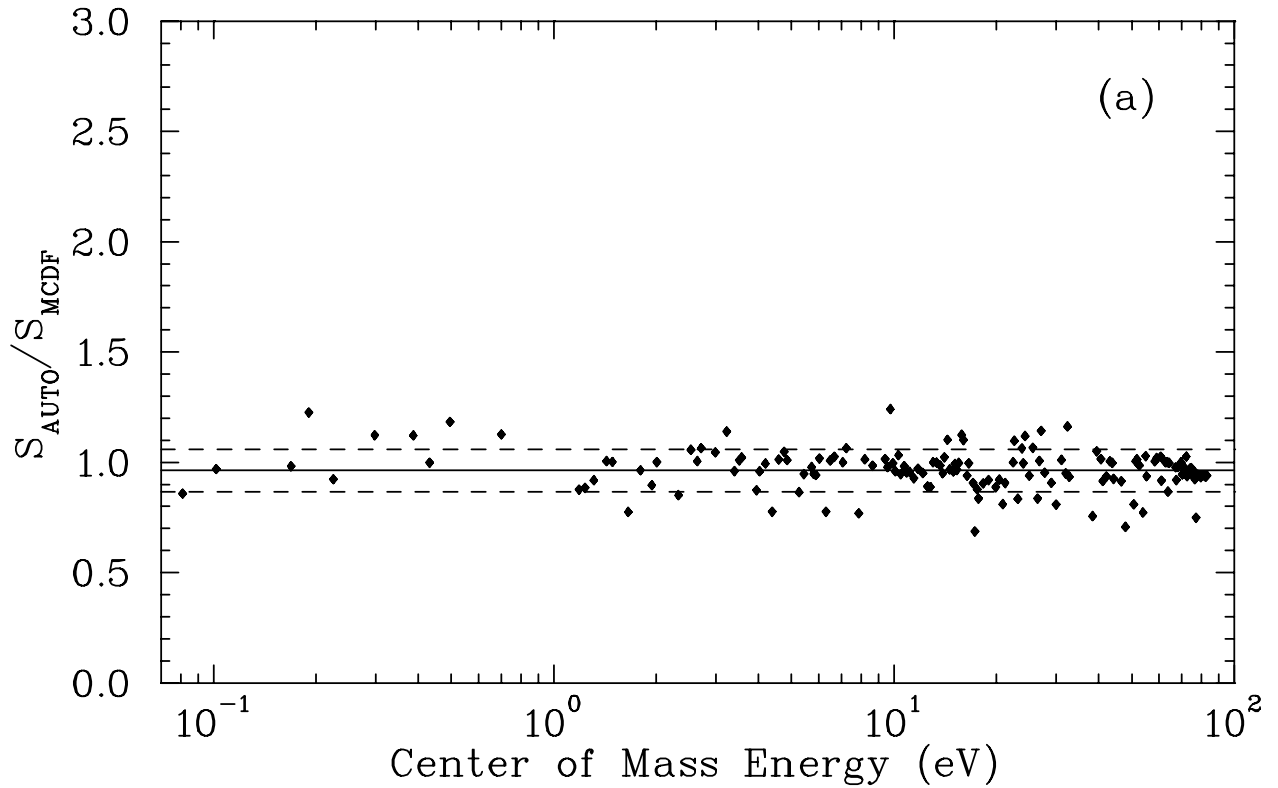


Fig. 7.— The ratio of the resonance strengths given in Table 2 for our (a) AUTOSTRUCTURE/MCDF, (b) HULLAC/MCDF, and (c) HULLAC/AUTOSTRUCTURE results. Resonance strength ratios are shown as a function of center-of-mass collision energy from 0.07 to 100 eV. The solid lines show the average value for the various ratios. The dashed lines show the 1σ standard deviation from these average values.

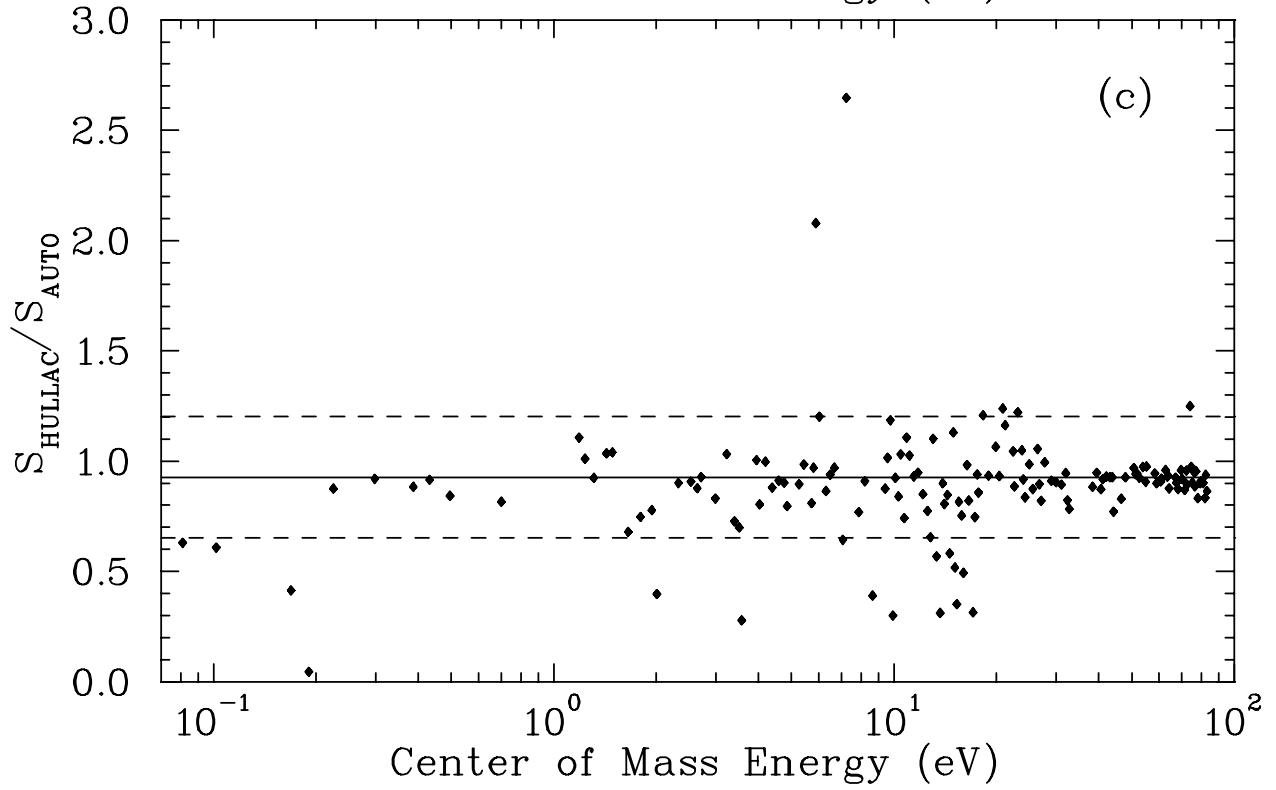
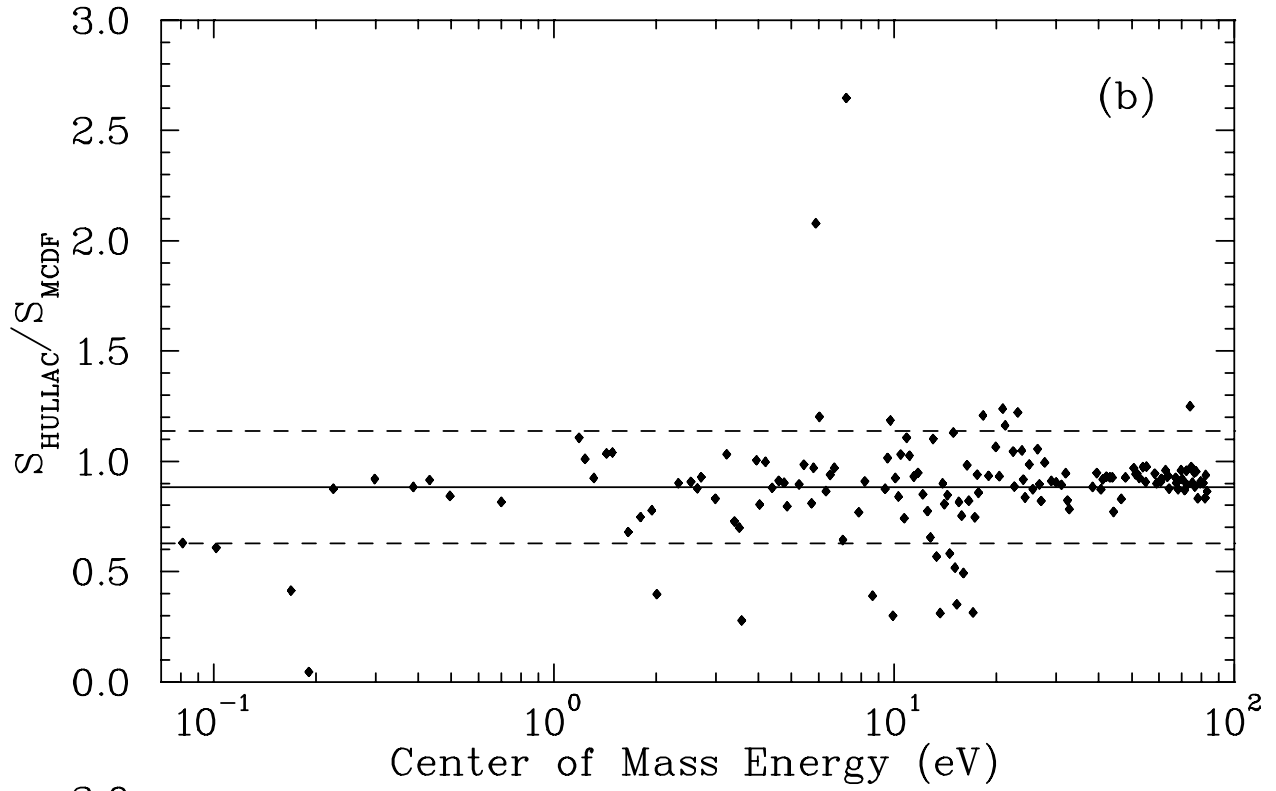


Fig. 7.— *Continued*